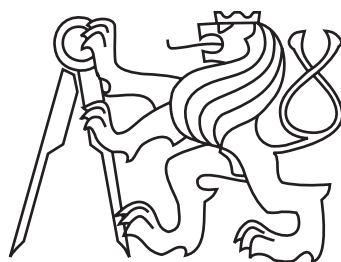# Czech Technical University in Prague
Faculty of Electrical Engineering

Doctoral Thesis

July 2017   Mushfiqul Alam

Czech Technical University in Prague
Faculty of Electrical Engineering
Department of Measurement

Adaptive Data Processing in Aircraft Control

Doctoral Thesis

Mushfiqul Alam

Prague, July 2017

Thesis Supervisor:
Associate Professor Jan Roháč, Ph.D.
Department of Measurement
Faculty of Electrical Engineering
Czech Technical University in Prague
Technicka 2
160 00 Prague 6
Czech Republic

Thesis Supervisor-Specialist:
Professor Sergej Čelikovsky, RNDr., CSc.
Department of Control Theory
Institute of Information Theory and Automation
Pod Vodarenskou vezi 4
182 08 Prague 8
Czech Republic

Abstract

This thesis focuses on the broad area of aircraft navigation solutions and control problems. For navigation solutions estimation of position, linear velocity and attitude (PVA) of a vehicle is of prime interest. In this work efforts are focused on developing a precise navigation solution for aircraft by looking for best estimator and improving the estimation performance while operating under challenging condition. In addition, the thesis addresses the design of aircraft flight controller to improve the performance of the aircraft. First part of the thesis explores the development of strapdown inertial navigation systems (INS) for aircraft using cost-effective micro-electro-mechanical-systems (MEMS) inertial sensors and aiding systems. The navigation solutions presented in the following are vehicle independent and can be used for ground, surface and air vehicles, or any moving body in general. However, for the experimental verifications small light weight aircraft is used. Small aircraft have fast dynamics and can be considered as worst-case scenarios. Within this part, firstly, a "easy to do" cost effective calibration method is introduced as a data pre-processing step for correcting sensor's deterministic errors such as, misalignment and scale factor. Secondly, an adaptive bandwidth filtering approach is proposed as a data pre-processing step for filtering the low frequency vibration effects from the inertial sensor's data. Finally, two data fusion techniques are discussed, exploiting the extended Kalman filter, to obtain the final navigation solution (PVA estimates). Mainly this part deals with principles of navigation, methods of system parameters estimation, calibration techniques, modeling, and data processing. Second part of the thesis investigates the application of nonlinear control techniques on fixed wing aircraft to improve the flight performance. A complete 3-DOF longitudinal flight controller for a fixed wing aircraft is discussed using nonlinear dynamic inversion technique, or in terms of control theory partial exact feedback linearization. Finally, an active gust load alleviation system is presented using a combined feedback/feedforward control technique for reducing the wing loading on an aircraft. All the navigation solution presented in this thesis are validated by extensive experimental data sets collected with real flight tests.

Keywords:

state estimation, aerial navigation, inertial measurement unit, data fusion, Kalman filter, flight control, dynamic inversion.

Abstrakt

Cílem dizertační práce je předložit řešení v oblastech leteckých navigačních a řídících systémů. V oblasti navigačních systémů se práce konkrétně věnuje vývoji a vytvoření způsobu odhadu pozice, linearizovaného vektoru rychlosti a orientace daného prostředku (letadla). V průběhu vývoje přesného navigačního systému byl hledán nejlepší možný estimátor a jeho výkonnost byla dále vylepšována pro činnost ve zhoršených podmínkách. Dále se práce zabývá návrhem řídících algoritmů vylepšujících letové vlastnosti letadla. První část se věnuje vývoji a dokumentaci inerciálního navigačního systému (INS) pevně spojeného s letadlem, tzv. strapdown, s využitím nízkonákladového vibračního senzoru typu MEMS a doplňujících navigačních systémů. Výsledné řešení je nezávislé na typu platformy (vozidla) a může být použito pro libovolný pohyblivý prostředek, létající nebo pozemní. Verifikace a testování systému proběhly na malém sportovním letadle, prostředku, který vykazuje velmi rychlé dynamické chování a tudíž může být považován za extrémní – nejhorší – testovací scénář. Jako první je popsána jednoduchá a snadno implementovatelná kalibrační metoda pro korekci určovacích chyb senzoru INS jako nesesouhlasení os (nesouosost – misalignment) a převodní konstanty (scale factor). V této části práce je též představen nově vyvinutý algoritmus pro předzpracování dat, založený na kmitočtovém filtru s adaptivní šířkou propustného pásma. Tento filtr slouží k odstranění vlivu mechanických vibrací na signály výstupu INS. Na konci první části dizertační práce jsou diskutovány dvě metody pro fúzi dat využívající rozšířeného Kalmanova filtru (Extended Kalman Filter - EKF) jakožto prostředku k získání výsledného odhadu navigačního řešení (vlastní pozice, rychlosti a orientace). Tato část se převážně věnuje metodám odhadu systémových veličin, technikám kalibrace, modelování a zpracování dat. Ve druhé části dizertace jsou prezentovány výsledky výzkumu a aplikace nelineárního řídícího algoritmu, určeného pro letoun s pevnými nosnými plochami. Cílem bylo pomocí řízení vylepšit letové charakteristiky letounu. Je zde diskutován kompletní řídící systém se třemi stupni volnosti využívající nelineární techniky – nonlinear dynamic inversion technique. Využíváno je zde linearizace prostřednictvím zpětné vazby, tzv. partial exact feedback linearization. Výsledkem je algoritmus aktivního systému pro tlumení podélných kmitů, který snižuje zatížení konstrukce křídla způsobené poryvy větru. Všechna navigační řešení a algoritmy předložené v této disertační práci byly podrobeny testování a verifikaci prostřednictvím rozsáhlého souboru reálných letových dat nahraného během letových zkoušek.

Klíčová slova:

stavová estimace, letecká navigace, inerciální měřící jednotka, datová fúze, Kalmanův filtr, řízení letu, dynamická inverze.

Acknowledgements

I would like to express my gratitude to my supervisors Jan Rohac and Sergej Celikovsky for providing necessary resources, excellent guidance, support and numerous dedicated hours of discussions, that inspired me in many ways during the last four years. I thank them for creating the perfect condition for research and introducing me to interesting research problems and questions. I would also like to extend my thanks to Martin Hromcik for the special cooperation. I humbly acknowledge the incredible support provided by the head of the Department Prof. Jan Holub.

I extend my thanks to the external colleagues for cooperation, Jakob Hansen, Torleiv Bryne, Kristoffer Gryte, Prof. Thor Fossen and Tor Johanssen.

A huge thanks goes to the staff of the Department of Measurement for ensuring a pleasant and flexible environment for my research, and to my colleagues from the Laboratory of Aircraft Instrumentation Systems for creating the enjoyable research atmosphere and unforgettable friendships. I am grateful to my colleagues Martin Sipos, Jakub Simanek, Petr Novakcek, Jan Popelka and all other research staff at the department for their invaluable cooperation, insights and help in carrying out hundreds of experiments and sharing the valuable datasets.

Doctoral research is not easy without the incredible administrative support. I would like to extend my gratitude to all the administrative staffs of the department, especially, Ms. Kocova, Sankotova and Ms. Kroutilikova from the Dean's office, for helping me doing all the related paper works through out my research.

I sincerely appreciate my friends for their continuous support during the times I almost felt like giving up. Few names I must mention are Matej, Dimitar, Claudia, Alex, Richard, Zackova, Oliver, Norbert, Jayanta, Gabbi, Sameen, Uddam, Shahir, Raitul, Nauman, Shabab and Anuj.

I am deeply grateful to my family for their encouragement, inspiration and mental support especially Api (sister), Mamas (uncles), Khalamonis (aunties) and nanu (grandmom). Last but not least, I am much obliged to everyone who endured me throughout this venture of my doctoral research.

To,
Ammu (my mother)
Momarrema Alam
&
Abbu (my father)
Mostafizul Alam

Contents

List of Figures

Abbreviations

2D / 3D	Two / Three Dimensions
ACC	Accelerometer
AFCS	Aircraft Flight Control System
AHRS	Attitude and Heading Reference System
ARS	Angular Rate Sensor or gyro
CF	Complementary Filter
CG	Centre of Gravity
DOF	Degree of Freedom
FIR	Finite Impulse Response
GLAS	Gust Load Alleviation System
GNSS	Global Navigation Satellite System
GPS	Global Positioning System
IMU	Inertial Measurement Unit
INS	Inertial Navigation System
KF / EKF / UKF	Kalman Filter / Extended / Unscented
LP	Low Pass
MEMS	Micro-Electro-Mechanical-Systems
NDI	Nonlinear Dynamic Inversion
PVA	Position, Velocity and attitude

Chapter 1

Introduction

1.1 Motivation

Good navigation performance of an aircraft is dependant on the availability of accurate navigation data and good control law design. For navigation, the most fundamental essential parameters include the estimation of position, velocity and attitude (PVA). MEMS (Micro-Electro-Mechanical System) based inertial navigation system (INS) consisting of tri-axial accelerometer (ACC) and tri-axial angular rate sensor (ARS) aided with GNSS receiver is most commonly used for a cost-effective strapdown navigation solution. The accuracy of the navigation solution is directly related to the choice of sensors. Therefore, it is important to have reliable and appropriate sensors depending on the application. First section of the thesis deals with the improvement of overall accuracy on navigation data estimation using cost-effective MEMS based INS. It includes topics concerning the evaluation of sensor's deterministic and stochastic parameters. The deterministic errors are evaluated by a "easy to do" calibration technique and sensor's stochastic parameters are evaluated by using sensor's data pre-processing, data validation techniques, data fusion methods applied to navigation equations.

Accelerometer can also be used to detect vibration effects on aircraft. Vibration effects on the wing in an aircraft can be assessed by measuring the vertical acceleration at a number of locations on the aircraft using ACCs [2]. The acceleration of the wing tip relative to the CG of the aircraft gives the measure of wing vibrations experienced by the aircraft. This information later can be used to design an active feedback controller to alleviate the vibration effects on the aircraft.

Recent development of the light weight aircraft has led to flexible aircraft with pronounced aeroelastic effects. Flexible aircraft develops large values of elastic displacement and acceleration in addition to those components of displacement and acceleration which arise from the rigid

body motion of the aircraft. The problem can occur because the control system sensors are of sufficient bandwidth to sense the structural displacements/vibrations/oscillations as well as the rigid-body motion of the aircraft. Therefore, for detecting the wing vibration, a filtering technique with adaptive bandwidth which can be applied on accelerometers is desirable for improving the control performance. The second part of the thesis aims a providing a detailed analysis on the design and development of aircraft flight controller for 3-DOF longitudinal flight controller and active vibration alleviation system.

The navigation solutions presented in this thesis are independent of any vehicles and can be used for ground, surface and air vehicles, or any moving body in general. However, for the experimental verifications small aircraft is used as they have fast dynamics and can be considered as worst-case scenarios. Verification of the flight control laws are carried out via simulation on high-fidelity dynamical model using MATLAB/Simulink.

1.2   Scope, Objective and Contributions

The thesis covers selected topics within the field of navigation systems for aircraft and flight control. The main objective of the research was to investigate and develop advanced algorithms and methodologies in order to enable increased usage of cost effective inertial sensing technology providing as accurate navigation data as possible. One of the other objective of the research was to design automatic control laws for fixed wing aircraft for navigation and load alleviation purposes.

1.2.1   Main Contributions

The main contributions from this doctoral thesis are summarized as:

- This thesis describes the two main areas of navigation, namely data pre-processing and state estimation and secondly, flight control for aircraft, and proposes the motivation behind our efforts at merging them to obtain good performance.

- Extends the recent years of development in calibration method for MEMS based IMU [46] by developing an "easy to do" cost efficient calibration technique for cost-effective IMU [4].

- The accuracy of final attitude and heading reference system (AHRS) is often compromised when the IMU operates under harsh environment. While operating under harsh environment the IMU data are significantly affected by low frequency vibration reducing the final estimation accuracy. A novel concept of using adaptive bandwidth filtering is proposed as a pre-processing of IMU data before the final attitude estimation. This approach preserves the dynamic information of the vehicle and increases the final estimation accuracy [3].

- A novel estimation algorithm is developed for a cost-effective navigation solution using commercial grade inertial sensors. Two different architectures of EKFs are proposed and performance are studied in details for robustness analysis with respect to GNSS outage [45].

- Longitudinal flight controller for a fixed-wing aircraft using non-linear dynamic inversion technique or, in terms of control theory, partial exact feedback linearisation is developed. A combination of three different flight controllers provide complete 3-DOF longitudinal flight control [1].

- A robust feedforward/feedback gust load alleviation system (GLAS) was developed to alleviate the gust loading on aircraft. The combined feedforward/feedback GLAS significantly reduces the wing root root moments for shorter as well as for longer gusts giving potential structural benefits and weight savings [4].

- A detailed comparative analysis is presented in the improvement of the final navigation solution using the adaptive variable bandwidth as a data pre-processing step.

1.2.2 List of Author's Publication

The results presented in this thesis are based on the following impacted journal articles and peer reviewed conference papers:

1.2.2.1 Journal Publications Directly Presented in the Thesis

1. Rohac, J., Hansen, J., **Alam, M.**, Sipos, M., Johansen, T., Fossen, T. "Validation of Nonlinear Integrated Navigation Solutions." *Annual Reviews in Control*, 43(1), 91–106, 2017.

2. **Alam, M.**, Celikovsky, S. "On Internal Stability of the Nonlinear Dynamic Inversion (NDI): Application to Flight Control." *IET Control Theory & Applications*, 11(12), 1849–1861, 2017.

3. **Alam, M.**, Rohac, J. "Adaptive Data Filtering of Inertial Sensors with Variable Bandwidth." *Sensors-An Open Access Journal*, 15(2): 3282-3298, 2015.

4. **Alam, M.**, Hromcik, M., Hanis, T. "Active Gust Load Alleviation System for Flexible Aircraft: Mixed Feedforward/Feedback Approach." *Journal of Aerospace Science and Technology*, 42(1): 122-133, 2015.

1.2.2.2 Conference Publications

1. **Alam, M.**, Moreno, G., Sipos, M., Rohac, J. "INS/GNSS Localization Using 15 State Extended Kalman Filter." *International Conference in Aerospace for Young Scientists*, Beijing, China, 2016.

2. **Alam, M.**, Sipos, M., Rohac, J., Simanek, J. "Calibration of a Multi-Sensor Inertial Measurement Unit with Modified Sensor Frame." *International Conference on Industrial Technology*, Seville, Spain, 2015.

3. **Alam, M.** "Combined Feedforward/feedback Gust Load Alleviation Control for Highly Flexible Aircraft." *PEGASUS-AIAA Student Conference*, Prague, Czech Republic, 2014.

1.2.2.3 Publications Not Presented in the Thesis

1. **Alam, M.**, Celikovsky, S., Walker, D. "Robust Hover Mode Control of a Tiltrotor Using Nonlinear Control Technique." *AIAA Guidance, Navigation, and Control Conference*, California, USA, 2016.

2. **Alam, M.**, Narenathreyas, K."Oblique Wing: Future Generation Transonic Aircraft." *International Journal of Mechanical, Aerospace, Industrial, Mechatronics and Manufacturing Engineering*, 8(5): 888–891, 2014.

1.3 Structure of the Thesis

This doctoral thesis is written in the format of *thesis by publication* approved by the Dean of Faculty of Electrical Engineering and by the *Directive for dissertation theses defense, Article 1.*

The thesis presents publications relevant to the topic of the thesis as individual chapters. The main contributions in this thesis are divided into Chapter 3 – 8. Chapter 3 – 7 presents 5 publications with unified formatting. Each chapter begins with a short summary section, where the main topic, conclusions, and contribution of the research work is explained.

The thesis is organized as follows: Chapter 2 presents the current state-of-the-art in both state estimation for aircraft navigation and application of control theory on aircraft. Chapter 3 – 7 introduces author's 5 major publications related to the topic of this doctoral thesis. Chapter 8 is an extension of Chapter 4 and Chapter 5 which provides further examination on the results of the adaptive data processing on navigation data estimation. The doctoral thesis is summarized and concluded in Chapter 9, which also discusses the suggestions for future work.

Chapter 2

State of the Art

This chapter aims at providing details on the state of the art regarding the topics related to this thesis. The thesis aimed to provide state estimation system for navigation purposes capable of working in challenging environment in order to have good control performance for aircraft. Therefore the first part of this chapter reviews the current state-of-the-art in state estimation applied especially for aerial navigation. The second part of this chapter reviews the current state-of-the-art related to the active control of aircraft for navigation and load alleviation purposes.

2.1 Navigation Data Estimation using Inertial Sensors

2.1.1 Inertial navigation systems - Sensor Technology

Navigation systems providing the tracking of an object's position, velocity and attitude (PVA) plays a keys role in wide range of applications, such as aeronautics, robotics and automotive industry. Inertial sensors measure angular rates and specific forces, using angular rate sensors (ARS) and accelerometers (ACC), respectively. 3-axis ACCs and 3-axis ARSs forms the core of the inertial measurement unit (IMU). Typically PVA are obtained via dead reckoning. One form of dead reckoning technique is using the initial position, velocity and attitude related to a coordinate frame of interest and consecutive update calculation based on the ACC and ARS measurements. Appropriate class of inertial sensors are essential to be chosen based on the economical aspect and the required navigation precision. The choice of the required precision is directly dependant on the application. Fig 2.1 and Fig 2.2 shows the required precision depending on the application for ARSs and ACCs.
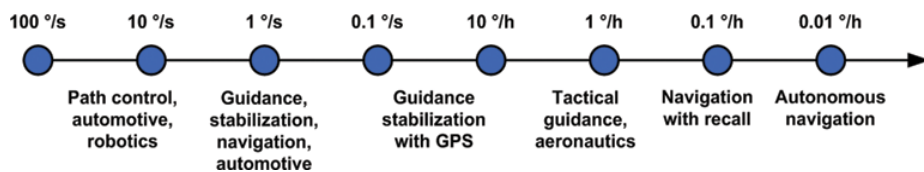
Figure 2.1: Bias instability of gyroscopes related to specific applications [23].
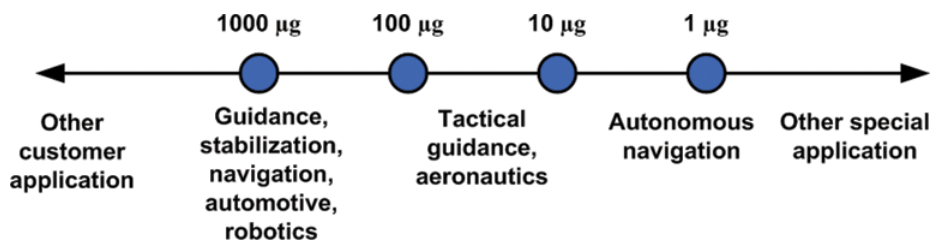
Figure 2.2: Bias instability of accelerometers related to specific applications [23].

From Fig 2.1 and Fig 2.2, it can be seen that ARS with precision better than $1°/h$ and ACC not less than $10\mu g$ are required for the usage in aircraft navigation. The higher precision, the more expensive the device is. Inertial sensors such as fiber optic gyroscopes (FOGs), ring laser gyroscopes (RLGs), servo ACCs can be used for high precision application however they are expensive. In comparison, micro-electro-mechanical-systems (MEMS) sensors are compact, lightweight and cost effective, thus offering an inexpensive solution for navigation purposes. Nevertheless, at the same time, MEMS-based inertial sensors suffer from bias instability, insufficient sensitivity, noise, etc., which presents significant challenges in data processing that have to be dealt within the navigation processes. The dynamic bias is the in-run variation of the bias also known as bias instability. In addition to sensor bias there are other sensor errors such as scale factor and scale factor nonlinearity. ARS also have g-sensitivity induced errors. These sensors may also be misaligned internally in the triad. Since the PVA estimation from inertial sensors primarily relies on the integration, these inaccuracies cause unbounded error growth, which needs to be corrected by data obtained from so-called aiding systems, e.g., magnetometers, GNSS, electrolytic tilt sensors, pressure based altimeter, etc.

2.1.2 Data Processing in Navigation System

Navigation systems are primarily supposed to provide PVA estimates. The navigation data are typically estimated by a chain of processes as schematically shown in Fig 2.3.

Signal/data preprocessing can differ according to vehicle dynamics and types of sensors utilized. The sensors might have analogue as well as digital outputs. In the case of analogue outputs, the preprocessing requires A/D conversion. The low pass (LP) filter is then used for both high-

Figure 2.3: Block scheme of processes required for position, velocity, and attitude estimation.
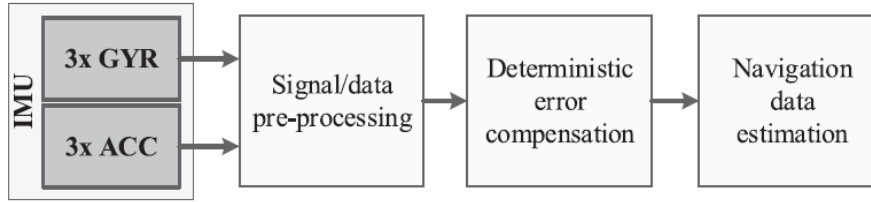
frequency components reduction and as an anti-aliasing filter. When the outputs are in digital form then a digital LP filter is utilized only. It is very important to choose the cut-off frequency correctly and additionally observe the group delay. Usually, the sensor's bandwidth is about 300 Hz up to 800 Hz depending on the sensor's type. If high rate navigation solution is required, which is generally intended for airborne applications, the frequency bandwidth can be reduced down to 50 or 40 Hz. In some applications it can go even lower down to 20 or 10 Hz, but it is not a common case. Deterministic error's compensation is a further key process minimizing effects of non-orthogonality of sensing axes, sensor scale factors, temperature dependencies as well as misalignment of sensor frame mounted into vehicle body frame. Most of these deterministic error corrections can be done during in-flight/motion calibration procedures; however, the most common way is to calibrate sensor errors separately.

2.1.3 Deterministic Error Compensation

In the field of navigation the estimation of inertial sensor's deterministic errors play a key role. Mainly multi-axial non-orthogonalities/misalignment and scale factor errors have to be identified and estimated within a calibration process. There are several approaches to calibrate the sensor for compensating deterministic errors, see for e.g. [10], [25], [53] and [52]. However, their applicability is strongly influenced by the time requirement and equipment required for the calibration process. These two factors mainly affects the price. Recently, a inexpensive calibration procedure for ACC using the knowledge of the gravity magnitude under static condition is presented in [46].

2.1.4 Estimation of Position, Velocity and Attitude

Inertial sensor's measurements suffer from errors such as bias and noise. Hence, if the estimation process is entirely based on dead reckoning through a kinematic model, the estimation process suffers from unbounded error growth. Therefore, some form of aiding systems are used for PVA estimation, most commonly position and velocity aiding using GNSS. The inaccuracies in the MEMS based inertial navigation system (INS) presents significant challenges in data processing

7

which is essential to deal within the data fusion process. There are various methods for INS aiding using GNSS based measurements by means of un-coupled [48], [49], loosely coupled [63], tightly coupled [31], and ultra-tightly coupled [5] integration schemes.

There are several approaches to data fusion for attitude estimation, such as temporally-interconnected observers (TIO) [6], complementary filters [29] or Kalman filters [13]. The most common sensor fusion algorithms of choice are variants of the nonlinear extension of the Kalman filter (KF), the extended Kalman filter (EKF), which has been covered in the literature for five decades, such as work presented in Ref [15], [35], [58], [13], [17] and [19] often uses an error-state implementation based on complementary filtering.

The work of Swirling in the field of least-squares estimation and signal processing could be traced back as one of the first efforts to use the computational advantages of applying recursion to least-squares problems [56]. Swirling first introduced the concept of "stagewise smoothing" through his publications in 1958 and 1959 [57]. Later on in 1960s Rudolf Kalman presented error propagation methods using a minimum variance estimation algorithm for linear systems, commonly known as Kalman Filter or linear quadratic estimation (LQE) [28]. Later on with the development of the digital systems, discrete method presented by Rudolf Kalman have received large attention and is now a fundamental term in various fields [22].

The Kalman filter (KF) introduced a recursive algorithm for state estimation of linear systems, which is optimal in the sense of minimum variance or least square error. The algorithm works in a two-step process, firstly prediction step and secondly, the measurement update. In the prediction step, the Kalman filter produces estimates of the current state variables via a kinematic model of the process, along with their uncertainties. In the measurement update step, the outcome of the next measurement (necessarily corrupted with some amount of error, including random noise) is observed, these estimates are updated using a weighted average, with more weight being given to estimates with higher certainty. The recursive nature of the algorithm makes is suitable to run in real-time using only the present input measurements and the previously calculated state and its uncertainty matrix; no additional past information is required. This makes the estimation process computationally efficient.

Kalman filter is a well-established state estimation approach [9]. Kalman filter assumes that the input to the time-varying state space model is normally-distributed defined by their mean and covariance. A important requirement is that the measurements have to be functions of the states, as the residual measurement (the difference between measured and estimated measurements) is used to update the states and keep them from diverging [22]. General assumtion about the process and measurement noise is to have Gaussian white noise. In cases where the noise of the system is not white, the KF can be augmented, by so called "shaping filters", with additional linear state equations to let the coloured noise be driven by Gaussian white noise [13]. The recursive estimation of the system's states using the Kalman filter also propagates a covariance matrix

which describes the uncertainties of the estimated state as well as the correlation between the other states [19].

The kinematic equations for navigation are naturally nonlinear due to the associated trigonometric transformations. Therefore, nonlinear estimation techniques are essential to use for accurate estimation ensuring stability of the modeled system. Originally the Kalman filter was designed for linear systems, however it can be applied to nonlinear systems without changing the operational principles. Nevertheless, the filter is no longer a optimal estimator due to the loss of guaranteed minimal variance. Nonlinear estimation problems are generally dealt by the Linearised KF (LKF), Extended KF (EKF) or sample-based methods such as unscented KF (UKF) [7], [20]. The UKF is an extension to nonlinear systems that does not involve an explicit Jacobian matrix, see [27]. The most widely used method is the EKF, which has been laregely applied in many applications where it achieved excellent performance [18]. The EKF uses nonlinear model in the time propagation for the state estimation. The EKF linearises the nonlinear model around an estimate of the current state using multivariate Taylor expansions before the time propagation of the covariance estimated and gain computation. This linearisation makes the EKF vulnerable to errors in the initial estimates compared to linear Kalman filter.

The KF and EKF are considered as the standard estimation theory and are therefore used as benchmark for comparison when developing new methods. The KF and its variants have been widely used in the navigation related literatures. Few examples can be mentioned are: An introduction to choice of states and sensor alignment consideration can be found in [55], while Ref [34] considers alternative attitude error representations. Extensive details on Kalman filtering can be found in Ref [13], [15], [18] and [19]. Ref [12] presents a method for evaluating the quality of linearisation for nonlinear systems and their usage in the Kalman filter. A study on coloured noise in contrast to the assumption of white noise can be found in [43].

The adaptive Kalman filter might be used in applications where tuning of the Kalman filter is uncertain at initialization, see [33], [37] and [38]. For not real-time critical application, such as surveying, the estimate can be enhanced by use of a smoother. In Fraser and Potter [14] a forward-smoother was proposed while in [44] a backwards smoother was introduced. Another alternative to the EKF for nonlinear systems is the particle filter. Particle filters are independent of noise distribution and are based on sequential Monte Carlo estimation algorithms [11] and [20]. Hence, the main advantage of using Particle filter in nonlinear non-Gaussian systems. When compared to Kalman filter, Particle filters are more computationally demanding; hence in current navigation systems it is not often used.

2.2 Control Problem in Aerospace Vehicle

2.2.1 Dynamic Control

Aircraft are highly non-linear systems, but flight control laws are traditionally designed from a set of linearised models. Due to the application of linear control laws on a non-linear system, the real performance ability of the aircraft is not fully utilised. In addition, in adverse situations like near stall, the aircraft develops significant non-linearities, and linear control laws do not perform well. The current state-of-the-art automatic flight control system (AFCS) provides efficient methods for pilots to fly the aircraft. The introduction of the fly-by-wire (FBW) system has enabled the aircraft to be stabilised automatically without pilot's input within the aircraft's performance envelope [16]. However, in the critical conditions, where the aircraft gets outside the flight envelope the automatic flight control known as 'Autopilot' is disengaged, and the pilot is required to take manual corrective actions. An example of critical conditions of this kind is when the aircraft reaches critical angle of attack (or stall angle), beyond which the lift is suddenly reduced. This phenomenon is known as stall. The standard stall recovery procedure recommended in the pilot training is to push the control stick down, forcing a nose down motion of the aircraft. This makes the aircraft go faster and restores the required lift [50]. Pilots tend to misread the situation and take wrong corrective measure leading to an accident. A significant number of commercial and military air crash accidents have occurred after loss of control due to stalling caused by pilot error. Indonesia AirAsia Flight 8501, Air France Flight 447, Navy McDonnell-Douglas QF-4S+ Phantom II and United States Air Force Boeing C-17A Lot XII Globemaster III are some recent air accidents caused by pilot error and stall [1].

Flight control laws below the stall angle are designed using linear control design methods such as gain scheduling [16]. The control laws are designed at many flight-operating points [32] and the gain scheduling is chosen as a function of mass, Mach number and altitude. This design procedure requires a great amount of assessment to ensure the adequate stability and performance at off design points. It is time-consuming and the performance capabilities of the aircraft are not fully realised. As an alternative to gain scheduling robust control algorithms such as $\mathcal{H}_2$ and $\mathcal{H}_\infty$ controllers are proposed [47]. However, at a large angle of attack (near the stall angle) aircraft develop significant non-linearities [54] and the linearised control laws does not perform well. An alternative approach is to apply non-linear design techniques, such as nonlinear dynamic inversion (NDI), in critical flight conditions such as near stall point or high attitude angle (pitch angle) manoeuvres where the aircraft develops nonlinearities. NDI directly make use of the non-linear structure of the aircraft model. It uses dynamic models and state feedback to globally linearise dynamics of selected controlled variables by cancelling the non-linearities in the dynamic model. As a result, the NDI method is capable of handling large nonlinearities. NDI control law

is designed to globally reduce the dynamics of selected controlled variables to integrators. A closed loop system is then designed to make the control variables exhibit specified command responses satisfying the flight-handling qualities and various physical limitation of the aircraft control actuators.

Flight control design using NDI was first proposed in the late 1970s [30], [36]. Since that time, a number of research efforts have been made to use non-linear control techniques for flight controls, e.g. as incremental NDI [51], adaptive fuzzy sliding control [41]. Various methods for analysing the robustness of the NDI flight controllers for a quasi-linear-parameter varying model were presented in [42]. Stochastic robust non-linear control using control logic for a high incidence research concept aircraft is proposed in [59].

2.2.2   Active Control for load alleviation

Aircraft wing structures are usually either manoeuvre-load or gust-load critical depending on whether the aircraft is a high performance-high manoeuvre aircraft or a transport type of aircraft. Although the design objectives differ for these two different types of aircraft, the underlying principle of redistribution of airload to reduce wing structural loads and structural weights is the same. Load alleviation systems using active control technologies had enabled weight reduction in aircraft by mitigating the structural loads to which the airframe is subjected as a result of manoeuvre demands or atmospheric disturbances.

The bending moment at the wing root joint of the aircraft is the principle determinator of the structural strength requirement at the wing root joints. The structural weight of the aircraft can be reduced if the wing root moment are reduced since less reinforcement are required to be used at the wing root joints. Thus, the structural weight reduction is directly related to the reduction of wing root moment. Active flight control system for load alleviation is particularly beneficial for reducing structural weight resulting from a few critical design points in the flight envelope where the highest wing root bending moment loads occur.

The Lockheed C-5A is one of the earliest examples of an aircraft incorporating active control to alleviate the detrimental effects of atmospheric disturbances. The C-5A aircraft suffered from fatigue life problems related to wing bending loads (Globalsecurity.org). Several load alleviation systems were evaluated on the C-5A aircraft, including a maneuver load alleviation system and a passive alleviation system that simply biased the aileron deflections upward to reduce wing bending load [8]. The Lockheed L-1011-500 aircraft included an Active Control System (ACS) to provide maneuver load alleviation (MLA) and gust load alleviation (GLA) without significant structural modification [26]. Wingtip and fuselage forward and aft vertical accelerometers as

well as fuselage pitch gyroscopes were added to the aircraft to support the ACS. The horizontal stabilizers and ailerons were used for control effectors [26].

Recent commercial aircraft have taken advantage of earlier advancements in active control for gust alleviation, although very little information is available in the public domain. The Airbus A320 aircraft (introduced in 1987) (Airbus, of the European Aeronautic Defence and Space Company EADS N.V., Netherlands) originally featured a Load Alleviation Function (LAF), which was later removed and was not incorporated into the Airbus A321, A319 aircraft, nor A318 aircraft. The LAF functionality has recently been reintroduced on some in-service A320 airplanes to allow a 1.3-percent increase in maximum takeoff weight [61]. The Airbus A330 aircraft (introduced in 1994) and the Airbus A340 aircraft (introduced in 1993) incorporated maneuver load alleviation systems as well as a flying quality enhancement system known as Comfort in Turbulence, or CIT. The objective of the CIT system was to increase the fuselage damping response (at 2.0 to 4.0 Hz) by actively controlling the rudder and elevators [24]. The Airbus A380 aircraft (introduced in 2007) also features a form of GLA system [39]. The Boeing 787 aircraft (introduced in 2011) is reported to use a MLA system as well as a flying quality enhancement system [40]. The flying quality enhancement system incorporates "static air data sensors" to detect the onset of lateral and vertical turbulence and uses ailerons, spoilers, and elevons to counteract the turbulence [40].

Current Gust Load Alleviation systems work primarily on the error feedback principle [2]. The first peak in the wing root moments (induces maximum load in the construction) determines the required sizing of the wing root joint reinforcement. Potential weight savings can be realized if the reduction in wing root moments is achieved. What is of special concern is therefore the 1st peak's reduction in the wing root moments, which is regarded as non-achievable by purely feedback solution [60]. Therefore combined feedforward plus feedback control can significantly minimize structural deflection due to air turbulence such as gusts [62]. If the sensors are placed smartly they could measure the r.m.s.(root mean square) vertical acceleration (along z-axis) at a number of locations on the aircraft. In order to precisely determine the effects of the wing bending relative to the center of gravity (CG) of the aircraft sensors are to be placed at the CG, wing tip right node and wingtip left node in principle. A related detailed treatment on optimal placement of sensors for this problematic issue is outlined in [21].

Chapter 3

Calibration of a Cost-effective Inertial Sensor

3.1 Summary of the contributions

In this chapter a "easy to do" calibration method for a cost-effective Multi-sensor Inertial Measurement Unit is presented. A calibration procedure focused on multi-sensor inertial measurement unit utilizing a modified sensor frames was analysed and evaluated. Unlike the common IMUs which consist of 3-axial accelerometer and gyroscope frames, the proposed concept of the multi-sensor unit consists of ten modified accelerometer frames supplemented by an unmodified ARS frame. The proposed IMU includes four 3-axial ACCs supplemented by six 2-axial ACCs and three regular 3-axial ARS frame all mounted on different PCBs (Printed Circuit Boards), the calibration procedure required to coincide all these different frames into one main IMU frame. The proposed approach is unique in the sense of calibrating a modified sensor frame into one main frame while evaluating scale factors, bias offsets, and misalignment angles of all ACCs. A cost effective stand-alone solution to the calibration procedure which does not require any precise knowledge of orientation and motion solution is proposed. The approach is experimentally verified and results confirm its effectiveness.

3.2 Publication

The work is represented by a publication with modified formatting and follows on the next page.

Calibration of a Multi-sensor Inertial Measurement Unit with Modified Sensor Frame

Mushfiqul Alam, Martin Sipos, Jan Rohac, Jakub Simanek
Department of Measurement
Czech Technical University in Prague, Faculty of Electrical Engineering
Prague, Czech Republic

Abstract— **Calibration of the inertial measurement units (IMU) used in navigation systems are crucial for ensuring accuracy of a navigation solution. It is common to discuss what calibration means, techniques, and algorithms can be utilized and implemented. For cost-effective measurement units it is desirable to use calibration means and approaches which are not expensive yet capable of providing sufficient accuracy. This paper thus focuses on multi-sensor inertial measurement unit which utilizes a modified sensor frames. Unlike the common IMUs which consist of 3-axial accelerometer and gyroscope frames, the proposed concept of the multi-sensor unit consists of ten modified accelerometer frames supplemented by an unmodified gyro frame. The modified frames of accelerometers are optimized for differential analogue signal processing in order to increase signal-to-noise ratio and hence overall sensing precision. Since the proposed concept of the measurement unit includes higher number of sensing frames it is required to develop a novel "easy to do and implement" calibration method which is the contribution of this paper. The proposed calibration approach was experimentally verified and results confirmed its usability.**

Keywords—accelerometers; gyroscopes; inertial measurement unit; calibration

I. INTRODUCTION

Inertial sensors such as accelerometers (ACCs) and gyroscopes (gyros) form the core of Inertial Measurement Units (IMUs) which are utilized in navigation systems. Such navigation systems can be widely used for estimating position, speed, and attitude in areas such as space, aerial or terrestrial vehicles, submarines etc. The grade of the IMU can vary based on the implemented sensors. In terms of stable and precise sensors, at least tactical grade ones are considered, they can be for instance ring laser gyros or fiber optic gyros, and servo or quartz accelerometers. These technologies are however expensive and thus in cost-effective applications MEMS (Micro-Electro-Mechanical System) technology is preferred. Nevertheless, this technology suffers from limited sensitivity, resolution, and error sources causing noisy time varying output. Of course, it also brings benefits for example in small size of sensors, low power consumption, and cost-effective implementation. Since the sensitivity of low-cost ACCs are limited by the resolution of about 0.1 up to 1 mg there was an effort to modify the ACC measuring or sensing frame to increase the accuracy of ACC based attitude estimation. This idea originates from our previous work published in [1]. Our original motivation led in the concept of a modified multi-

sensor IMU which is composed as shown in Fig. 1 and explained in more details in Section II.

In any case, no matter which sensor technology is used, it is always crucial to perform the calibration on each IMU. The process of calibration can vary based on the available facilities. For cost-effective solutions expensive calibration means are not suitable as such alternative cost-effective and easy to implement approaches are recommended. Common approaches providing the calibration of conventional 3D sensing frames in IMUs can be found in [2], [3], [4]; however, the contribution of this paper lies in proposing a novel "easy to do and implement" calibration procedure suitable for our previously developed multi-sensor IMU with a modified ACC frame. Since the proposed IMU includes four 3-axial ACCs supplemented by six 2-axial ACCs and three regular 3-axial gyros frame all mounted on different PCBs (Printed Circuit Boards), the calibration procedure requires to coincide all these different frames into one main IMU frame. The proposed approach is unique in the sense of calibrating a modified sensor frame into one main frame.

The rest of the paper is organized as follows. Section II outlines the proposed concept of the multi-sensor IMU in details. Section III provides description of data filtering and processing to obtain sensor error models and the calibration procedures which is followed by experimental results provided in Section IV. The paper is concluded in Section V.

II. IMU CONCEPT

The modified configuration of the multi-sensor IMU consists in total of six 2-axial analogue ACCs ADXL203, four 3-axial analogue ACCs ADXL337 and thee 1-axis digital gyros ADIS16136. As shown in Fig. 1, on the mainboard four ADXL337 ACCs and two 2-axial ADXL203 ACCs are placed. Other four ADXL203 ACCs are placed at side boards, and three digital single axis gyroscopes ADIS16136 are placed in the regular way on each PCBs. Fig. 1 shows a concept scheme of the proposed IMU solution. At each side board, a gyroscope and two 2-axial ACC are placed. At each side board, 2-axial ACCs are placed in a way that its sensitive axes are pointing at 45 degrees with respect to the main board axis Z. The resultant of each 2-axial ACC is computed as the difference between its individual axes respecting the orientation depicted in Fig. 1, see resultants denoted as R_1-R_6. This concept of modified ACC frame brings benefits in sensing the gravity vector by ACCs with low sensor resolution about 1mg under conditions when

1984

the main board is close to be horizontal. The main board additionally includes two 2-axial ACCs for improved sensing of translational acceleration along the main board X and Y axes. This design principle was presented in the form of the patent [5].
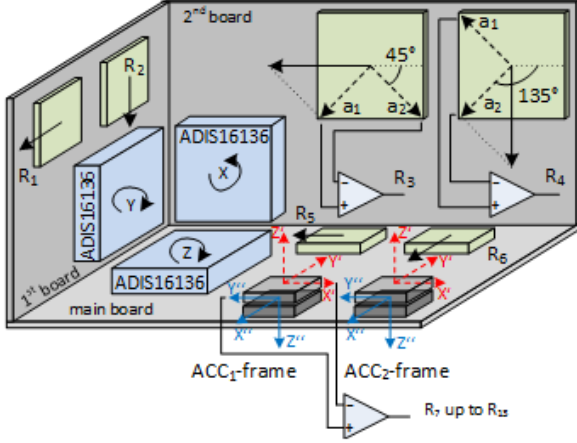

Fig. 1. Concept scheme of proposed IMU solution.

Each sets of two 3-axial ACCs ADXL337, denoted as ACC_1 and ACC_2 frame, forms pairs of sensitive axes. They are aligned to the main board axes X, Y, Z in such a way that when an acceleration is applied, it affects both ACCs with coupled axes the same way for a particular main axis (X, Y or Z) but with opposite signs. There are two couples of ADXL337 ACCs and resultant accelerations are denoted as R_7-R_{12}.

All boards include 8-channel 16-bit analogue-to-digital convertors AD7689 to digitalize ACC resultants R_1-R_6 and R_7-R_{12}. All resultants are performed by instrumentation amplifiers AD8222 which provide subtraction within the particular ACC pairs. The data are sampled by frequency of 1 kHz and then processed in microcontroller STM32F405 (STMicroclectronics). Processed data are available through CAN (Controller Area Network) bus for enhanced data fusion to obtain a navigation solution. The data from gyros are processed with the same sampling frequency.

The proposed concept of this IMU is advantageous in terms of ACC signals handling due to increased Signal-to-Noise Ratio (SNR) and thus accuracy of the overall acceleration measurement. A hardware realization of the proposed IMU is shown in Fig. 2.
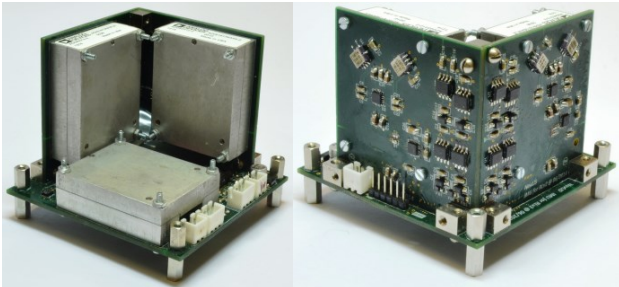

Fig. 2. Hardware realization of proposed IMU.

III. DATA PROCESSING

A. Principles of ACC signals differential processing

In the case of 2-axial ACCs each output pair is led into an instrumentation amplifier to perform subtraction

$$U_1 - U_2 = U_{10} \pm \Delta U_1 - U_{20} \mp \Delta U_2$$
$$= U_{10} - U_{20} \pm (\Delta U_1 + \Delta U_2), \quad (1)$$

where U_i corresponds to outputs of an ACC pair,
U_{i0} is a DC value when no acceleration is applied,
ΔU_i reflects the output change when acceleration applied.

Given IMU is horizontal, when opposite directions of sensitive axes within an ACC pair are considered and $U_{10} - U_{20} = 0$ in ideal case, the Eq.1 can be rewritten into the form

$$U_1 - U_2 \approx \Delta U_1 + \Delta U_2 = 2\Delta U \approx 2a_i, \quad (2)$$

where a_i is an applied acceleration in i-axis of the main board frame.

When noise is considered with respect to (1-2) the resulting value σ_{Ti} can be evaluated as

$$\sigma_{Ti} = \sqrt{\sigma_{1i}^2 + \sigma_{2i}^2}, \quad (3)$$

where σ_{Ti} is a standard deviation of combined signal with respect to the individual signal standard deviation.

From (2-3) there can be seen that the sensitivity was doubled and the noise level increased, but not two times. That improves the signal to noise ratio (SNR). In the case of 3-axial ACCs the situation is similar, but it cannot use the advantage of the condition $U_{10} - U_{20} = 0$, because a pair consists of axes from different sensors.

B. Sensor Error Models

The proposed unconventional IMU cannot be entirely calibrated using common calibration techniques as explained in [2], [3], [4], [6]. The motivation is thus to calibrate and align 10 ACC individual frames (four 3-axis and six 2-axis) into one corresponding main board X, Y, Z frame and complete the calibration by aligning the gyros sensitive axes with the main frame. For calibration purposes we utilized a common sensor error model (SEM) for 3-axial ACCs and gyros presented in details in [2], [7]. The procedure includes the SEM estimation covering scale factors, an orthogonalizing matrix respecting Fig. 3, bias offsets, plus a misalignment matrix in the case of the gyros. For the calibration of the 2-axial ACCs we propose a novel SEM estimation and calibration technique.
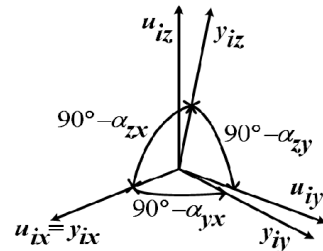

Fig. 3. Relationship between y_i – non-orthogonal frame and u_i – orthogonal frame, where i denotes the sensor triad which is being calibrated.

The SEM for 3-axial ACCs can be defined as

$$u_a = T_a S_a (y_a - b_a) =$$
$$\begin{bmatrix} 1 & 0 & 0 \\ \alpha_{xy} & 1 & 0 \\ \alpha_{zx} & \alpha_{zy} & 1 \end{bmatrix} \begin{bmatrix} S_{ax} & 0 & 0 \\ 0 & S_{ay} & 0 \\ 0 & 0 & S_{az} \end{bmatrix} \left(\begin{bmatrix} y_{ax} \\ y_{ay} \\ y_{az} \end{bmatrix} - \begin{bmatrix} b_{ax} \\ b_{ay} \\ b_{az} \end{bmatrix} \right), \quad (4)$$

for 2-axial ACCs as

$$u_R = T_R S_R (y_R - b_R) =$$
$$\begin{bmatrix} 1 & 0 \\ \alpha_R & 1 \end{bmatrix} \begin{bmatrix} S_{R1} & 0 \\ 0 & S_{R2} \end{bmatrix} \left(\begin{bmatrix} y_{R1} \\ y_{R2} \end{bmatrix} - \begin{bmatrix} b_{R1} \\ b_{R2} \end{bmatrix} \right), \quad (5)$$

and for 3-axial gyros as

$$y_g - b_g = S_g T_g M_g u_g$$
$$= \begin{bmatrix} S_{gx} & 0 & 0 \\ 0 & S_{gy} & 0 \\ 0 & 0 & S_{gz} \end{bmatrix} \begin{bmatrix} 1 & 0 & 0 \\ \alpha_{xy} & 1 & 0 \\ \alpha_{zx} & \alpha_{zy} & 1 \end{bmatrix} \begin{bmatrix} c_\theta c_\psi & -c_\phi s_\psi + s_\phi s_\theta c_\psi & s_\phi s_\psi + c_\psi s_\theta c_\psi \\ c_\theta s_\psi & c_\phi c_\psi + s_\phi s_\theta s_\psi & -s_\phi c_\psi + c_\phi s_\theta s_\psi \\ -s_\theta & s_\phi c_\theta & c_\phi c_\theta \end{bmatrix}^T \begin{bmatrix} u_{gx} \\ u_{gy} \\ u_{gz} \end{bmatrix}$$
$$(6)$$

where u_a, u_R, y_g are the vectors of measured accelerations and angular rates; S_a, S_R, S_g are the scale factor matrices; T_a, T_R, T_g are transformation matrices from non-orthogonal frame to orthogonal frame; $b_a. b_R, b_g$ corresponds to the offset vectors; u_g is the vectors of referential angular rates; M_g denotes the misalignment matrices between the gyro orthogonal frame and the main board frame; ψ, θ, ψ are the Euler angles, and c & s correspond to *cosine* and *sine* functions.

C. Calibration of 3-Axial Accelerometers

The 3-axial ACC calibration is performed from data obtained at various orientations under the condition when the sensors are affected only by the gravity. The sensor values are obtained by rotating the sensor along each the main board axis (X, Y, Z) and taking at least two readings per quadrant. Thus it means 24 orientations in total. According to the Thin-Shell method [8] and accuracy analyses presented in [2], it is recommended to measure the ACC outputs in more than 21 orientations. An advantage of this approach is that no precise knowledge about particular orientations is required. The SEM in (4) can be minimized with respect to the Root Mean Square Error (RMSE) defined as

$$RMSE = \sqrt{\frac{\sum_{i=1}^{n}(|a_i(x)| - G)^2}{n}}, \quad (7)$$

where $x = (S_{ax}, S_{ay} \dots b_{ay}, b_{az})$ is m- dimensional vector of unknown parameter, n −number of performed orientations. G is the magnitude of the gravity equal to 1 g; and $|a_i(x)|$ is the magnitude of the estimated acceleration vector. The minimization criterion can use for instance Gauss-Newton algorithm [9], Merayo's algorithm [10], Quasi-Newton factorization algorithm [10], or Levenberg Marquardt algorithm [2].

D. Calibration of 3-axial Gyroscope

As in the case of ACC calibration a similar procedure can be performed for gyro calibration just with a limitation that the Earth rate is measurable, which is in cases of high resolution gyros. For MEMS gyros the resolution is not sufficient, and thus other approach is needed. In our case the gyros triad calibration relies only on three successive rotations along all main board axes X, Y, Z. They are performed individually and for each rotation angular rates from the triad are to be measured as well as the referential rotated angle. This angle can be evaluated for example with already calibrated ACCs as explained in section III.BC. One strict condition for this calibration approach is that the gyro rotation requires to be only along horizontally aligned axis with accuracy better than 0.5 deg, for details see [1].

An implemented algorithm for gyro SEM estimation, see (6), utilizes the Cholesky decomposition and the LU (Lower Upper) factorization. When all three perpendicular rotations are performed and angular rates measured, the angular rates are compensated for the offsets which have been estimated as a mean value of output readings when sensors are kept under steady-state conditions, which gives u_g and y_g. The calibration algorithm is performed in an angle domain which means angular rates are integrated to obtain angles. Integrating y_g gives full 3x3 Y_g matrix of integrated angles and integrating u_g a diagonal matrix U_g of referential angles. By rearranging the gyro SEM model in (6) can be then evaluated as

$$(Y_g U_g^{-1}) = S_g T_g M_g, \quad (8)$$

Eq(8) can be further simplified to eliminate M_g as

$$(Y_g U_g^{-1})(Y_g U_g^{-1})^T = (S_g T_g)(S_g T_g)^T \quad (9)$$

The lower triangular matrix $(S_g T_g)$ can be found by Cholesky decomposition as in (10) followed by LU factorization to find S_g and T_g matrix as (11)

$$(S_g T_g) = chol((Y_g U_g^{-1})(Y_g U_g^{-1})^T) \quad (10)$$

$$[S_g, T_g] = LU(S_g T_g), \quad (11)$$

where LU denotes the LU factorization; The matrix M_g can be then obtained by

$$M_g = T_g^{-1} S_g^{-1} Y_g U_g^{-1}, \quad (12)$$

E. Calibration of 2-axial Accelerometer

The calibration of 2-axial ACCs are performed by three successive rotation of the IMU along its main axes (X, Y, Z). In theory, while rotating a pair of 2-axial ACC along the main axis which are placed at the same PCB; the resultant accelerations output will form a circle with radius equal to $\sqrt{2}g$. For the minimization criterion a modified RMSE error formulation is defined as

$$RMSE = \sqrt{\frac{\sum_{i=1}^{n}(|R_i(x)| - |a_i(x)|)^2}{n}},$$ (13)

where $R_i(x)$ is the resultant acceleration from the 2-axial ACCs on the same PCB and $|a_i(x)|$ is the acceleration from the already calibrated ACC_1 or ACC_2.

F. Signal filtering

Raw digitalized ACC and gyro data in the proposed IMU are sampled at 1 kHz even when a final implementation of navigation equations is intended to operate at 100 Hz. This oversampling capability allows better signal processing. We proposed three FIR digital low-pass filters to be used in real time to filter the raw data with the decimation factor equal to 10. When designing the filters, we aimed for the flat and zero-gain pass-band, and at least 40 dB attenuation of the high-frequency stop-band. The resulting filters are labeled as follows: Filter 1 (*Parks-McClellan* type, bellow 0.5 % pass-band ripple), Filter 2 (*equiripple* type designed in MATLAB *FDATool*), and Filter 3 (*Bartlett*, two cascaded averaging filters that provide a Bartlett window FIR filter response).

The resulting frequency and step response of these three filters are shown in Fig. 4 and Fig. 5. Filter parameters, such as cut-off frequency, stop-band frequency with attenuation at least 40 dB, and delay in samples are listed in Table I.
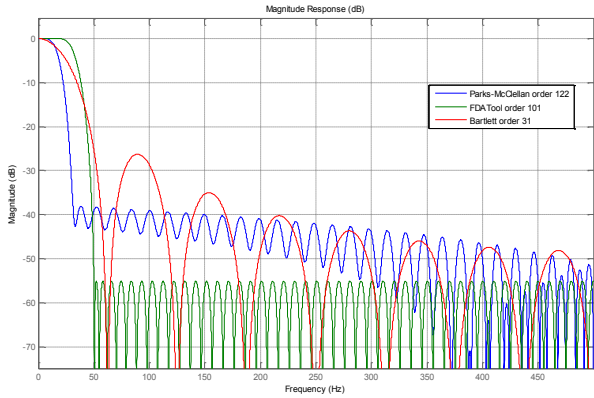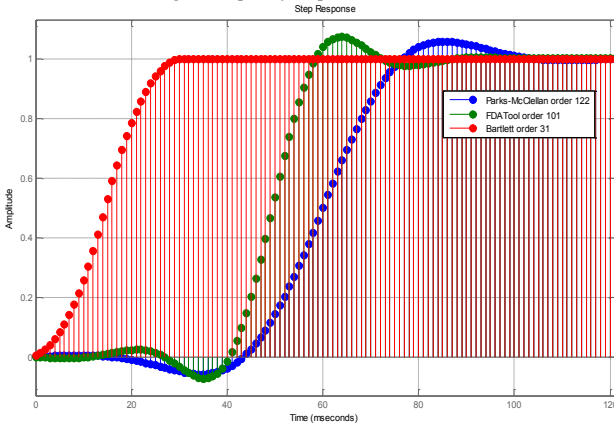

Fig. 4 Frequency response of FIR filters

Fig. 5 Step response of the FIR filters.

TABLE I. FILTER PARAMETERS FILTER 1: PARKS-MCCLELLAN, FILTER 2: FDATOOL, FILTER 3: BARTLETT

Parameter	Filter 1	Filter 2	Filter 3
$f_{\text{cut-off (-3 dB)}}$ (Hz)	10	30	20
$f_{\text{stop (-40 dB)}}$ (Hz)	31	48	56
Delay (samples)	60.5	50	15

IV. EXPERIMENTAL RESULTS

Before the calibration took place the IMU power was switched on and left to warm up to stabilize its thermal dependency. The 3-axial ACCs' data were recorded in 24 orientations under steady conditions to reduce the influence of random noise and the average was computed. After recording the data, the orientation values were implemented to the minimization criterion (7) to estimate the SEM defined in (4). The calibration results of 3-axial ACC are shown in Fig. 6. It can be noticed that mean RMSE value for the uncalibrated ACC-1 is very high (0.1359g) and it is not consistent, after the calibration the mean RMSE value falls down to (0.3mg) and it is consistent (linear) across the different orientations.
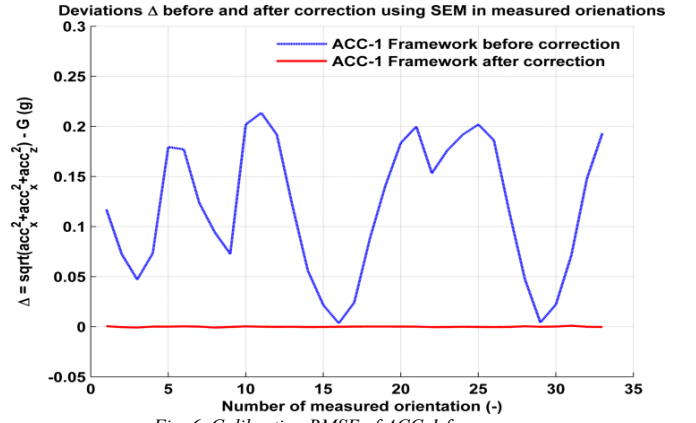
Fig. 6. Calibration RMSE of ACC-1 frame.

For the calibration of 2-axial ACCs the IMU was rotated successively along each three single axis in one direction with small intervals. It was ensured that the intervals were divided in such a way that at least 21 or more orientations were recorded. Then the minimization criterion defined in (11) was performed to fit the unit circle produced by the already calibrated ACC-1 frame. The calibration results are shown in Fig. 7 to Fig. 9. The comparison of the entire calibration process from 2-axial ACCs is depicted in Fig. 10, which shows deviations of subtracted accelerations before and after calibration. The mean RMSE value of the uncalibrated 2-axial ACC pair varies between 0.4129g to 0.4206g which is significantly high. After the calibration, the mean RMSE value varies from 0.0016g to 0.0041g, which is an obvious improvement to the IMU. TABLE II summarizes the RMSE values before and after calibration. The SEM values obtained via the calibration are summarized TABLE III.
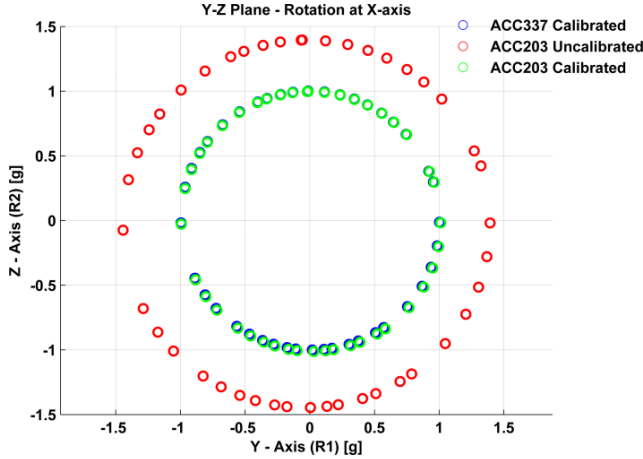
Fig. 7. Acceleration of the IMU during rotation along X-axis.
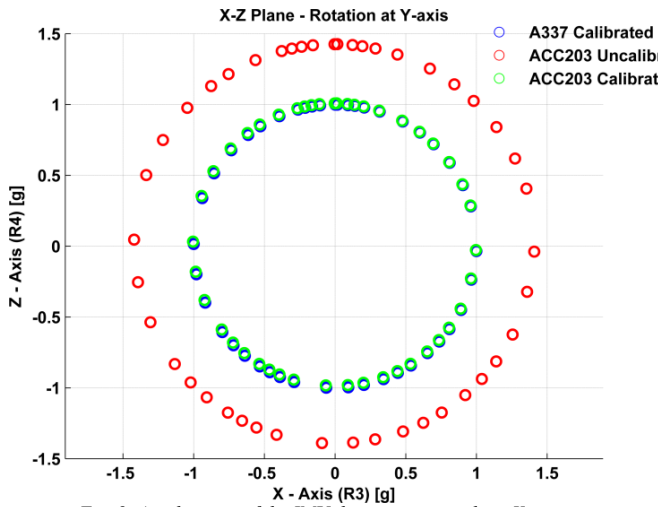
Fig. 8. Acceleration of the IMU during rotation along Y-axis.
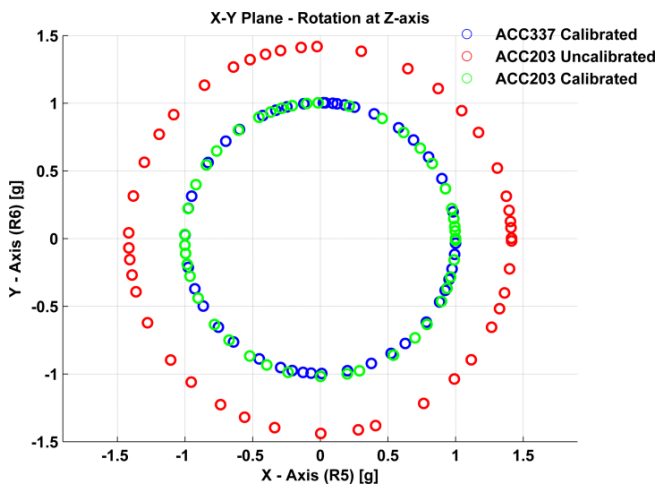
Fig. 9. Acceleration of the IMU during rotation along Z-axis.
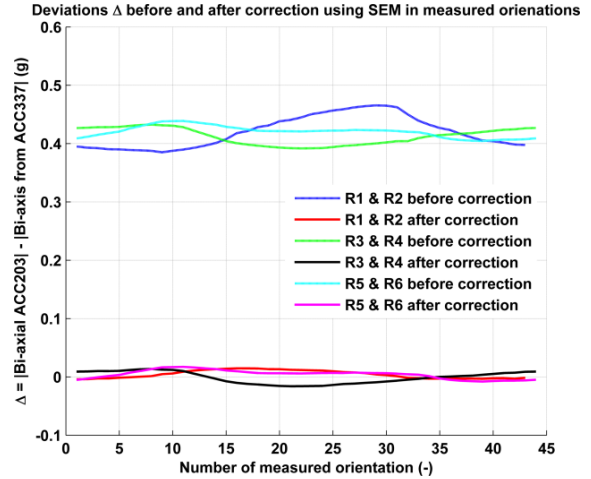
Fig. 10. RMSE of calibrated 2-axial frames defined by ACC pair's individual subtraction.

TABLE II. RMSE OF ACC FRAMES BEFORE AND AFTER CALIBRATION.

Accelerometers	RMSE before calibration (g)	RMSE after calibration (g)
ACC-1 frame	0.1359	0.0003
ACC-2 frame	0.1172	0.0006
2-axial frame [R_1R_2]	0.4206	0.0055
2-axial frame [R_3R_4]	0.4129	0.0041
2-axial frame [R_5R_6]	0.4206	0.0016

TABLE III. CALIBRATION VALUES OF THE ACC FRAMES.

|	ACC-1 Frame	ACC-2 Frame	ACC203 $R_{1,2}$	ACC203 $R_{3,4}$	ACC203 $R_{5,6}$
$S_x(-)$	0.9016	0.9018	--	0.7030	0.7070
$S_y(-)$	0.9076	0.9013	0.7030	--	0.6990
$S_z(-)$	0.9023	0.9092	0.7040	0.7110	--
$\alpha_{xy}(-)$	0.0012	0.0016	--	--	0.0059
$\alpha_{zx}(-)$	0.0160	-0.0178	--	0.0022	--
$\alpha_{zy}(-)$	0.0116	-0.0113	-0.0042	--	--
$b_{ax}(g)$	0.0897	0.0401	--	--	-0.0008
$b_{ay}(g)$	-0.056	0.0303	-0.0186	-0.0050	-0.0073
$b_{az}(g)$	0.0403	0.0324	-0.0175	0.0126	--

When all ACC frames are calibrated and align together, the gyro frame calibration can take place. Gyros, before they were calibrated, were kept in temperature balance to minimize the bias temperature dependency. Before the calibration the Z-axis of the IMU was aligned with the horizontal plane. It must be ensured that the plane of performed rotation is about horizontal within $\pm 0.5^o$ accuracy. The rest of rotations were performed along another axes aligned again horizontally with the already calibrated ACC frame. To estimate the gyro offsets the gyro outputs were measured under static conditions for approximately 30 seconds. Then successive rotations were applied and the gyro outputs were measured as well as the referential angle of rotation. The referential angles in the presented case were calculated from the already calibrated ACC-1 frame. These steps were repeated for each axis. The gyro calibration progressions are depicted in Fig. 11.

Fig. 11. Gyro output progressions during the calibration.

To evaluate the efficiency of proposed filtering process which was supposed to minimize the effect of sensor noise we applied all three proposed filters on all IMU output signals and observed the performance. The data were obtained u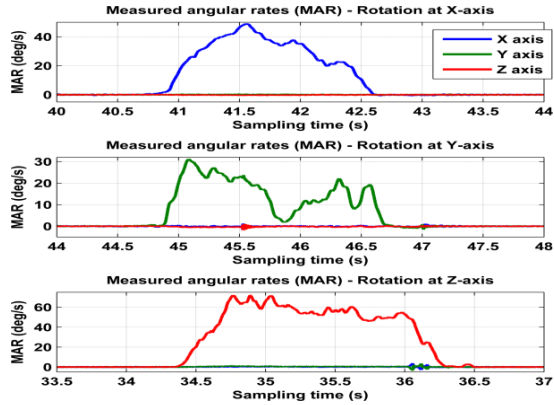nder steady conditions. In Table IV, there are listed standard deviations of measured and filtered data from all used sensors. The data out of brackets correspond to the sampling frequency of 1 kHz, and the data in brackets were decimated to get the update frequency of 100 Hz, which is the frequency used for consecutive navigation solutions.

TABLE IV. FILTER PERFORMANCE FILTER 1: PARKS-MCCLELLAN, FILTER 2: EQUIRIPPLE, FILTER 3: BARTLETT

Sensors	Standard deviation			
	Raw data	Filter 1	Filter 2	Filter 3
ACC-1 x (mg)	2.77	0.77 (0.76)	1.02 (0.98)	0.84 (0.82)
ACC-1 y (mg)	2.61	0.78 (0.78)	1.05 (1.02)	0.86 (0.84)
ACC-1 z (mg)	4.77	1.80 (1.76)	2.36 (2.24)	1.96 (1.88)
ACC203 x (mg)	2.12	0.90 (0.88)	1.15 (1.11)	0.97 (0.93)
ACC203 y (mg)	1.97	0.80 (0.79)	1.08 (1.05)	0.88 (0.86)
Gyro x (°/s)	0.111	0.043 (0.042)	0.046 (0.045)	0.044 (0.042)
Gyro y (°/s)	0.105	0.020 (0.018)	0.025 (0.024)	0.021 (0.020)
Gyro z (°/s)	0.102	0.018 (0.017)	0.024 (0.022)	0.019 (0.018)

Given the filter parameters and results in Table II and Table IV, respectively, Bartlett window FIR filter was selected for filtering of raw ACC and gyro readings sampled at 1kHz. Thus, the output obtained has sufficient attenuation and the lowest delay out of three proposed filters.

The proposed calibration principles and methods of the modified multi sensor IMU is easy to carry out and does not require any expensive precise equipment. Hence it provides a quick and cheap calibration procedure for the proposed IMU which offers potential cost saving. In addition the performance of the IMU is significantly improved with respect to the RMSE error reduction.

V. CONCLUSION

This paper proposes a novel approach to calibration when a multi-sensor inertial measurement unit with modified sensor frame is utilized. The proposed unit consists of ten accelerometers (ACCs) with individually modified frames and one unmodified gyro frame. The ACC frames are optimized in order to perform differential signal processing which increases signal-to-noise ratio and thus improves overall precision of acceleration sensing when low-cost ACCs are used. Therefore, the proposed calibration approach required aligning all individual frames into one main axes and evaluate scale factors, bias offsets, and misalignment angles of all ACCs used plus coincide the ACC frame and gyro frame with the main body frame. The paper deals with cost-effective solution to the calibration solution which does not use any expensive means, but a stand-alone solution independent on any precise knowledge of orientation and motion which can be provided by only expensive calibration means. The approach was experimentally verified and results confirm its effectiveness. With respect to presented results the reached effectiveness is better than 99.5 % when uncalibrated and calibrated data are considered.

REFERENCES

[1] J. Rohac, "Accelerometers and an Aircraft Attitude Evaluation," in *In IEEE Sensors 2005 - The 4-th IEEE Conference on Sensors [CD-ROM]. CA: IEEE Sensors*, Irvine, 2005.

[2] P. Paces, M. Sipos and J. Rohac, "Analyses of Triaxial Accelerometer Calibration Algorithms," *IEEE Sensors Journal,* vol. 12, no. 5, pp. 1157-1165, 2012.

[3] Z. Syed, P. Aggarwal, C. Goodall, X. Niu and N. El-Sheimy, "A new multi-position calibration method for MEMS inertial navigation systems," *Measurement Science & Technology,* vol. 8, no. 7, pp. 1897-1907, 2007.

[4] A. Kim and F. Golnaraghi, "Initial Calibration of an Inertial Measurement Unit Using Optical Position Tracking System," in *PLANS 2004: Position Location and Navigation Symposium*, 2007.

[5] J. Rohac, "Measurement Unit of an Artificial Horizon". Czech Republic Patent PUV 2011-24979, 16 01 2012.

[6] S. Won and F. Golnaraghi, "A Triaxial Accelerometer Calibration Method Using a Mathematical Model," *IEEE Transactions on Instrumentation and Measurement,* vol. 8, no. 9, pp. 2144-2153, 2010.

[7] D. Jurman, R. Jankovec, R. Kamnik and M. Topic, "Calibration and data fusion solution for the miniature attitude and heading reference system," *Sensors and Actuators A : Physical,* vol. 138, no. 2, pp. 411-420, 2007.

[8] M. Sipos, J. Rohac and P. Novacek, "Improvement of Electronic Compass Accuracy Based on Magne-tometer and Accelerometer Calibration," *Acta Physica Polonica A,* vol. 121, no. 4, pp. 945-949, 2012.

[9] I. Skog and P. Handel, "Calibration of a MEMS Inertial Measurement Unit," in *XVII IMEKO World Congress*, Rio de Janeiro, Brazil, 2006.

[10] S. Bonnet, C. Bassompierre, C. Godin, S. Lesceq and A. Barraud, "Calibration Methods for Inertial and Magnetic Sensors," *Sensors and Actuators A : Physical,* vol. 156, no. 2, pp. 302-311, 2009.

[11] K. E. Donald, Optimal Control Theory: An Introduction, California: Dover Publications, 2004.

Chapter 4

Adaptive Pre-processing of Inertial Sensor's Data using Variable Bandwidth

4.1 Summary of the contributions

This chapter outlines on the adaptive data pre-precessing of the inertial sensors. A novel concept in adaptive data pre-processing for attitude and heading reference system (AHRS) which is primarily estimated using only inertial sensors (ACCs and ARSs) is proposed. The novelty lies in proposing an adaptive data pre-processing by using a variable bandwidth filtering when sensor's data are affected by significantly strong vibration while operating under harsh environments. This approach utilizes sinusoidal estimation to continuously adapt the filtering bandwidth of the accelerometer's data in order to reduce the effects of vibration and sensor noise before attitude estimation is processed. Low frequency vibration generally limits the conditions under which the ACCs can be used to aid the attitude estimation process, which is primarily based on ARS data and, thus, decreases its accuracy. In contrast, the proposed pre-processing technique enables using ACCs as an aiding source by effective data smoothing, even when they are affected by low frequency vibration. The proposed concept is verified via simulation and real-flight test.

4.2 Publication

The work is represented by a publication with modified formatting and follows on the next page.

Article

Adaptive Data Filtering of Inertial Sensors with Variable Bandwidth

Mushfiqul Alam * and Jan Rohac

Department of Measurement, Faculty of Electrical Engineering, Czech Technical University in Prague, Technicka 2, Prague 16627, Czech Republic; E-Mail: jan.rohac@fel.cvut.cz

* Author to whom correspondence should be addressed; E-Mail: mushfala@fel.cvut.cz; Tel.: +420-22435-2061; Fax: +420-233-339-929.

Abstract: MEMS (micro-electro-mechanical system)-based inertial sensors, *i.e.*, accelerometers and angular rate sensors, are commonly used as a cost-effective solution for the purposes of navigation in a broad spectrum of terrestrial and aerospace applications. These tri-axial inertial sensors form an inertial measurement unit (IMU), which is a core unit of navigation systems. Even if MEMS sensors have an advantage in their size, cost, weight and power consumption, they suffer from bias instability, noisy output and insufficient resolution. Furthermore, the sensor's behavior can be significantly affected by strong vibration when it operates in harsh environments. All of these constitute conditions require treatment through data processing. As long as the navigation solution is primarily based on using only inertial data, this paper proposes a novel concept in adaptive data pre-processing by using a variable bandwidth filtering. This approach utilizes sinusoidal estimation to continuously adapt the filtering bandwidth of the accelerometer's data in order to reduce the effects of vibration and sensor noise before attitude estimation is processed. Low frequency vibration generally limits the conditions under which the accelerometers can be used to aid the attitude estimation process, which is primarily based on angular rate data and, thus, decreases its accuracy. In contrast, the proposed pre-processing technique enables using accelerometers as an aiding source by effective data smoothing, even when they are affected by low frequency vibration. Verification of the proposed concept is performed on simulation and real-flight data obtained on an ultra-light aircraft. The results of both types of experiments confirm the suitability of the concept for inertial data pre-processing.

21

1. Introduction

Recently, there has been a growing trend toward using cost-effective MEMS (micro-electro-mechanical system) technology-based sensors for navigation purposes in aerospace systems, such as on light aircrafts and unmanned aerial vehicles (UAVs). A strapdown inertial system consisting of tri-axial accelerometers (ACCs) and tri-axial angular rate sensors (ARSs) is commonly used for attitude estimation (roll, pitch, yaw angle), as well as for velocity and position evaluations. On large aircraft, ring laser gyros and servo ACCs are used on board for precise measurements, which is expensive. In comparison, MEMS sensors are compact, lightweight and cost effective, thus offering an inexpensive solution for navigation purposes. However, at the same time, MEMS-based inertial sensors suffer from bias instability, insufficient sensitivity, noise, *etc.*, which present significant challenges in data processing that have to be dealt with in navigation processes. Originally, the attitude was supposed to be evaluated by integrating angular rates; nevertheless, as mentioned before, the measurements suffer from several inaccuracy impacts. In the case of the ARS-based attitude evaluation process, this inaccuracy causes unbound error growth, which needs to be corrected by data obtained from so-called aiding systems, e.g., magnetometers, cameras and even ACCs. These aiding systems provide information about attitude only under certain conditions, limiting their usability. This paper focuses on data pre-processing for navigation solutions based on inertial sensors only (ARSs and ACCs). Therefore, the ARS-based attitude evaluation process is primarily aided by ACC-based attitude evaluation [1]. This aiding can be applied under conditions when only gravity affects ACC measurements and no other acceleration is present [2–4]. This principle is common in cost-effective solutions of attitude and heading reference systems (AHRSs); however, these ideal aiding conditions are hardly achievable in harsh environments, due to strong vibrations present on light or small aircrafts. This complicates the situation, as the frequency of those vibrations cannot be simply isolated from the aircraft dynamics. The ARSs are primarily used for attitude evaluation, unlike the ACCs, which are utilized in AHRS just for attitude compensation.

To learn the characteristics of real flight conditions, several flight experiments were performed using IMU ADIS16350 (Analog Devices, Norwood, MA, USA), which was utilized in the EFIS INTEGRA TL-6524 (Electronic Flight Instrumentation System) ,flight monitoring system manufactured by TL-Elektronic, Inc. (Hradec Králové, Czech Republic) The system was mounted to the instrument panel of the ATEC321 aircraft (ATEC321 is a Czech ultra-light aircraft, designed and produced by ATEC v.o.s, Libice nad Cidlinou, Czech Republic). The instrument panel was equipped neither with active nor passive vibration dampers. As a result, the sensors were directly affected by strong structural vibrations. Measurements were made for different flight phases, such as parking, taxing on the runway, taking off, during the flight and landing. The data were recorded at a sampling frequency of 43 Hz. The worst situation corresponds to the case when the vibration impact cannot be distinguished and isolated from the aircraft dynamics. Such a situation is depicted in Figures 1 and 2, which show the flight data from

22

ACC and ARS measured during the engine revolution per minute (RPM) suppression and their frequency spectrum.
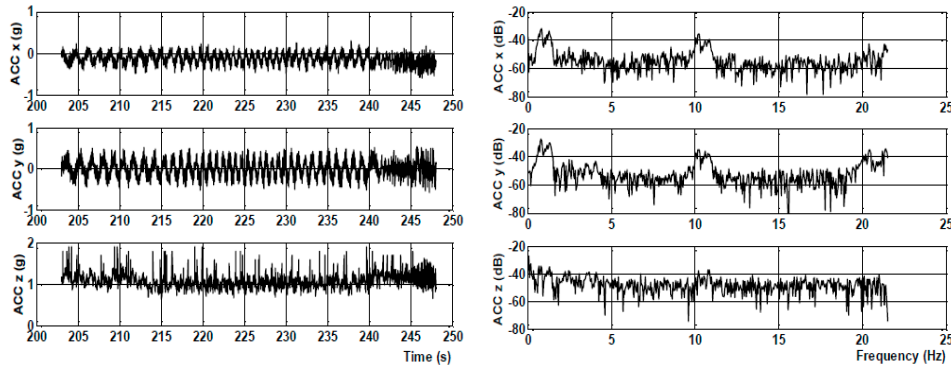
Figure 1. Accelerometer (ACC) measured during engine suppression and the frequency spectrum.
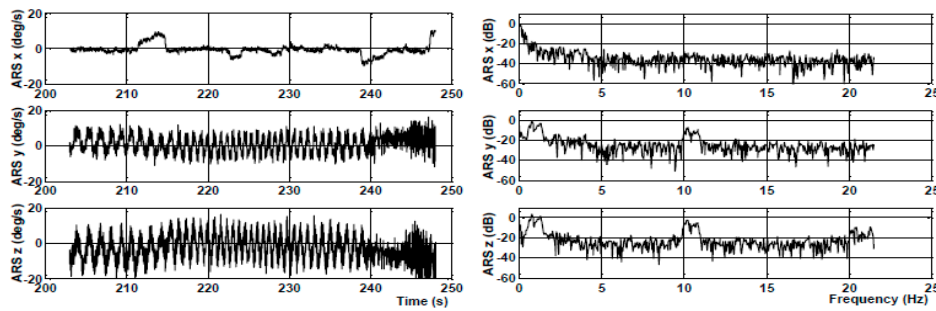
Figure 2. Angular rate sensor (ARS) measured during engine suppression and the frequency spectrum.

In cases of engine RPM suppression during the flight, vibration frequencies go down all the way to 0.5 Hz. ACCs are generally affected by the combination of translation, centrifugal and gravitational accelerations along with the vibrations arising from the propeller and the aircraft structure. The vibration effect often dominates the ACC measurements. In contrast, vibrations have slight impacts on ARS readings depending on g and g^2 sensitive parameters; contrariwise, their readings are affected by bias instability and noise. These different characteristics of ARS and ACC enable their data fusion to improve the final accuracy of the whole attitude estimation process. Generally, ARS data are always used to estimate attitude, even under dynamic conditions, when the aircraft is maneuvering or under steady flight conditions. Unlike ACC, data are directly utilized for the attitude compensation under only steady-state conditions when the gravity distribution in the sensor's framework can be estimated. This corresponds to situations in which the aircraft performs a direct and unaccelerated flight. In the cases where the aircraft undergoes a banked turn or a circular flight, a long-term additional acceleration is present due to the centripetal force created by traveling along a curved path. In such conditions, it is possible to estimate the centripetal acceleration and to subtract it out by providing the known velocity or airspeed to the data fusion process [5]. There exist several approaches to data fusion for attitude

estimation, such as temporally-interconnected observers (TIO) [6], complementary filters [7] or Kalman filters [8,9]. However, the accuracy of the estimation is always reduced, while the ACC data are affected by periodic vibration. This complicates the situation, due to a harsh environment causing structural vibrations, which are directly picked up by the ACCs. Therefore, for precise attitude estimation regardless of the aircraft flight condition, it is essential to provide acceleration data that are as smooth as possible with a reduced vibration effect; thus, ACC data require pre-processing. The light aircrafts are classified as Level I Class I, Category B Flight Phase (cruise, climb, descent, loiter) by the Federal Aviation Administration (FAA). The maximum time to achieve a change in the bank and pitch angle is 1.7 s, and the minimum time is 0.2 s [10,11]. This means that the aircraft's operational frequency lies in the range of 0.6 up to 5 Hz. In this instance, the ideal choice would be to apply a band-pass (BP) filter; nevertheless, such a narrow bandwidth would require a very high order filter, which is not desirable for navigation purposes, because of the long delays.

As mentioned, the aircraft dynamics lies in the range of 0.6 up to 5 Hz, and the vibration frequency might go all the way down to 0.5 Hz. Therefore, using a constant 5 Hz bandwidth low-pass (LP) filter would mean that the 0.5 Hz frequency vibrations will not be filtered. On the other hand, using a constant 0.6-Hz bandwidth LP filter would lead to a situation in which the aircraft's motion information in the bandwidth up to 5 Hz would be lost. Therefore, our contribution is a novel concept of pre-processing ACC data using adaptive bandwidth filtering, which is modified based on sinusoidal data estimation. The proposed filtering algorithm is adaptive in the sense that the filtering bandwidth is modified based on the signal history. This enables the usage of ACC-based attitude compensation, even under variable low-frequency vibration impacts, while common commercial AHRS systems fail to have the correct compensation capability. This proposed approach brings several advantages against the ones commonly used, such as a smaller and acceptable delay, even when the narrowest bandwidth of 0.5 Hz is applied on the ACC data. On the other hand, ARS data are filtered with a constant bandwidth, and thus, when no low-frequency vibrations arise, all data are filtered with the same bandwidth of 5 Hz, which provides the same delay of data pre-processing for the majority of the flight. This approach hence brings an added advantage to inertial data pre-processing and enhances the ACC-based attitude compensation possibilities.

The rest of the paper is organized as follows: Section 2 outlines the methodology of the proposed concept in detail. A detailed description of the principle of estimating the sensor's signal via a sinusoidal estimation filtering algorithm is also presented in this section. Section 3 provides the results of the proposed algorithm applied on simulated data and real flight data and confirms the suitability of the approach. Section 4 concludes the paper with final remarks.

2. Methodology

This paper proposes an adaptive variable bandwidth filtering via sinusoidal data estimation to pre-process the data of ACCs and ARSs by as narrow a bandwidth LP filter as possible, while preserving the dynamics information included in the data. In the past, several attempts were made to use variable bandwidth filtering in communications systems [12,13], but the use was limited to a fixed length of finite impulse response (FIR) filters. However, the length of the filter is always proportional to its delay, which restricts the usability for navigation purposes. In the proposed concept, two key assumptions are made:

1. The vibration content in the inertial data has an approximately periodic and sinusoidal characteristic.

2. The frequency of the signal content varies gradually, and the changes are smooth.

A schematic block diagram of the proposed signal filtering method using variable bandwidth filters is depicted in Figure 3.
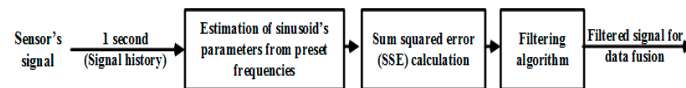

Figure 3. Complete filtering block diagram.

In general, the overall filtering process can be broken down into three main stages: (1) estimation of the sinusoid's parameter; (2) sum squared error calculation; and (3) applying filtering on the signal. The overall filtering task is carried out with a 1 s window of the signal history. This particular length of the history is chosen to have the capability to detect vibration content down to 0.5 Hz, since at least a half cycle of the approximate sinusoidal signal is necessary for the estimation process. The estimation of the sinusoid's frequency is based on preset frequencies, which are chosen according to the required filtering pass bands and bandwidths associated with the flight operational conditions. When raw signals enter the first block, they are fitted with sinusoids of all preset frequencies to get their approximations. The raw signals and their sinusoidal approximations are then led to the second block to calculate the sum squared error (SSE) of the fitting. The sinusoidal approximation with the preset frequency for which the SSE is the lowest marks the best fit and, thus, indicates the operating frequency of the vibration's strongest content. Finally, based on the operating frequency, a variable bandwidth in the filtering algorithm is adapted and applied on the signal. The process in the first and second block can be easily performed by fast Fourier transformation (FFT) while post-processing; however, it is computationally expensive for real-time applications. Thus, applying the proposed sinusoidal approximation technique brings an advantage in terms of lower computational demands, making the filtering suitable for real-time applications. Details about the chain of signal processing described above are presented in the following subsections.

2.1. Principles of Sinusoidal Signal Estimation

As mentioned earlier in Section 1, the vibration impact on the sensor's signal is often periodic, sinusoidal in nature and with one strongest frequency content. Therefore, it is often a reasonable approximation to address the problem of determining/estimating the frequency content in the raw signal via sinusoidal fitting algorithms.

Assume that the signal history x is obtained at time instances t where N is the total number of samples in the sequence. N is chosen to preserve a 1 s window. x_N and t_N correspond to the latest sample, and $(N - 1)$ down to 1 represent samples in the signal history.

$$x_n = [x_1 \, x_2 \ldots x_{N-1} \, x_N]^T; \; t_n = [t_1 \, t_2 \ldots t_{N-1} \, t_N] \tag{1}$$

For a small signal history window, the history sequence x can be assumed as periodic with a frequency f and angular frequency $\omega = 2\pi f$. The orthogonality relationships of the sine and cosine functions can be used to break down an arbitrary periodic function into a set of simple terms that can be summed, solved individually and then recombined to obtain the solution to the original signal sequence

25

x_n or to its approximation. Using the method for a generalized Fourier series, the signal history sequence x can be represented or modeled as a summation of the cosine and sine, as follows:

$$s_n(\vartheta) = A \cos(\omega \times t_n) + B \sin(\omega \times t_n) + C \tag{2}$$

where s_n is the approximation of x_n ; $A, B, C,$ ω and f are unknown constants, and ϑ defines the set of these four unknown parameters (A, B, C and ω). The sine wave fitting problem in (1) and (2) can be then solved by minimizing of the sum squared error [14,15], which is given by:

$$V(\vartheta) = \frac{1}{N} \sum_{n=1}^{N} (x_n - s_n(\vartheta))^2 \tag{3}$$

Consider the particular parameter vector θ; where $\theta = [A\ B\ C]^T$ and ϑ can be written as:

$$\vartheta = [\theta^T \ \omega]^T$$

Let $D\ (\omega)$ be the $N \times 3$ matrix defined as:

$$D\ (\omega) = \begin{bmatrix} \cos(\omega \times t_1) & \sin(\omega \times t_1) & 1 \\ \vdots & \vdots & \vdots \\ \cos(\omega \times t_N) & \sin(\omega \times t_N) & 1 \end{bmatrix} \tag{4}$$

The sum squared error in (4) can be written as:

$$V(\vartheta) = V(\omega, \theta) = \frac{1}{N} \{ [x_n - D\ (\omega)\theta]^T [(x_n - D(\omega)\theta)] \} \tag{5}$$

When the frequency f of the signal history is known (in other words, angular frequency ω is known), Equation (5) can be minimized in the least squares sense by solving the set of linear equations $D(\omega)\theta = x_n$ [16]. If $D(\omega)$ has the full rank, the solution of the estimated $\hat{\theta}$ is given by:

$$\hat{\theta} = \begin{pmatrix} \hat{A} \\ \hat{B} \\ \hat{C} \end{pmatrix} = \left(D(\omega)^T D(\omega) \right)^{-1} D(\omega)^T x_n \tag{6}$$

It can be noted that for large N, the columns in $D(\omega)$ become orthogonal. Thus, $D(\omega)^T D(\omega)$ becomes a diagonal matrix with elements $[{N}/{2}\ {N}/{2}\ N]$. Thus, it makes the calculation of the inverse of $(D(\omega)^T D(\omega))$ to estimate $\hat{\theta}$ computationally inexpensive.

2.2. Sum Squared Error Calculation to Estimate the Filtering Bandwidth

The principles described in Section 2.1 are used to estimate the frequency content in the signal considering the 1 s window of the signal history. The mentioned Equations (5) and (6) can be solved easily when the frequency f is known. Therefore, the proposed approach uses preset frequencies $\hat{f}_i$. These frequencies specify the filtering bandwidth, which can be then applied in the third block in Figure 3. Each $\hat{f}_i$ is used to estimate $D(\omega)$ defined in Equation (4) and $\hat{\theta}$ in Equation (6). The sinusoidal signal $\hat{x}_{i_i}$ is then constructed for each $\hat{f}_i$ and the corresponding $\hat{\theta}$ using:

$$\widehat{x_{n_i}} = \hat{A} \cos(2\pi \hat{f}_i \times t_n) + \hat{B} \sin(2\pi \hat{f}_i \times t_n) + \hat{C} \tag{7}$$

This step gives the advantage of using as many estimates as needed for the specific application and required filtering bandwidths. To get the best sinusoidal approximation with respect to the original raw signal x_n, the *SSE* is calculated using:

$$SSE = \sum_{1}^{N} \left(x_n - \widehat{x_{n_i}}\right)^2 \qquad (8)$$

The preset frequency $\hat{f}_i$, which gives the lowest value of the SSE, provides the best fit for the measured signal and, thus, indicates the operating frequency based on which the filtering bandwidth of the third stage is adapted and applied. Since the estimation process uses the 1 s window, the proposed approach has a corresponding learning time of 1 s. This means that the proposed approach will take 1 s to detect a complete change/transition in the frequency and to adapt the filtering bandwidth.

2.3. Filtering Algorithm

A conventional finite impulse response (FIR) filtering (such as generalized equiripple, quadratically weighted moving average, *etc.*) alone cannot be used for such a low filtering bandwidth (≈0.5 Hz) while providing smooth data. In addition, reaching such a narrow bandwidth would lead to higher order filters, which is not desirable, since they produce a long delay in the signal processing. Therefore, a novel multistage adaptive filtering approach is developed, as demonstrated in the block scheme in Figure 4. The proposed filtering process is adaptive in the sense that the bandwidth of the overall filtering process can vary with respect to the frequency content in the signal. The filtering process can be broken down into two main stages. The first stage is the filtering of the signal using a variable bandwidth Kaiser windowed filter with coefficients $[b_1\ b_2\ ..... b_{N-1}\ b_N]$, while the second stage utilizes an LP wavelet filter with a variable level of decomposition.
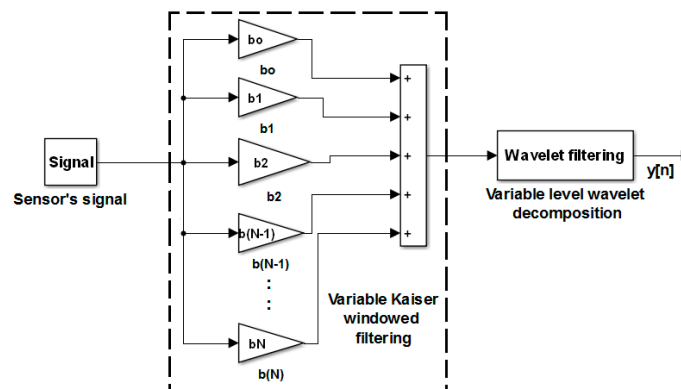

Figure 4. Schematic diagram of the new filtering algorithm.

For the first stage, a Kaiser windowed LP filter is chosen, since it allows to control the transition band, pass band and stop band ripples through a proper choice of the filter order and has further a unique *sin* function shape, which provides low bandwidth and low side lobes at an equivalent filter length

compared to other types of conventional filters. The coefficients of the Kaiser windowed LP filter can be calculated as:

$$b(n) = \frac{I_o(\frac{2\beta}{M}\left(\sqrt{n(M-1)}\right)}{I_o(\beta)} \tag{9}$$

where β is an arbitrary, non-negative real number that determines the shape of the window, I_o is the zeroth order modified Bessel function and M is the order of the filter.

The second stage is formed by a wavelet filter, which brings further advantages in terms of a further attenuation of high frequency noise, while preserving an acceptable delay. Different levels of wavelet decomposition can be reached by taking an LP mother wavelet filter, upsampled by a factor of 2 and convolving it with the same LP mother wavelet filter. This process can be repeated to achieve different levels of decomposition and, thus, different filtering bandwidths. In our case, the *sym*4 mother LP wavelet was considered. The details of the choice of mother wavelet filter and for obtaining different levels of decomposition are outlined in [17–20].

The filtering bandwidth of wavelet filtering cannot be explicitly chosen or controlled; however, wavelet filters are capable of providing smooth data for signal reconstruction. Whereas the filtering bandwidth for the Kaiser window can be chosen based on Equation (9), the two characteristics of the two filters can be combined together to provide one overall filter that is efficient in low frequency attenuation, while keeping the filter order minimal; in other words, keeping the delay minimal.

In the filtering process, the raw signal is passed through the Kaiser windowed LP filter and then filtered by the wavelet filter to further suppress the high frequency noise and to smooth the filtered signal. Note that the overall filtering bandwidth can be modified by varying the length of the Kaiser windowed LP filter and by modifying the level of the wavelet filter decomposition. Simulation results are discussed in detail in Section 3.2, and the experimental verification is in Section 3.4.

3. Performance Evaluation and Discussion

The performance of the proposed filtering approach is evaluated based on simulated data, as well as on real flight data. The algorithm was implemented using MATLAB. The results are presented in detail in the following subsections.

3.1. Performance of the Filtering Algorithm with Different Bandwidths

As mentioned above, a main objective of the proposed filtering algorithm is to achieve efficient filtering performance in terms of low frequency vibration attenuation in the signal while preserving an acceptable delay. For this reason, we have split the frequency range of interest, 0.5 to 5.5 Hz, into 11 bandwidths with a step size of 0.5 Hz. Based on the required bandwidth values, we have optimized the coefficients of the Kaiser windowed LP filter using Equation (9) and chose the levels of wavelet filter decomposition.

To observe the efficiency of the overall filtering, we simulated a sinusoidal signal with frequencies in the range of 0.5 to 14 Hz and let it pass through both stages of the proposed filtering algorithm. The sampling frequency of the simulated signals was chosen to be 43 Hz to be consistent with the sampling frequency of the real flight experiment. The performance of the filtering for two signal frequencies

28

(0.5 Hz and 1 Hz) when the bandwidth was set to 0.5 Hz is depicted in Figure 5. For all combinations of the bandwidths and the signal frequencies, see Table 1, which summarizes the filtering performance. Particular delays corresponding to the filtering performances are denoted in Table 2. It can be seen that the maximum delay in the signal is about 0.39 s, which is an acceptable delay for ACC signal processing and attitude compensation.
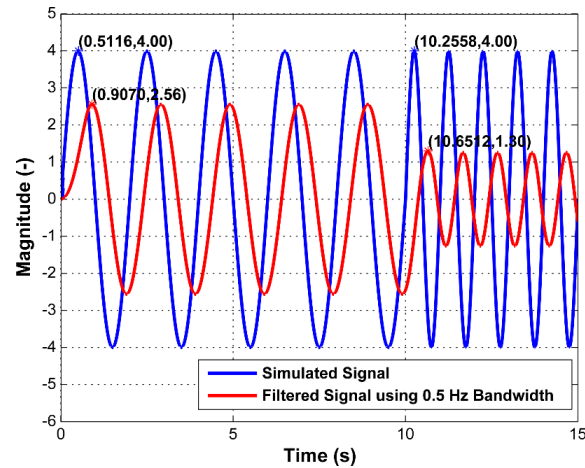
Figure 5. Filtering the simulated signal using only the 0.5 Hz bandwidth filter.

The attenuation level in the filtered signal is calculated using:

$$G_{dB} = 20 \log_{10}(A_2/A_1) \tag{10}$$

where A_1 is the amplitude of the original signal and A_2 is the amplitude of the filtered signal.

The selection of the filtering bandwidth that is applied in the third block in Figure 4 is dependent on Tables 1 and 2. In Table 1, the minimum required level of attenuation corresponds to −15 dB; nevertheless, if further attenuation is needed, it is always a possibility to use a narrower bandwidth up to 0.5 Hz. Attenuation of −15 dB corresponds to approximately 1/5th of the original amplitude. The particular choice of filtering bandwidth based on the signal operating frequency is highlighted in dark grey in Table 1. For example, if the operating signal frequency is 10 Hz or higher, the filtering bandwidth is 5.5 Hz. If it is from 8 to 10 Hz, the filtering bandwidth is going to be 5 Hz.

Table 1. Filtering efficiency at different filtering bandwidths for various signal frequencies.

		Signal Frequency (Hz)															
		14	12	10	8.0	6.0	5.0	4.5	4.0	3.5	3.0	2.5	2.0	1.5	1.0	0.6	0.5
Filtering Bandwidth (Hz)	**5.5 (M = 24, L = 1)**	−34.5	−31.5	−22.3	−9.0	−6.0	−0.5	0.1	0.3	0.0	−0.1	−0.3	−0.2	−0.1	−0.1	0.1	0.1
	5.0 (M = 28, L = 1)	−45.7	−35.2	−29.9	−24.1	−8.9	−3.7	−0.5	0.5	0.4	0.0	−0.1	−0.2	0.0	−0.1	0.0	0.0
	4.5 (M = 30, L = 1)	−42.7	−38.3	−32.6	−31.0	−28.7	−6.2	−2.5	−0.6	0.0	0.1	0.0	−0.4	−0.4	−0.3	0.0	0.0
	4.0 (M = 26, L2)	−42.6	−38.6	−33.7	−28.8	−24.1	−16.1	−7.4	−3.4	−0.6	0.0	0.1	0.0	−0.3	−0.4	−0.1	0.0
	3.5 (M = 29, L2)	−36.7	−35.0	−32.8	−30.1	−23.4	−22.5	−15.4	−7.7	−3.7	−0.9	0.5	0.5	0.5	0.5	0.1	0.1
	3.0 (M = 32, L = 1)	−53.7	−40.8	−40.8	−36.5	−29.1	−26.1	−24.9	−26.6	−9.4	−3.7	−0.3	0.5	0.3	0.1	−0.1	0.0
	2.5 (M = 28, L = 2)	−45.6	−44.7	−42.3	−37.5	−29.8	−31.1	−22.8	−23.0	−21.2	−12.8	−6.0	−1.2	−0.1	0.7	0.4	0.0
	2.0 (M = 32, L2)	−41.5	−38.3	−43.0	−33.8	−37.3	−29.2	−36.3	−25.9	−28.0	−19.3	−9.4	−3.6	−0.6	0.0	0.1	0.1
	1.5 (M = 7, L = 3)	−40.7	−40.1	−45.6	−29.9	−41.4	−37.5	−35.5	−34.5	−21.4	−12.7	−17.1	−4.2	−2.5	−0.9	0.0	0.0
	1.0 (M = 38, L = 1)	−62.7	−62.5	−61.6	−59.4	−57.5	−56.4	−58.2	−56.4	−59.4	−43.3	−26.2	−15.3	−8.2	−3.6	−0.5	0.0
	0.5 (M = 33, L = 3)	−39.2	−40.1	−38.8	−38.5	−40.0	−40.1	−29.4	−37.8	−27.3	−37.6	−24.1	−35.3	−20.5	−9.8	−4.5	−3.9

Note: M corresponds to the Kaiser windowed filter order, and L corresponds to the level of wavelet decomposition (LoD).

Table 2. Time delays for the chosen filtering bandwidths.

Filtering Bandwidth (Hz)	Time Delay (s)
5.5	0.23
5.0	0.24
4.5	0.26
4.0	0.33
3.5	0.35
3.0	0.36
2.5	0.37
2.0	0.38
1.5	0.38
1.0	0.39
0.5	0.39

3.2. Demonstration of Data Smoothing

As mentioned in Section 2.3, the wavelet filters are used to smooth the signal, as well as to further attenuate its unwanted high frequency content. To confirm these characteristics, a white noise was generated with variance set to unity. Two LP Kaiser filters were designed for the bandwidth of 2 Hz with different filter orders (M = 25 and M = 32) using Equation (10) and applied to the white noise. Afterwards, the signal filtered with the Kaiser filter of M = 25 was further passed through the wavelet filter with level of decomposition (LoD) = 1. The filtering results are shown in Figure 6. The results are further demonstrated in the frequency domain in Figure 7.
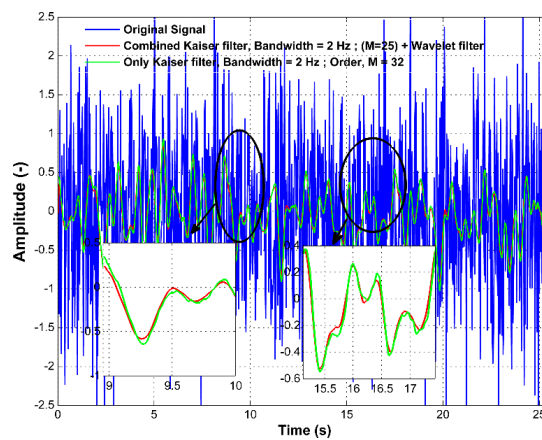

Figure 6. Comparison between filtering using only the Kaiser windowed low-pass (LP) filter and the proposed filtering multistage algorithm with the wavelet filter implemented in the time domain.
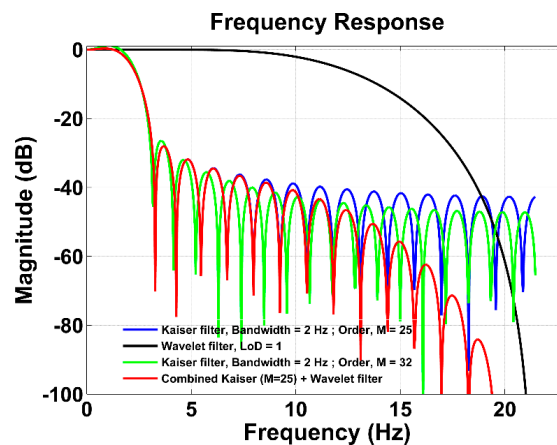

Figure 7. Comparison between filtering using only the Kaiser windowed LP filter and the proposed filtering multistage algorithm with the wavelet filter implemented in the frequency domain.

In Figure 7, it can be seen that both LP Kaiser filters with a cut-off frequency of 2 Hz have slightly different attenuation at higher frequencies; however, their delays are different, *i.e.*, 0.28 s and 0.36 s. Nevertheless, when the LP Kaiser filter of M = 25 (blue line) is combined with the wavelet filter with the first level of decomposition (LoD = 1) (black line), which has M = 7, the combined filter performance (red line) changes for the higher frequencies, while preserving the attenuation at low frequencies. The overall filtering has the order M = 32, and its filtering efficiency increases when attenuating higher frequencies. Thus, it reaches better performance than using only the LP Kaiser filter of M = 32 with a comparable time delay. This means that the proposed filtering approach provides a more enhanced filtering capability compared to conventional filters, while keeping the filter order at a minimum.

This can be explained by the wavelet filters being advantageous despite having an irregular shape to their frequency characteristics. They are able to perfectly reconstruct functions with linear and higher order polynomial shapes, such as rectangular, triangular, second order polynomials and windowed filters [21]. Note that Fourier series fail to do so while designing regular filters, such as Kaiser, and various other conventional filters mentioned earlier [22]. As a result, wavelets are able to denoise the particular signals better than conventional filters that are based on the Fourier transform design and that do not follow the algebraic rules obeyed by the wavelets.

3.3. Application of the Multistage Filtering Algorithm on Simulated Data

For testing the adaptability of the proposed filtering approach, a sinusoidal signal was simulated with two frequencies (2 Hz and 3 Hz) with additive white Gaussian noise of unity variance and a sampling frequency of 43 Hz. It was observed how the filter behaves with respect to a change of frequency. The resulting performance is shown in Figure 8.
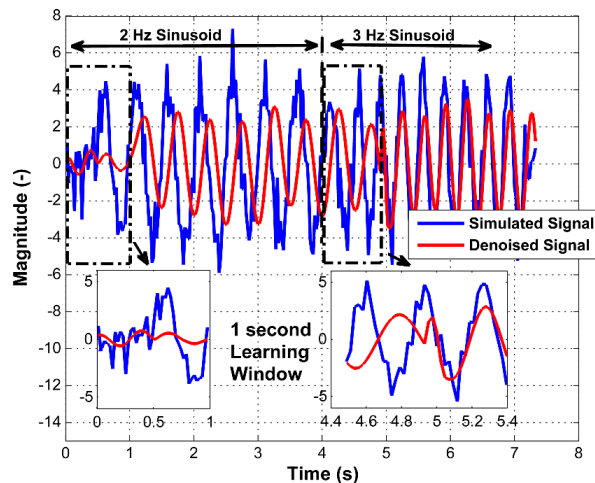

Figure 8. Filtering result on the simulated signal.

The first part of Figure 8 contains the signal with 2 Hz, while 3 Hz is used in the second part. From the filtered data, it can be seen that the filtering method has a 1 s learning time to observe the complete transition between one operating frequency to another. The figure also illustrates that for a low

frequency (2 Hz), a lower filtering bandwidth is used than in the case of a frequency of 3 Hz. The zoomed part of the time range of 4.4 to 5.4 s shows the filter behavior when the filtering bandwidth is changed.

3.4. Application of the Algorithm on Real Flight Data

As mentioned in Section 1, a narrow bandwidth filtering is required due to the potential presence of low frequency vibrations affecting inertial sensors. Aircraft can fly under direct and un-accelerated conditions or under dynamic motion conditions. For cost-effective attitude estimation systems, it is necessary to consider that the signals from the ARSs require preserving the dynamics information, and in contrast, the ACCs' signals are used as an aiding source to compensate for the attitude estimation, only under steady flight conditions. Mentioned in Section 1, the motion dynamics of light aircraft lies within the 5 Hz bandwidth; hence, a constant bandwidth of 5.5 Hz is used for the ARSs' signal filtering. This choice provides unmodified dynamics in the range of 5 Hz, as required. In the case of ACC signals, an adaptive bandwidth filtering is applied to reduce the vibration effects in the signals. In other words, the same bandwidth of 5.5 Hz is chosen for both ARSs and ACCs when the flight conditions lead to noise and vibrations with frequencies higher than 10 Hz. This ensures the same delay for both ARSs and ACCs for the majority of the flight, which is advantageous. When conditions change and the vibration frequency goes down, the ACCs' signal filtering bandwidth is adapted accordingly, potentially down to 0.5 Hz, while the filtering bandwidth for the ARSs' signals does not change. This approach provides both observable dynamics from ARSs and a compensation capability for attitude estimation with the help of the ACCs, even under steady flight conditions when the ACCs are affected by low frequency vibrations. Generally, due to the low frequency vibrations' influence, the operation of the majority of the commercially used cost-effective AHRSs is limited. In contrast, the proposed filtering approach is more robust while operating under a low frequency vibrating environment compared to the commonly used approaches.
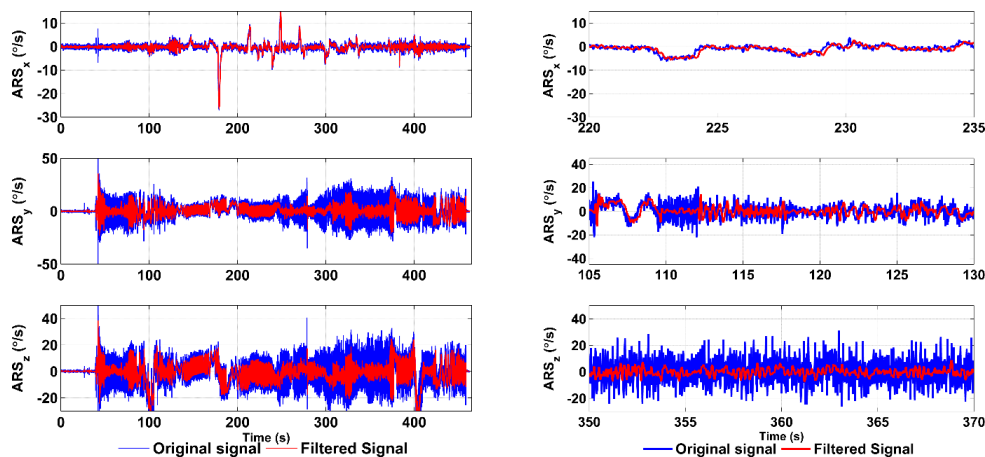

Figure 9. Angular rates measured during the flight, the filtered signals and the zoomed tracks.

33

Real flight data for ACCs and ARSs are obtained from flight experiments using the ultra-light aircraft, ATEC 321. The flight data were sampled at a frequency of 43 Hz. As proposed, for the filtering purposes, 11 different bandwidths were chosen at equal intervals from 0.5 Hz to 5.5 Hz. The filtering of the ARS data using a constant 5.5-Hz bandwidth LP filter is shown in Figure 9. It can be seen that the potential high frequency noise is attenuated and filtered in the ARS measurements, while preserving the delay up to 0.23 s.

Figure 10 shows the ACC signal from the same flight as shown in Figure 9.
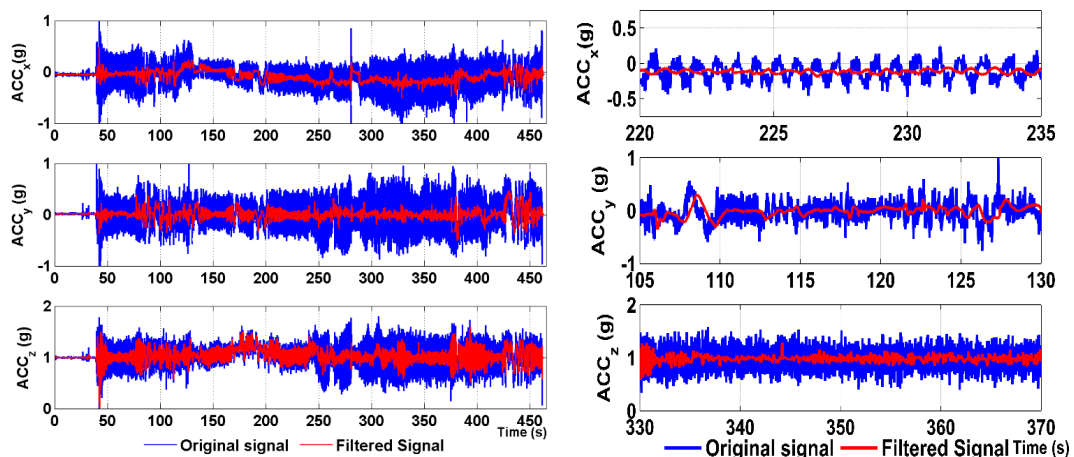
Figure 10. Acceleration measured during engine suppression, the filtered signal and the zoomed tracks.

It can be seen in Figure 10 that the low frequency vibrations affecting the signal during the engine suppression between 220–235 s are significantly attenuated in the case of ACC_x (zoomed tracks). This measured signal suffered from a vibration frequency of about 0.5 Hz, and thus, at this point, the filtering was performed at the lowest bandwidth corresponding to the highest filtering order. On the other hand, the ACC_y track in the range of 105–130 s suffered from high frequency vibrations; hence, the filtering was performed with a wider bandwidth; so, the filtering order was lower and the delay was shorter.

To confirm the adaptability of the filtering bandwidth, the ACC_x signal is shown in Figure 11 with zoomed parts. It demonstrates the variable bandwidth filtering capability and corresponding delays. In the left inset, the signal frequency was approximately 1.25 Hz and the filtering bandwidth was set to 0.5 Hz, which corresponds to the narrowest filtering bandwidth and which operates at the highest level of wavelet decomposition, *i.e.*, LoD = 3. At this instance, the order of the filter is maximal and the time delay corresponds to 0.39 s. In comparison, in the right inset, it can be seen that the signal frequency content is approximately 4 Hz and the filtering bandwidth corresponds to 3 Hz. In this instance, the time delay is 0.36 s, because the order of the filter is lower. In addition, it can be seen that a better attenuation is achieved, while the signal frequency is higher.

34

Figure 11. Variable bandwidth filtering of ACC in the x-axis.

Nevertheless, the variable filtering of ACC signals is applied only when the character of the signal content is periodic; otherwise, a constant 5.5-Hz bandwidth filter is applied the same way as used in the ARS's signals. This approach provides the same delay on both ARS and ACC data during the majority of the flight, and when low frequency vibration content occurs in ACC data, which is generally under special and rare conditions, such as the engine RPM suppression, the bandwidth of ACC data filtering is modified. This 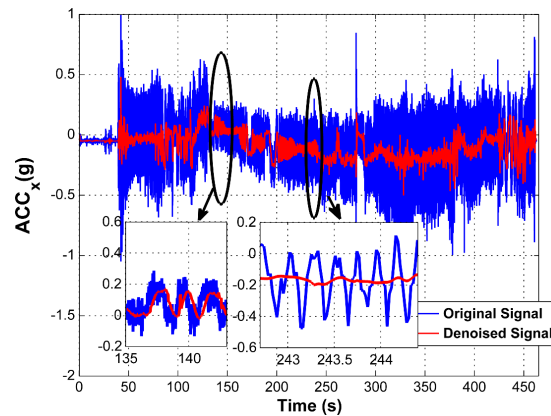case leads to different delays for the ARS and ACC data; however, as long as they are used only for attitude compensation under steady-state conditions, these differences can be simply managed by taking different delays in data fusion into account.

4. Conclusions

This paper proposed a novel concept of filtering inertial data with an enhanced capability of providing smooth data under harsh environments, eliminating low frequency vibration influences. Cost-effective attitude and heading reference systems (AHRSs) generally fuse data from angular rate sensors (ARSs) and accelerometers (ACCs) to provide stable attitude estimation. Commonly, it is advantageous to fuse data in such a way that very low-frequency content corresponding to the steady-state flight conditions is taken from the ACC's measurements and higher-frequency content corresponding to changes of flight conditions is obtained from the ARS's measurements. Nevertheless, a problem arises when ACC readings are affected by low-frequency vibrations, and thus, the compensation ability in the attitude estimation process becomes vibration dependent. This is often the case when the correct filtering is not applied on the ACC's signals. The contribution of this paper thus lies in proposing the filtering of the ACC's with an adaptive bandwidth capability, providing the same delay in inertial data processing, when vibration frequencies are above 10 Hz. When the vibration frequency in the ACC's data is below 10 Hz, the data are filtered with a modified bandwidth to reduce the vibration effects. The modification of the filtering bandwidth relies on continuous estimation of the frequency of the strongest vibration content based on the particular bandwidth filtering applied. This filtering approach was confirmed based on simulated and real-flight data, and in all cases, the proposed approach reached better efficiency for vibration impact reduction, while preserving shorter processing delays compared with the commonly used approaches used in the commercially available AHRS

systems. This paper presents the data pre-processing in terms of data filtering and not data fusion. Nevertheless, based on the effectiveness of vibration impact reduction, the proposed approach improves the ACC-based attitude compensation capability even under strong vibration, which brings a significant advantage compared with the commercially available systems.

Acknowledgment

Author Contributions

The presented work contains equal contribution from the all the authors. J. Rohac defined the research theme and was responsible for the overall guidance and results analysis. M. Alam was responsible for the conceptualization of the proposed methods, filtering algorithms including the mathematical modeling.

Conflicts of Interest

The authors declare no conflict of interest.

References

1. Gebre-Egziabher, D.; Hayward, R.C.; Powell, J.D. A low-cost GPS/inertial attitude heading reference system (AHRS) for general aviation applications. In Proceedings of the IEEE 1998 Position Location and Navigation Symposium, Palm Springs, CA, USA, 20–23 April 1998.
2. Savage, P.G. Strapdown inertial navigation integration algorithm design part 1: Attitude algorithms. *J. Guid. Control Dyn.* **1998**, *21*, 19–28.
3. Savage, P.G. Strapdown inertial navigation integration algorithm design part 2: Velocity and position algorithms. *J. Guid. Control Dyn.* **1998**, *21*, 208–221.
4. Sipos, M.; Paces, P.; Reinstein, M.; Rohac, J. Flight attitude track reconstruction using two AHRS units under laboratory conditions. In Proceedings of the 2009 IEEE Sensors, Christchurch, New Zealand, 25–28 October 2009.
5. Euston, M.; Coote, P.; Mahony, R.; Jonghyuk, K. A complementary filter for attitude estimation of a fixed-wing UAV. In Proceedings of the International Conference on Intelligent Robots and Systems, Nice, France, 22–26 September 2008.
6. Bristeau, P.-J.; Petit, N. Navigation System for Ground Vehicles using Temporally. In Proceedings of the American Control Conference, O'Farrell Street, San Francisco, CA, USA, 29 June–1 July 2011.
7. Reinstein, M.; Kubelka, V. Complementary filtering approach to orientation estimation using inertial sensors only. In Proceedings of the IEEE International Conference on Robotics and Automation (ICRA), Prague, Czech Republic, 14–18 May 2012.

8. Farrell, J. Aided Navigation: GPS with High Rate Sensors; McGraw Hill Education: New York, NY, USA, 2008.

9. Simanek, J.; Reinstein, M.; Kubelka, V. Evaluation of the EKF-Based Estimation Architectures for Data Fusion in Mobile Robots. *IEEE-Asme T. Mech.* **2014**, *20*, 985–990.

10. Moorhouse, D.J.; Woodcock, R.J. Background Information and User Guide for MIL-F-8785C, Military Specification-Flying Qualities of Piloted Airplanes. Air Force Wright Aeronautical Labs Wright-Patterson Air Force Base: Dayton, OH, USA, 1982.

11. Pratt, R.W. Flight Control Systems: Practical Issues in Design and Implementation, The Institute of Electrical Engineers: Stevenage, UK, 2000; pp. 119–167.

12. Harris, F. Fixed length FIR filters with continuously variable bandwidth. In Proceedings of the 1st International Conference on Wireless Communication, Vehicular Technology, Information Theory and Aerospace & Electronic Systems Technology. Aalborg, Denmark, 17–20 May 2009.

13. Harris , F.; Lowdermilk, W. Implementation Considerations and Performance Comparison of Variable Bandwidth FIR Filter and Phase Equalized IIR Filter. In Proceedings of the Conference Record of the Forty-First Asilomar Conference on Signals, Systems and Computers, Pacific Grove, CA, USA, 4–7 November 2007.

14. IEEE Standard for Digitizing Waveform Recorders, 1994; pp. 1–74. Available online: http://ieeexplore.ieee.org/stamp/stamp.jsp?arnumber=469117 (accessed on 30 January 2015)

15. IEEE Standard for Terminology and Test. Methods for Analog-To-Digital Converters, 2001; pp. 1–92. Available online: http://ieeexplore.ieee.org/stamp/stamp.jsp?arnumber=929859 (accessed on 30 January 2015)

16. Kay, S.M. Detection Theory. In *Fundamentals of statistical signal processing*; Prentice Hall: Upper Saddle River, NJ, USA, 1998; Volume 2.

17. Rohac, J.; Reinstein, M.; Draxler, K. Data processing of inertial sensors in strong-vibration environment. In Proceedings of the 2011 IEEE 6th International Conference on Intelligent Data Acquisition and Advanced Computing Systems (IDAACS), Prague, Czech Republic, 15–17 September 2011.

18. Rohac, J.; Daado, S. Impact of Environmental Vibration on Inertial Sensor's Output. *Sens. Transducers J.* **2013**, *24*, 19–27.

19. Fugal, D.L. Conceptual Wavelets In Digital Signal Processing; Space & Signals Technologies LLC: Berlin, Germany, 2009.

20. Rajmic, P.; Vlach, J.; Vyoral, J. Real-time wavelet transform with overlap of signal segments. In Proceedings of the International Conference on Signals and Electronic Systems, Krakow, Poland, 14–17 September 2008.

21. Weeks, M. Digital Signal Processing Using MATLAB & Wavelets; Jones & Bartlett Learning: Sudbury, MA , USA, 2010.

22. Wojtaszczyk, P. A Mathematical Introduction to Wavelets; Cambridge University Press: Cambridge, UK, 1997.

Chapter 5

Navigation Data Estimation using Nonlinear Estimation Algorithms

5.1 Summary of the contributions

This chapter outlines on the navigation data estimation technique using INS aided by GNSS measurement. Various techniques for fusing the INS and GNSS data to get as accurate estimation as possible is discussed in details. The main contribution of this chapter lies in providing a detailed performance analysis of loosely coupled navigation solutions, where a nonlinear observer and two EKF solutions with different architectures/models incorporated are in focus. Two different architecture of EKFs are discussed, one with a 21-state single-stage and the other with a multi-stage configuration. For both the EKF architectures, loosely couples GNSS integration schemes are used. The single-stage EKF provides the strongest connection between the final attitude estimation and GNSS based position and velocity measurements. The estimation process in multi-stage EKF architecture is divided into two main parts; an Attitude estimator and a Position/Velocity estimator. By using cascaded Kalman filtering, this method avoids the need to propagate additional states, resulting in the covariance propagation to become more computationally efficient. The estimation results are verified on real flight data tested on Slingsby T67C aircraft. The accuracy of the estimation techniques were thoroughly studied during GNSS outages.

5.2 Publication

The work is represented by a publication with modified formatting and follows on the next page.

Full Length Article

Validation of nonlinear integrated navigation solutions

CrossMark

Jan Rohac[a,*], Jakob M. Hansen[b], Mushfiqul Alam[a], Martin Sipos[a], Tor A. Johansen[b], Thor I. Fossen[b]

[a] Department of Measurement, Faculty of Electrical Engineering, Czech Technical University in Prague, Prague, Czech Republic
[b] Department of Engineering Cybernetics, Norwegian University of Science and Technology, Trondheim, Norway

A B S T R A C T

There exist numerous navigation solutions already implemented into various navigation systems. Depending on the vehicle in which the navigation system is used, it can be distinguished in most cases among; navigation, tactical, and commercial grade categories of such systems. The core of these systems is formed by inertial sensors, i.e. accelerometers and angular rate sensors/gyros. Navigation and tactical grade systems commonly rely on fiber optic/ring laser gyros and servo/quartz accelerometers with high resolution, sensitivity, and stability. In the case of cost-effective navigation systems, for example piloted light and ultralight aircraft, usually use commercial grade sensors, where the situation differs. The sensor outputs are less stable and sensitive, and suffer from manufacturing limits leading to temperature dependency, bias instability, and misalignment which introduces non-negligible disturbances. These conditions commonly limit the applicability of the navigation solution since its stand-alone operation using free integration of accelerations and angular rates is not stable. This paper addresses a cost-effective solution with commercial grade inertial sensors, and studies the performance of different approaches to obtain navigation solution with robustness to GNSS outages. A main goal of this paper is thus comparison of a nonlinear observer and two extended Kalman filter solutions with respect to the accuracy of estimated quantities and their sensitivity to GNSS outages. The performance analyses are carried out on real flight data and evaluated during phases of the flight when the solutions are challenged by different environmental disturbances.

© 2017 Elsevier Ltd. All rights reserved.

1. Introduction

Cost-effective MEMS (Micro-Electro-Mechanical System) based inertial measurement units (IMU) aided with GNSS (Global Navigation Satellite System) based positioning have become common for applications in broad areas of interest, such as piloted light and ultralight aircraft, unmanned aerial, terrestrial, and water vehicles. For a strapdown navigation solution an inertial navigation system (INS) consisting of tri-axial accelerometer (ACC) and tri-axial angular rate sensor (ARS) aided with GNSS receiver is used for position, velocity and attitude (PVA) estimation. There are various methods for INS aiding with using GNSS based measurements based on un-coupled (Savage, 1998a,b), loosely coupled (Wolf, Eissfeller, & Hein, 1997), tightly coupled (Li, Wang, Rizos, Mumford, & Ding, 2006), and ultra-tightly coupled (Babu & Wang, 2009) integration schemes. A variety of the mentioned integration schemes integrates IMU measurements with GNSS based ones in order to provide a stable and robust navigation solution regardless of the con-

dition of operation. MEMS based IMUs are compact, lightweight, and cost-effective thus offering a cheap solution. However, at the same time they suffer from bias instability, insufficient sensitivity, noise etc. That presents significant challenges in data processing which has to be dealt with in the data fusion process. Moreover, the vibration imposed by vehicle or engine motions often dominates and corrupts ACC measurements (Alam & Rohac, 2015) as well as ARS readings depending on g- and g^2-sensitivity parameters. On the other hand, accuracy of the single point GNSS based measurements can degrade due to ionospheric or tropospheric refraction, multipath, and/or weak/blocked GNSS signal. However, by fusing available data these disadvantages of both individual systems can be reduced, and thereby the resultant system can provide a robust navigation solution under all environmental conditions even when GNSS signal is temporally unavailable or it suffers from increased level of error. The accuracy of the GNSS based measurements can be further improved with satellite-based augmentation system (SBAS) corrections and/or Real-Time-Kinematic (RTK) solutions down to the order of cm-level precision.

There are several approaches for fusing INS/GNSS in order to obtain PVA estimates, such as temporally interconnected ob-

Nomenclature

EKF	Extended Kalman Filter
NO	Nonlinear Observer
GNSS	Global Navigation Satellite System
ACC	Accelerometer
GYR	Gyroscope/angular rate sensor
BF	Body frame (b – frame)
NED	North-East-Down referential coordinate frame (n – frame)
ECEF	Earth-Centered-Earth-Fixed coordinate frame (e – frame)
ECI	Earth-Centered-Inertial coordinate frame (i – frame)
PVA	Position, Velocity, and Attitude
LP filter	Low-Pass filter
RMSE	Root Mean Square Error
TMO	Translational Motion Observer
C_b^n	Transformation matrix from the BF to NED
f^b	Vector of specific force expressed in the BF
ω_{ib}^b	Vector of angular rate between the BF and ECI expressed in the BF
a^b, v^b	Vectors of acceleration and velocity expressed in BF,
g^n	Vector of gravitational acceleration expressed in NED,
ACF	Vector of anti-centrifugal force,
Θ	Vector of Euler angles - (ϕ, θ, ψ),
p_{GNSS}^n, v_{GNSS}^n	Vectors of position and velocity from GNSS expressed in NED,
b_g, b_a	GYR and ACC bias vectors in BF,
$\hat{x}_k$	State vector estimate at a time instance k,
z, $\hat{z}_k$	Measurement vector, expected measurement vector formed based on $\hat{x}_k$,
T	Sampling period,
$\| \cdot \|_2$	Euclidean norm of the vector,
$(\cdot \times)$	Skew-symmetric matrix of the vector.

servers (Bristeau & Petit, 2011), complementary filters (Reinstein & Kubelka, 2012) or Kalman filters (KF) with various architectures (Alam, Moreno, Sipos, & Rohac, 2016; Farrell, 2008; Rezaeian et al., 2013; Simanek, Reinstein, & Kubelka, 2014; Simon, 2010; Zihajehzadeh, Loh, Lee, Hoskinson, & Park, 2015), eXogenous Kalman Filters, nonlinear observers (Johansen & Fossen, 2016), unscented Kalman filters (UKF) (Gustafsson et al., 2002; Ristic, Arulampalam, & Gordon, 2004) and particle filters (PF) (Sotak, Sopata, & Kmec, 2006). Due to the dynamic motion of the majority of the vehicles being highly nonlinear, the most commonly used approaches utilize nonlinear observers and extended Kalman filter (EKF). Much attention is also paid to UKF and PF, but their applicability is limited by high computational loads. In the following sections only EKFs and nonlinear observers are studied for the estimation algorithm and compared, where each approach has its own advantages.

The KFs generally provide estimates as well as the estimated uncertainty of the state vector based on a recursive algorithm (Bar-Shalom, Li, & Kirubarajan, 2004). It is a well-established state estimation approach for a linear or nonlinear state space model which works on the assumption that the inputs are normally-distributed and characterized by their mean and covariance values. The weakest point of the KF (and EKF) is calculation of the inverse covariance matrix of the measurement vector due to round-off errors when implemented into microcontrollers and its high computational cost. There are several methods to solve this problem for instance Modified Cholesky factorization (UD decomposition)
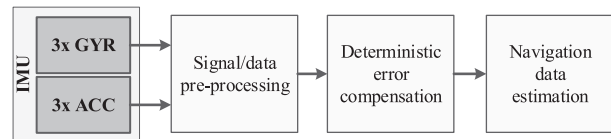

Fig. 1. Block scheme of processes required for position, velocity, and attitude estimation.

or sequential approaches, for more details see (Grewal & Andrews, 2001). Nonlinear observers are based on a deterministic approach, contrary to the stochastic approach of the KF, motivated by the higher computational load of KFs when applied to nonlinear systems. When designing nonlinear observers, the stability properties should be determined explicitly, whereas the optimality of the KF ensures stability in linear systems, while having no stability guarantee for nonlinear systems. In recent years, nonlinear observers have been proposed in various fields, where attitude estimation has had extensive research; for instance, see (Batista, Silvestre, & Oliveira, 2011a; Batista, Silvestre, & Oliveira, 2011b; Crassidis, Markley, & Cheng, 2007; Grip, Fossen, Johansen, & Saberi, 2012; Hamel & Mahony, 2006; Mahony, Hamel, Trumpf, & Lageman, 2009; Salcudean, 1991; Thienel & Sanner, 2003; Vik & Fossen, 2001). A common approach to determine attitude is to compare corresponding vectors in two coordinate frames, e.g. (Salcudean, 1991). These vectors can be based on e.g. gyroscopic data, (Vik & Fossen, 2001), magnetometer or velocity measurements, (Hamel & Mahony, 2006). A modular observer structure consisting of an attitude observer and translational motion observer was proposed in Grip, Fossen, Johansen, and Saberi (2013). Here the advantage is that the observer gains can be fixed or slowly time-varying leading to a decrease in computational load, compared to the KF gain estimation which is carried out at every iteration.

A main contribution of this paper lies in a providing a detailed performance analysis of loosely coupled navigation solutions, where a nonlinear observer and two EKF solutions with different architectures/models incorporated are in focus. For the EKFs two different architectures are presented, one with a 21-state single-stage and the other with a multi-stage configuration. The estimation algorithms are verified on real flight data from a Slingsby T67C aircraft, detailed in Section 4. This paper thoroughly investigates the robustness of the individual estimation approaches with respect to GNSS outages.

The paper is organized as follows: Section 2 outlines the estimation approaches used in the paper to estimate PVA. Section 3 presents a complete description of a sensor assembly and related description for flight experiments. Section 4 presents experimental verification, robust performance analysis and comparison of each estimation techniques with respect to GNSS outages when compared to the referential positioning system using RTK based GNSS positioning. Section 5 concludes the paper with final remarks.

2. Principles and models used

Navigation systems are primarily supposed to provide PVA estimates. The navigation data are typically estimated by a chain of processes schematically shown in Fig. 1.

Signal/data preprocessing can differ according to vehicle dynamics and types of sensors utilized. The sensors might have analog as well as digital outputs. In the case of analog outputs, the preprocessing requires A/D conversion. The LP filter is then used for both high-frequency components reduction and as an anti-aliasing filter. When the outputs are in digital form then a digital LP filter is utilized only. It is very important to choose the cut-

off frequency correctly and additionally observe the group delay. Usually, the sensor's bandwidth is about 300 Hz up to 800 Hz depending on the sensor's type. If high rate navigation solution is required, which is generally intended for airborne applications, the frequency bandwidth can be reduced down to 50 or 40 Hz. In some applications it can go even lower down to 20 or 10 Hz, but it is not a common case. Deterministic error's compensation is a further key process minimizing effects of non-orthogonality of sensing axes, sensor scale factors, temperature dependencies as well as misalignment of sensor frame mounted into vehicle body frame. Most of these deterministic error corrections can be done during in-flight/motion calibration procedures; however, the most common way is to calibrate sensor errors separately, see (Alam, Sipos, Rohac, & Simanek, 2015; Rohac, Sipos, & Simanek, 2015).

Navigation data generally consists of position, velocity, and attitude. These quantities are evaluated via dead-reckoning principles according to (1)–(4). The process is well known as mechanization of strapdown navigation equations. More details can be found in (Salychev, 2004; Savage, 1998a,b; Titterton & Weston, 2004).

$$\dot{\boldsymbol{v}}^n = \boldsymbol{C}_b^n \boldsymbol{f}^b + \boldsymbol{g}^n - \left(2\boldsymbol{\omega}_{ie}^n + \boldsymbol{\omega}_{en}^n\right) \times \boldsymbol{v}^n, \tag{1}$$

$$\dot{\boldsymbol{C}}_n^e = \boldsymbol{C}_n^e (\boldsymbol{\omega}_{en}^n \times), \tag{2}$$

$$\dot{p}_{Up}^n = -v_{Down}^n, \tag{3}$$

$$\dot{\boldsymbol{C}}_b^n = \boldsymbol{C}_b^n (\boldsymbol{\omega}_{ib}^b \times) - (\boldsymbol{\omega}_{in}^n \times) \boldsymbol{C}_b^n, \tag{4}$$

where low-letter indices indicate the quantity frame or frames relation (*en* – NED with respect to ECEF, *ie* - ECEF with respect to ICI, *ib* – BF with respect to ECI), or the axis within the frame, upper indices define in which frame the vector is expressed, $\boldsymbol{\omega}_{in}^n = \boldsymbol{\omega}_{ie}^n + \boldsymbol{\omega}_{en}^n$.

In the case of cost-effective solutions (1)–(4) can be reduced due to limited sensor's sensitivity into form

$$\dot{\boldsymbol{v}}^n = \boldsymbol{C}_b^n \boldsymbol{f}^b + \boldsymbol{g}^n, \tag{5}$$

$$\dot{p}_{Up}^n = -v_{Down}^n, \tag{6}$$

$$\dot{\boldsymbol{C}}_b^n = \boldsymbol{C}_b^n (\boldsymbol{\omega}_{ib}^b \times). \tag{7}$$

This INS mechanization has been known for a long time and has been verified in many applications (Simon, 2010). However, it still works with just raw inertial data passed through a LP filter and extracted from deterministic sensor's errors. To further improve the performance, accuracy, and robustness of the navigation solution data fusion is commonly used to combine inertial data with aiding systems. These aiding systems can vary based on a particular application having a different form and the integration can use different schemes. In this paper two different approaches are discussed and compared, i.e. extended Kalman filter in its single and dual structure and nonlinear observer. Data fusion helps estimate sensor's bias which is crucial in phases when aiding systems cannot be used. In addition to dealing with sensor errors and bias, applied navigation solutions need to take vehicle vibrations into consideration as they affect inertial measurements in terms of angular rates and specific forces read out.

The contribution of this paper is in designing different navigation solutions, tuning their parameters and in comparing their performances and analyzing their robustness to GNSS outages and vehicle harsh environment with high vibration impacts.

2.1. Extended Kalman filtering

Extended Kalman filters (EKFs) are used as nonlinear estimators for navigation solutions. More details about the EKF algorithm can be found in (Grewal & Andrews, 2001). A basic example of an INS/GNSS integration scheme using a 12-dimensional state vector (8) containing position, velocity, attitude, and gyro bias, all driven

by a control vector $\boldsymbol{u}$ consisting of measured angular rates and specific forces, is shown in Fig. 2. The measurement vector (9) is 3-dimensional and includes only GNSS based position converted to the local navigation coordinate frame (Nemra & Aouf, 2010). The process with a transition function (10) is capable of filtering GNSS based position and use it for attitude corrections and gyro bias estimation. The performance of this kind of estimation can be found in (Hansen, Rohac, Sipos, Johansen, & Fossen, 2016). This approach is not robust to GNSS outages since it does not allow for estimation of ACC bias. Therefore, several enhanced models were designed and studied and can be found in following sections.

$$\hat{\boldsymbol{x}} = [\hat{\boldsymbol{p}}^n \quad \hat{\boldsymbol{v}}^b \quad \hat{\boldsymbol{\Theta}} \quad \hat{\boldsymbol{b}}_g]^T; \; \boldsymbol{u} = \begin{bmatrix} \boldsymbol{\omega}_{ib}^b & \boldsymbol{f}^b \end{bmatrix}^T \tag{8}$$

$$\boldsymbol{z} = [\boldsymbol{p}_{GNSS}^n]; \; \hat{\boldsymbol{z}}_k = \begin{bmatrix} \hat{\boldsymbol{p}}^n \end{bmatrix} \tag{9}$$

$$\boldsymbol{x}_{k+1} = \boldsymbol{x}_k + T \cdot \begin{bmatrix} \boldsymbol{C}_b^n \boldsymbol{v}_b \\ \boldsymbol{f}^b + \boldsymbol{v}^b \times (\boldsymbol{\omega}_{ib}^b - \boldsymbol{b}_g) - \boldsymbol{C}_n^b \boldsymbol{g}^n \\ \begin{bmatrix} 1 & \sin\phi \tan\theta & \cos\phi \tan\theta \\ 0 & \cos\phi & -\sin\phi \\ 0 & \sin\phi \sec\theta & \cos\phi \sec\theta \end{bmatrix} (\boldsymbol{\omega}_{ib}^b - \boldsymbol{b}_g) \\ \boldsymbol{b}_g \end{bmatrix} \tag{10}$$

2.1.1. Single structure EKF based estimator

Even if we are using a loosely coupled integration scheme in both approaches, a single structure EKF, shown in Fig. 3, provides in one block both position/velocity estimation as well as attitude estimation. That provides the strongest connection between GNSS based position and velocity measurements and the attitude estimation, and furthermore, ensures all inputs with their noise satisfy a condition of white noise character. The white noise character ensures according to the KF theory the best and stable KF/EKF performance. The state vector (11) against the 12-state EKF based estimator described by (8)–(10) includes even accelerations and angular rates modeled as a random constant and bias of all ACCs and gyros. Acceleration and angular rate states are generally modeled as an exponentially correlated process; however, large correlation time needs to be considered and thus it all comes close to a random constant model with a white noise as a driving source. The bias is also modeled as a random constant which corresponds to the initial offset estimation. It is supported by added driven noise which makes bias time varying as it is supposed to; nevertheless, a standard deviation of the driven noise differs. A time update of the state vector respects a transition function in (12) with a zero control vector. All measurements get into the model via a measurement vector (13). A very important part of the measurement vector is a specific force compilation with a compensated centripetal force applied when the vehicle is moving and turning simultaneously, i.e. experiencing dynamic motion.

$$\hat{\boldsymbol{x}} = [\hat{\boldsymbol{p}}^n \quad \hat{\boldsymbol{v}}^b \quad \hat{\boldsymbol{a}}^b \quad \hat{\boldsymbol{\Theta}} \quad \hat{\boldsymbol{\omega}}_{ib}^b \quad \hat{\boldsymbol{b}}_a \quad \hat{\boldsymbol{b}}_g]^T, \; \boldsymbol{u} = 0 \tag{11}$$

$$\boldsymbol{x}_{k+1} = \boldsymbol{x}_k + \begin{bmatrix} \boldsymbol{C}_b^n \cdot T \cdot \left(\boldsymbol{v}^b + \frac{1}{2}T \cdot \boldsymbol{a}^b\right) \\ T \cdot \boldsymbol{a}^b \\ \boldsymbol{0}_{3x3} \\ T \cdot \begin{bmatrix} 1 & \sin\varphi \cos\theta & \cos\varphi \cos\theta \\ 0 & \cos\varphi & -\sin\varphi \\ 0 & \sin\varphi \sec\theta & \cos\varphi \sec\theta \end{bmatrix} \cdot \boldsymbol{\omega}_{ib}^b \\ \boldsymbol{0}_{3x3} \\ \boldsymbol{0}_{3x3} \\ \boldsymbol{0}_{3x3} \end{bmatrix} \tag{12}$$
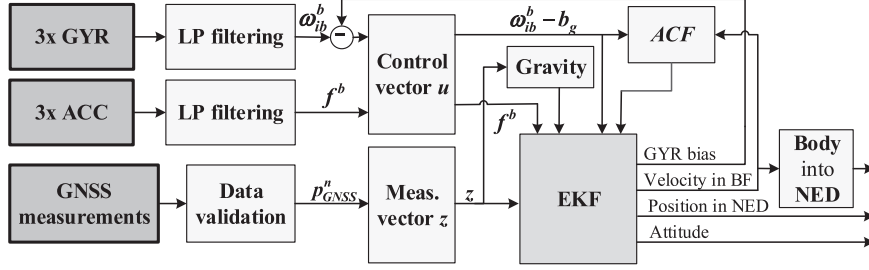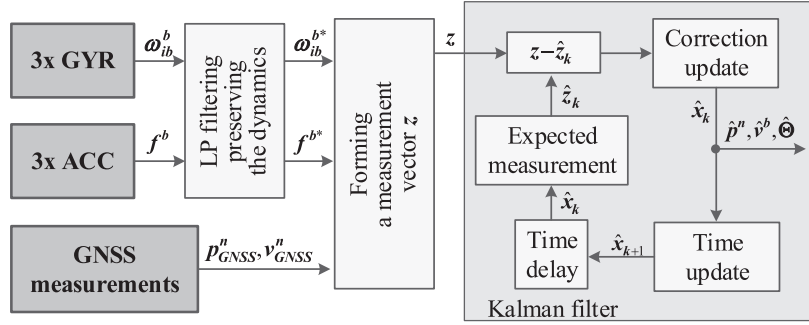
Fig. 2. Single structure 12-state EKF based estimator.

Fig. 3. Single structure EKF based estimator of position, velocity, and attitude.

$$z = \begin{bmatrix} p^n_{GNSS} \\ v^n_{GNSS} \\ f^{b*} \\ \omega^b_{ib} \end{bmatrix}; \quad \hat{z}_k = \begin{bmatrix} \hat{p}^n \\ \hat{C}^n_b \hat{v}^b \\ \hat{a}^b - \hat{C}^b_n \begin{bmatrix} 0 & 0 & 1 \end{bmatrix}^T + \hat{\omega}^b_{ib} \times \hat{v}^b + \hat{b}_a \\ \hat{\omega}^b_{ib} + \hat{b}_g \end{bmatrix},$$
(13)

where

$$C^n_b = \begin{bmatrix} c_\theta c_\psi & -c_\phi s_\psi + s_\phi s_\theta c_\psi & s_\phi s_\psi + c_\phi s_\theta c_\psi \\ c_\theta s_\psi & c_\phi c_\psi + s_\phi s_\theta s_\psi & -s_\phi c_\psi + c_\phi s_\theta s_\psi \\ -s_\theta & s_\phi c_\theta & c_\phi c_\theta \end{bmatrix}$$
(14)

where $c_\phi = \cos\phi$, $s_\phi = \sin\phi$, etc.

The model described by (11)–(14) assumes a vehicle with some slower dynamic, i.e. longer correlation times, and thus it allows to use random constant models for angular rates and acceleration modeling with sufficiently high driving noise. For more details about concrete values please see Appendix A.

2.1.2. Dual structure EKF based estimator

This section describes the details of the dual structure EKF for the PVA estimation. The overall estimation process is divided into two main sections; an Attitude estimator and a Position/Velocity estimator. By using cascaded Kalman filtering, this method avoids the need to propagate additional states, resulting in the covariance propagation to become more computationally efficient. The novelty in the proposed algorithms lies in the imposed state constraints in the attitude estimation for evaluating the external forces on the ACCs. The overall estimation process is shown in a block scheme in Fig. 4. In the following sections, each part of the estimator structure will be introduced in detail.

2.1.2.1. Attitude EKF based estimator.
The vehicle attitude is represented in this case by Euler angles since we assume singularity

free calculations. This assumption comes from the operation conditions and limits of any aircraft. The state vector (15) is updated via a transition function (16) when angular rates form a control vector. Expected measurements (17) are related to ACC readings when only gravity affects the sensor, which means non dynamic motion.

$$\hat{x} = \begin{bmatrix} \hat{\Theta} & \hat{b}_g \end{bmatrix}^T, u = \omega^b_{ib} = \begin{bmatrix} \omega_{b_x}, & \omega_{b_y}, & \omega_{b_z} \end{bmatrix}^T$$
(15)

$$x_{k+1} = x_k +$$
$$+ T \cdot \begin{bmatrix} 1 & \sin\phi \tan\theta & \cos\phi \tan\theta \\ 0 & \cos\phi & -\sin\phi \\ 0 & \sin\phi \sec\theta & \cos\phi \sec\theta \\ & 0 & \\ & 0 & \\ & 0 & \end{bmatrix} \left(\begin{bmatrix} \omega_{b_x} \\ \omega_{b_y} \\ \omega_{b_z} \end{bmatrix} - \begin{bmatrix} b_{g_x} \\ b_{g_y} \\ b_{g_z} \end{bmatrix} \right)$$
(16)

$$z = \begin{bmatrix} f_x \\ f_y \\ f_z \\ \psi_{GNSS} \end{bmatrix}, \quad \hat{z}_k = \begin{bmatrix} -\sin\theta \\ \sin\phi\cos\theta \\ \cos\phi\cos\theta \\ \psi \end{bmatrix}$$
(17)

The heading (ψ) is evaluated based on the GNSS velocities as

$$\psi_{GNSS} = atan2\left(V_{GNSS_{East}}, V_{GNSS_{North}}\right),$$
(18)

and is used for aiding when following condition is fulfilled.

$$norm_{Vel_{GNSS}} = \sqrt{V_{GNSS_{North}}^2 + V_{GNSS_{East}}^2} > 3 \ m/s$$
(19)

We note that usage of GNSS velocities provides the course angle, which is equal to the heading angle only when the crab angle is zero. This assumption leads to a reasonable approximation when winds and curves are not too large. If the $norm_{Vel_{GNSS}}$ is less than 3 m/s, then the heading estimation based on GNSS velocity is noisy. If the ACC and gyro readings are affected by vibration arising from
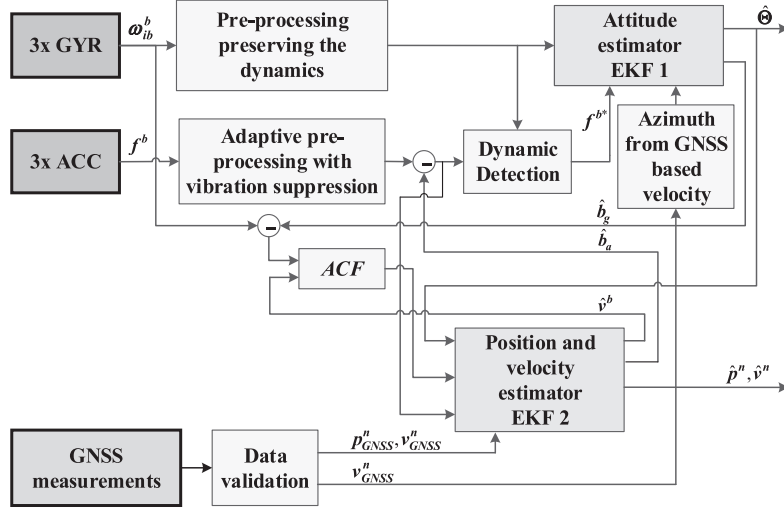
Fig. 4. Enhanced IMU/GNSS loosely-coupled integration scheme using a dual structure EKF estimator.

the vehicle's structures, an adaptive pre-processing can be applied before the data are used inside EKF, for details on adaptive filtering for reducing vibration impact please see (Alam & Rohac, 2015).

As shown in the block diagram in Fig. 4, the gyro bias is fed back to the gyro input. One of the crucial part in the attitude estimator is the dynamic detection. The ACC data are only used as measurement whenever there is no significant dynamics detected in the vehicle's motion.

2.1.2.2. Dynamic detection. For the ACC based aiding in an attitude estimator it is crucial to recognize conditions under which ACC readings are affected by only gravity, which means no dynamic change in the motion. For this purpose, we have designed dynamics detector formed by 3 parameters which are monitored simultaneously for particular data history. In our case it was set to a history window of 0.5 s. These monitoring parameters are:

1. The norm of the ACC readings

$$ACC_{norm} = \sqrt{f_x^2 + f_y^2 + f_z^2} \tag{20}$$

2. The norm of the gyro data

$$GYR_{norm} = \sqrt{\left(\omega_{b_x} - b_{g_x}\right)^2 + \left(\omega_{b_y} - b_{g_y}\right)^2 + \left(\omega_{b_z} - b_{g_z}\right)^2} \tag{21}$$

3. The rate of heading change

$$\dot{\psi} = \left(\frac{\left(\omega_{b_y} - b_{g_y}\right)sin\phi}{cos\theta} + \frac{\left(\omega_{b_z} - b_{g_z}\right)cos\phi}{cos\theta} \right) \tag{22}$$

In an ideal case only ACC_{norm} can be monitored for detecting dynamics; and when it equals to 1g, no dynamic conditions could be considered. However, under real operating conditions under harsh environment bounds/thresholds should be set to allow possibility for variation along with monitoring the parameters from (20) to (22). We have thus considered following conditions and no dynamic motion is assumed to be present when all three conditions are met simultaneously.

Condition 1: $|ACC_{norm} - 1g| < threshold_{ACC}$.
Condition 2: $|GYR_{norm}| < threshold_{GYR}$.
Condition 3: $|\dot{\psi}| < threshold_{ARS}$.

The threshold values are chosen depending on a vehicle type and/or adaptively modified according to operational conditions. The three parameters from (20) to (22) are monitored for 0.5 s from the history of the estimation, when all Conditions 1-3 are met throughout this window of 0.5 s, it is considered that ACC output is affected just by gravity and thus ACC based attitude estimation are used for compensating the attitude obtained primarily by free integration of GYR data.

2.1.2.3. Position/velocity EKF based estimator. The estimator estimates position in NED frame, velocity in the body-frame and ACC bias of the vehicles while using GNSS position and velocity as aiding measurements. The state vector (23) is updated via the transition function (24) where the control vector $\boldsymbol{u}$ (23) contains ACC measurements in terms of a specific force, Euler angles and anti-centrifugal force. The measurement vector (25) contains position estimates from GNSS and downward velocity in body axis. The estimation equations are given as:

$$\hat{\boldsymbol{x}} = \begin{bmatrix} \hat{\boldsymbol{p}}^n & \hat{\boldsymbol{v}}^b & \hat{\boldsymbol{b}}_a \end{bmatrix}^T, \quad \boldsymbol{u} = \begin{bmatrix} \boldsymbol{f}^b, & \boldsymbol{\Theta}, & \boldsymbol{ACF} \end{bmatrix}^T, \tag{23}$$

$$\boldsymbol{x}_{k+1} = \boldsymbol{x}_k + T \times \begin{bmatrix} \boldsymbol{C}_b^n \boldsymbol{v}^b \\ \left(\begin{bmatrix} f_x \\ f_y \\ f_z \end{bmatrix} - \begin{bmatrix} b_{ax} \\ b_{ay} \\ b_{az} \end{bmatrix} \right) + \boldsymbol{C}_b^{nT} \begin{bmatrix} 0 \\ 0 \\ 1 \end{bmatrix} - \boldsymbol{ACF} \\ 0 \\ 0 \\ 0 \end{bmatrix}, \tag{24}$$

$$\boldsymbol{z} = \begin{bmatrix} \boldsymbol{p}_{GNSS}^n \\ v_{GNSS_{Down}}^b \end{bmatrix}, \quad \hat{\boldsymbol{z}}_k = \begin{bmatrix} \hat{\boldsymbol{p}}^n \\ \hat{v}_{Down}^b \end{bmatrix}. \tag{25}$$

The $\boldsymbol{ACF}$ is the vector of anti-centrifugal force experienced by the vehicle and is calculated as:

$$\boldsymbol{ACF} = - \begin{pmatrix} v\left(\omega_{b_z} - b_{g_z}\right) - w\left(\omega_{b_y} - b_{g_y}\right) \\ -u\left(\omega_{b_z} - b_{g_z}\right) + w\left(\omega_{b_x} - b_{g_x}\right) \\ u\left(\omega_{b_y} - b_{g_y}\right) - v\left(\omega_{b_x} - b_{g_x}\right) \end{pmatrix}. \tag{26}$$

As shown in the estimation block diagram in Fig. 4, it is important to validate GNSS data before they are processed. Any bad

sample from the GNSS data may cause an inaccurate estimation of the state vector. The GNSS data validation is further explained in the next section.

2.1.2.4. GNSS data validation. Position estimated from the GNSS data is validated using quadratic polynomial fitting. The validation is carried out as follows. At first a GNSS position is predicted based on the 2 s data history of GNSS positions using quadratic polynomial fitting RMSE minimization. Then the deviation between the latest GNSS position and the predicted GNSS position is determined as:

$$dev_{GNSS\,pos} = lastest_{GNSS_{pos}} - predicted_{GNSS_{pos}}. \tag{27}$$

If the magnitude of the deviation is greater than a threshold value, then the latest GNSS data are discarded.

$$if \; \left| dev_{GNSS\,pos} \right| > thershold_{GNSS}$$
$$\Rightarrow discard \; the \; latest \; GNSS \; position \tag{28}$$

The advantage of having velocity in the BF as a state in the Position/Velocity estimator is that, when the vehicle doesn't experience side-slips or vertical decent, the concept of "Perfect Measurement" can be used. That means during the outage of GNSS signal, we can provide/assume velocity in Y- and Z-axis in the BF is zero. This assumption helps stabilizing the ACC bias estimate in case of GNSS signal outages.

2.2. Nonlinear observer

The kinematic equations describing position, $\boldsymbol{p}^e$, linear velocity, $\boldsymbol{v}^e$, attitude in the quaternion, $\boldsymbol{q}^e_b$, and GYR or ACC bias $\boldsymbol{b}^b$ are given as:

$$\dot{\boldsymbol{p}}^{\boldsymbol{e}} = \boldsymbol{v}^{\boldsymbol{e}}, \tag{29}$$

$$\dot{\boldsymbol{v}}^{\boldsymbol{e}} = -2\left(\boldsymbol{\omega}^{\boldsymbol{e}}_{\boldsymbol{ie}}\times\right)\boldsymbol{v}^{\boldsymbol{e}} + \boldsymbol{f}^{\boldsymbol{e}} + \boldsymbol{g}^{\boldsymbol{e}}\left(\boldsymbol{p}^{\boldsymbol{e}}\right), \tag{30}$$

$$\dot{\boldsymbol{q}}^{\boldsymbol{e}}_{\boldsymbol{b}} = \frac{1}{2}\boldsymbol{q}^{\boldsymbol{e}}_{\boldsymbol{b}} \otimes \bar{\boldsymbol{\omega}}^{\boldsymbol{b}}_{\boldsymbol{ib}} - \frac{1}{2}\bar{\boldsymbol{\omega}}^{\boldsymbol{e}}_{\boldsymbol{ie}} \otimes \boldsymbol{q}^{\boldsymbol{e}}_{\boldsymbol{b}}, \tag{31}$$

$$\dot{\boldsymbol{b}}^b_g = 0, \dot{\boldsymbol{b}}^b_a = 0. \tag{32}$$

The position and velocity are given in the ECEF, while the gyro and ACC bias is in the BF, and the attitude is expressed as a unit quaternion describing the rotation between BF and ECEF. The gravity vector, $\boldsymbol{g}^{\boldsymbol{e}}(\,\cdot\,)$, is assumed known for a given position, while a vector $\boldsymbol{x} \in \mathbb{R}^3$ can be represented as a quaternion with zero real part and vector part $\boldsymbol{x}$, i.e. $\bar{\boldsymbol{x}} = [0; \boldsymbol{x}]$. The Earth rotation, $\boldsymbol{\omega}^{\boldsymbol{e}}_{\boldsymbol{ie}}$, is constant and known, and the product of two quaternions, $\boldsymbol{q}_1$ and $\boldsymbol{q}_2$, is given as $\boldsymbol{q}_1 \otimes \boldsymbol{q}_2$. The gyro bias, $\boldsymbol{b}^b_g$, and ACC bias, $\boldsymbol{b}^b_a$, are considered to be slowly time-varying.

2.2.1. Nonlinear GNSS/INS integration

The nonlinear observer structure consists of two parts; an attitude estimator and a translational motion observer, (Grip et al., 2013). The attitude estimator determines the vehicle attitude from inertial measurements, whereas the translational motion observer utilizes global measurements provided by a GNSS receiver as well as specific force measurements.

An estimate of the specific force in the ECEF is fed back from the TMO to the attitude estimator, making the structure a feedback interconnection of two subsystems. The observer structure was shown to be semi-globally stable in (Grip et al., 2013). The observer structure can be seen in Fig. 5. In the following sections, each part of the observer structure will be introduced in detail.
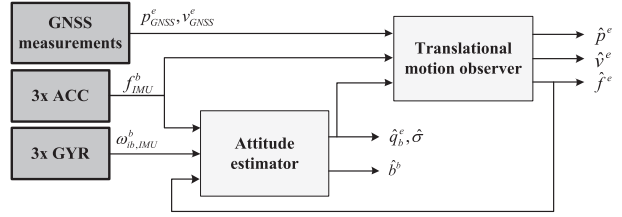

Fig. 5. Nonlinear observer structure consisting of attitude and translational motion.

2.2.2. Attitude estimation

The vehicle attitude is represented by a unit quaternion, $\hat{q}^e_b$, describing the rotation from BF to ECEF. Furthermore, the attitude estimator also determines a gyro bias estimate, $\hat{b}^b$, to compensate for sensor drift. The attitude estimation is given by, (Grip et al., 2012; Mahony et al., 2009):

$$\dot{\hat{\boldsymbol{q}}}^e_b = \frac{1}{2}\hat{\boldsymbol{q}}^b_b \otimes \left(\bar{\boldsymbol{\omega}}^b_{ib,IMU} - \overline{\hat{\boldsymbol{b}}^b_g} + \bar{\hat{\boldsymbol{\sigma}}}\right) - \frac{1}{2}\bar{\boldsymbol{\omega}}^e_{ie} \otimes \hat{\boldsymbol{q}}^e_b, \tag{33}$$

$$\dot{\hat{\boldsymbol{b}}}^b_g = \text{Proj}\left(-k_I\hat{\boldsymbol{\sigma}}, \left\|\hat{\boldsymbol{b}}^b_g\right\|_2 \le M_{\hat{b}}\right). \tag{34}$$

Here the projection function, Proj$(\,\cdot\,, \cdot)$, limits the gyro bias estimate to be within a sphere of radius $M_{\hat{b}}$, where k_I is a constant gain and $\hat{\boldsymbol{\sigma}}$ is an injection term. The injection term is based on the comparison of two vectors in the BF, $\boldsymbol{v}^b_1$ and $\boldsymbol{v}^b_2$, with two corresponding vectors in the ECEF, $\boldsymbol{v}^e_1$ and $\boldsymbol{v}^e_2$:

$$\hat{\boldsymbol{\sigma}} = k_1\boldsymbol{v}^b_1 \times \boldsymbol{R}\left(\hat{\boldsymbol{q}}^b_b\right)^T\boldsymbol{v}^e_1 + k_2\boldsymbol{v}^b_2 \times \boldsymbol{R}\left(\hat{\boldsymbol{q}}^e_b\right)^T\boldsymbol{v}^e_2.$$

The gains, k_1 and k_2, are positive and sufficiently large tuning constants. The vectors can be chosen in various ways utilizing e.g. magnetometer or pressure measurements. Here the vectors are chosen, based on specific force and heading from the GNSS velocity, as:

$$\boldsymbol{v}^b_1 = \frac{\boldsymbol{f}^b_{IMU}}{\left\|\boldsymbol{f}^b_{IMU}\right\|_2}, \quad \boldsymbol{v}^e_1 = \frac{\hat{\boldsymbol{f}}^e}{\left\|\hat{\boldsymbol{f}}^e\right\|_2}, \quad \boldsymbol{v}^b_2 = \begin{bmatrix} \cos(\psi) \\ -\sin(\psi) \\ 0 \end{bmatrix}, \quad \boldsymbol{v}^e_2 = \boldsymbol{R}^e_n\begin{bmatrix} 1 \\ 0 \\ 0 \end{bmatrix},$$

where the specific force estimate, $\hat{\boldsymbol{f}}^e$, is determined by the translational motion observer. The reference vector $\boldsymbol{v}^e_2$ denotes the direction North decomposed in the ECEF, while the corresponding body vector, $\boldsymbol{v}^b_2$, utilizes the heading angle ψ. The heading angle can be obtained from a compass or in this case from GNSS velocity measurements in NED:

$$\psi = \tan^{-1}\left(\frac{v_e}{v_n}\right),$$

where v_n and v_e signifies the velocity in North and East direction.

2.2.2.1. Accelerometer bias estimation. The bias of the accelerometer measurements can be considered a slowly time-varying value added to the true measurements; $\boldsymbol{f}^b_{IMU} = \boldsymbol{f}^b + \boldsymbol{b}^b_a$. Considering a combination of parameters $\boldsymbol{\theta} = [\|\hat{\boldsymbol{b}}^b_a\|_2, (\hat{\boldsymbol{b}}^b_a)^T]^T$ and $\phi = [1, -2(\boldsymbol{f}^b_{IMU})^T]^T$ the measurement for the injection term can be expressed; $y_f = \|\hat{\boldsymbol{b}}^b_a\|_2 - 2(\boldsymbol{f}^b_{IMU})^T\hat{\boldsymbol{b}}^b_a$, as presented in Grip et al. (2012, 2016). The combination vector propagation is then expressed as, (Grip et al., 2012):

$$\dot{\hat{\boldsymbol{\theta}}} = \boldsymbol{\Gamma}\phi\left(y_f - \phi^T\hat{\boldsymbol{\theta}}\right),$$

where $\boldsymbol{\Gamma}$ is a positive-definite symmetric gain matrix. The ACC bias is carried out under the assumption that there is sufficient excitation of the vehicle for the ACC to experience versatile acceleration.

Formally this requirement is expressed as an assumption that:

$$\int_{t}^{t+T} \phi(\tau)\phi^T(\tau)d\tau \geq \epsilon I,$$

where $\epsilon > 0$ and $T > 0$ such that for each $t \geq 0$ the condition is satisfied and the persistently excitation assumption is valid.

The ACC bias estimation can be implemented similarly to the gyro bias estimation, (Grip, Fossen, Johansen, & Saberi, 2016):

$$\dot{\hat{\boldsymbol{\theta}}} = \mathrm{Proj}\left(\boldsymbol{\Gamma}\phi\left(\hat{\boldsymbol{y}}_f - \phi^T\hat{\boldsymbol{\theta}}\right), \left\|\hat{\boldsymbol{\theta}}\right\|_2 \leq M_{\hat{w}}\right),$$

where $M_{\hat{w}}$ is a bound on the length of the bias vector.

2.2.3. Translational motion observer

The translational motion observer estimates position, linear velocity and specific force of the vehicle by using injection terms based on the difference in measured and estimated global position. A GNSS receiver provides the global position measurements. The TMO is given as:

$$\dot{\hat{\boldsymbol{p}}}^e = \hat{\boldsymbol{v}}^e + \boldsymbol{\theta}\boldsymbol{K}_{pp}\left(\boldsymbol{p}_{GNSS}^e - \hat{\boldsymbol{p}}^e\right) + \boldsymbol{K}_{pv}\left(\boldsymbol{v}_{GNSS}^e - \boldsymbol{C}_v\hat{\boldsymbol{v}}^e\right), \tag{35}$$

$$\dot{\hat{\boldsymbol{v}}}^e = -2\left(\boldsymbol{\omega}_{ie}^e \times\right)\hat{\boldsymbol{v}}^e + \hat{\boldsymbol{f}}^e + \boldsymbol{g}^e\left(\hat{\boldsymbol{p}}^e\right) + \boldsymbol{\theta}^2\boldsymbol{K}_{vp}\left(\boldsymbol{p}_{GNSS}^e - \hat{\boldsymbol{p}}^e\right) \\ + \boldsymbol{\theta}\boldsymbol{K}_{vv}\left(\boldsymbol{v}_{GNSS}^e - \boldsymbol{C}_v\hat{\boldsymbol{v}}^e\right) \tag{36}$$

$$\dot{\boldsymbol{\xi}} = -\boldsymbol{R}\left(\hat{\boldsymbol{q}}_b^e\right)\left(\hat{\boldsymbol{\sigma}}\times\right)\boldsymbol{f}_{IMU}^b + \boldsymbol{\theta}^3\boldsymbol{K}_{\xi p}\left(\boldsymbol{p}_{GNSS}^e - \hat{\boldsymbol{p}}^e\right) + \boldsymbol{\theta}^2\boldsymbol{K}_{\xi v}\left(\boldsymbol{v}_{GNSS}^e - \boldsymbol{C}_v\hat{\boldsymbol{v}}^e\right), \tag{37}$$

$$\hat{\boldsymbol{f}}^e = \boldsymbol{R}\left(\hat{\boldsymbol{q}}_b^e\right)\left(\boldsymbol{f}_{IMU}^b - \boldsymbol{b}_a^b\right) + \boldsymbol{\xi}. \tag{38}$$

Here an auxiliary state, $\boldsymbol{\xi}$, has been introduced for estimation of the specific force. The tuning parameter θ is typically chosen to be equal to 1. The additional injection term based on linear velocity measurements and estimates was shown in Grip, Fossen, Johansen, and Saberi (2012a) not to be essential to the observer stability, however, it does increase performance. Hence the matrix C_v can be chosen to be zero.

Introducing the error variables; $\tilde{\boldsymbol{p}} = \boldsymbol{p}^e - \hat{\boldsymbol{p}}^e$, $\tilde{\boldsymbol{v}} = \boldsymbol{v}^e - \hat{\boldsymbol{v}}^e$, and $\tilde{\boldsymbol{f}} = \boldsymbol{f}^e - \hat{\boldsymbol{f}}^e$, the state vector of the error dynamics can be stated as $\tilde{\boldsymbol{x}} = [\tilde{\boldsymbol{p}}; \tilde{\boldsymbol{v}}; \tilde{\boldsymbol{f}}]$. The gains of the translational motion observer can then be chosen to satisfy $(\boldsymbol{A} - \boldsymbol{KC})$ being stable where:

$$\boldsymbol{A} = \begin{bmatrix} \boldsymbol{0}_{3x3} & \boldsymbol{I}_{3x3} & \boldsymbol{0}_{3x3} \\ \boldsymbol{0}_{3x3} & \boldsymbol{0}_{3x3} & \boldsymbol{I}_{3x3} \\ \boldsymbol{0}_{3x3} & \boldsymbol{0}_{3x3} & \boldsymbol{0}_{3x3} \end{bmatrix}, \quad \boldsymbol{C} = \begin{bmatrix} \boldsymbol{I}_{3x3} & \boldsymbol{0}_{3x3} & \boldsymbol{0}_{3x3} \\ \boldsymbol{0}_{3x3} & \boldsymbol{I}_{3x3} & \boldsymbol{0}_{3x3} \end{bmatrix},$$

$$\boldsymbol{K} = \begin{bmatrix} \boldsymbol{K}_{pp} & \boldsymbol{K}_{pv} \\ \boldsymbol{K}_{vp} & \boldsymbol{K}_{vv} \\ \boldsymbol{K}_{\xi p} & \boldsymbol{K}_{\xi v} \end{bmatrix}. \tag{39}$$

The gains can be chosen to be constant without issue to the stability of the observer. However, in Bryne, Fossen, and Johansen (2014) it was shown that time-varying gains give faster convergence and aid in sensor noise suppression. Since the translational motion observer is similar in structure to the EKF the gain matrix $\boldsymbol{K}$ can be determined similarly by solving a Riccati equation. Furthermore, it is possible to update the time-varying gain matrix on a slower time scale, leading to a smaller computational footprint.

3. Experimental setup

The flight experiment was conducted using a Slingsby T67C aircraft (General Aviation category) shown in Fig. 6 (left). To obtain GNSS data and inertial data, we have used a DMU-10 (Silicon & Sensing, 2016) IMU which was connected with a MAX8W (μBlox) GNSS receiver. The DMU-10 is of commercial grade with 6 degree of freedom MEMS based IMU consisting of 3 gyros, 3 ACCs

and a temperature sensor. The data from the GNSS receiver and DMU-10 were pooled by a microcontroller STM32F746ZGT6 (STMicroeletcronics) and saved as raw data to a SD logger through CAN bus with CANAerospace protocol incorporated. The data from the IMU and GNSS receiver were sampled at 200 Hz and 5 Hz respectively. The data from an X91+ GNSS receiver were sampled at 5 Hz and were related to measurements obtained from GNSS stationary reference station placed in Pribram city, which is a part of Czech Reference GNSS Station Network (CZEPOS). The GNSS data were processed in the open source RTKlib to give an accurate RTK-GNSS based position used in our paper as a reference for comparing results of proposed approaches. The navigation unit was mounted in a sensory compartment inside a Pelicase 1450 as depicted in Fig. 6 (right) and placed onboard the aircraft as shown in Fig. 7 (left). The GNSS antennae were mounted on the cabin cover as shown in Fig. 7 (right). More details about the parameters of DMU-10 unit can be found at Fig. 8.

3.1. Allan variance analysis

The Allan Variance (AVAR) analysis is a frequently used tool to identify stochastic parameters of inertial sensors. It is a time-domain approach to analyze time series of data in terms of the noise characteristics. D. W. Allan introduced the AVAR in 1966 (Allan, 1966). Originally, it was oriented at the study of oscillator stability; however, after its first publication this kind of analysis was adopted for general noisy data characterization. Because of the close analogies to inertial sensors, the AVAR has also been included in the IEEE Standards, (e.g. IEEE Std. 1293; IEEE Std. 528; IEEE Std. 647). We thus carried out AVAR analysis on the DMU-10 unit used in the performed experiments, and further on fiber optic gyro DSP-3100 (KVH manufacturer) and a quartz accelerometer INN-204 (Innalabs manufacturer) to compare noise characteristics of DMU-10 with tactical grade inertial sensors. The results are depicted in Fig. 9 and summarized in Table 1. The results fit with datasheet values presented at Fig. 8.

The robustness of the navigation solution is always related to estimate bias of inertial sensors as accurately as possible via means of aiding systems when they are available. In the case of the studied DMU-10 IMU the bias instability according to Fig. 9 causes a standard deviation of 0.0014°/s in angular rates and 26 μg in measured specific force. To design such a FIR filter capable to get a bias instability out of an original signal it was required first to decimate output data sampling frequency, in our case it was to 1 Hz, and then to design FIR filter with an equiripple window with parameters as shown in Fig. 10. The cut-off frequency was set to 0.001 Hz, which means 0.002π rad/sample as a normalized frequency. The result of a zero-phase filtering (MATLAB function "filtfilt") is depicted in Fig. 11. A standard deviation reached in the case of angular rate was 0.0034°/s and 58 μg in the case of ACC data. Even the resultant standard deviations did not reach the values evaluated by AVAR, they can still show an estimated bias progression which is a key element of robustness analysis given in Section 4. Obtained values can thus serve as a qualificator when a complete navigation is analyzed and inertial sensor's bias estimated.

4. Experimental verification

4.1. Description of the experiment

The flight included various flight patterns including slow turns and rapid altitude changes, see Fig. 12 (left). The flight included rapid altitude change from 450 m up to 1040 m and vice-versa. The flight took about 33 min including rolling, take-off, climb, cruise, descent, and landing as marked in Fig. 12 (right). Since different stages during the flight had different conditions for the navigation

45

Fig. 6. Slingsby T67C aircraft (left), the sensory compartment inside Pelicase 1450 (right). (For interpretation of figures in color, the reader is referred to the web version of this article.)

Fig. 7. Measurement assembly onboard aircraft Slingsby T67C in a sensory compartment with a referential GNSS system on the top (left) and GNSS antennae mounted on the cabin cover (right).

Table 1
Summarized key stochastic parameters from the AVAR analysis.

	Parameter	DMU10 Fs = 200 Hz	DSP-3100 Fs = 1kHz	INN-204 Fs = 1kHz
GYR	$ARW(°/\sqrt{h})$	0.35	0.03	X
	$BIN(°/h)$	7.53	0.60	X
ACC	$VRW(m/s/\sqrt{h})$	0.05	X	0.01
	BIN (mg)	0.04	x	0.01
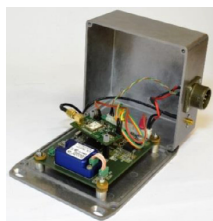
DMU-10 unit datasheet values:

Measurement range:	*±300 deg/s, ±10g*
In-Run bias stability:	*≤ 15 deg/h, 0.05mg*
A/V random walk:	*≤ 0.4 deg/ √h, 0.05 m/s/√h*
Noise in BW=100 Hz:	*0.1 deg/s, 1 mg*
g-sensitivity:	*0.003 deg/s rms /g*

Fig. 8. Measurement unit DMU-10 (left) with its datasheet values (right) (Silicon, & Sensing, 2016).

unit to operate, we divided the obtained data according to particular flight stages and analyzed the navigation solution performance separately in each of them. During the flight, there were conditions with high dynamics reaching angular rates up to $±50°/s$ and values of specific force of $−5.2$ g and $+2.3$ g.

Moreover, data suffered from strong influence of vibrations with a frequency spectrum varying according to the propeller RPM. Figs. 13 and 14 thus indicate vibration differences related to spe-

cific force progressions at particular stages, i.e. rolling and taking-off, in terms of time and frequency domain. It can be seen that the effects of propeller rotation is strongly influenced at 20 Hz.

Due to having access to compare our final estimation with a reference our experimental setup included a dual-frequency GNSS receiver X91+ (CHC) with output processed by RTKlib (www.rtklib.com). The static accuracy of the reference position was about 1 cm (1σ), when the RTK based solution reached the fix status and 5 cm (1σ) when the solution corresponded to the float status. During the flight presented in this paper the fix status occurred in 92.8%, in 7.2% there was a float status (see Fig. 12 (left)). Nevertheless, at closer look after the evaluation of single point GNSS and RTK-GNSS based solutions it was possible to see the difference in position estimate. Observed deviations are shown in Fig. 15, where as it can be seen the differences between these estimates vary depending on dynamic changes during maneuvering.

4.2. Performance analysis under GNSS ON conditions

The estimation was carried out using three different approaches as described in Section 2. The 9 fundamental parameters for nav-
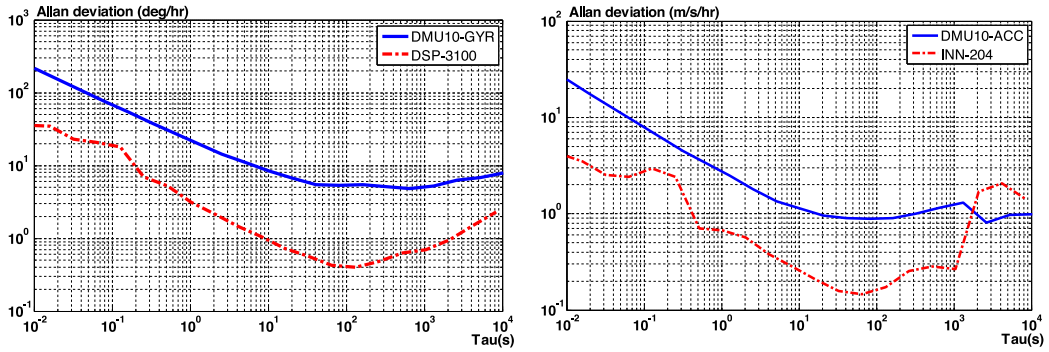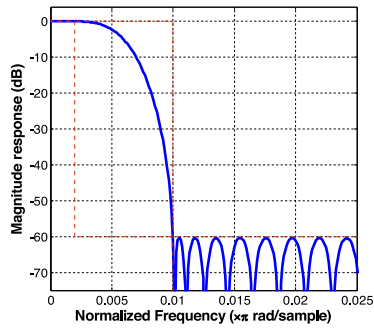
Fig. 9. Allan deviation plot of a tactical grade gyro DSP-3100 and gyro of DMU10 unit (left), a tactical grade accelerometer INN-204 and accelerometer of DMU10 unit (right).

Parameters of the filter:

Sampling Frequency: N/A (normalized frequency)
Passband Edge: 0.0020
3-dB Point: 0.0052
6-dB Point: 0.0061
Stopband Edge: 0.0100
Passband Ripple: 0.0095 dB
Stopband Atten.:   -60.2671 dB
Transition Width: 0.0080
Window used: equiripple
Order: 857

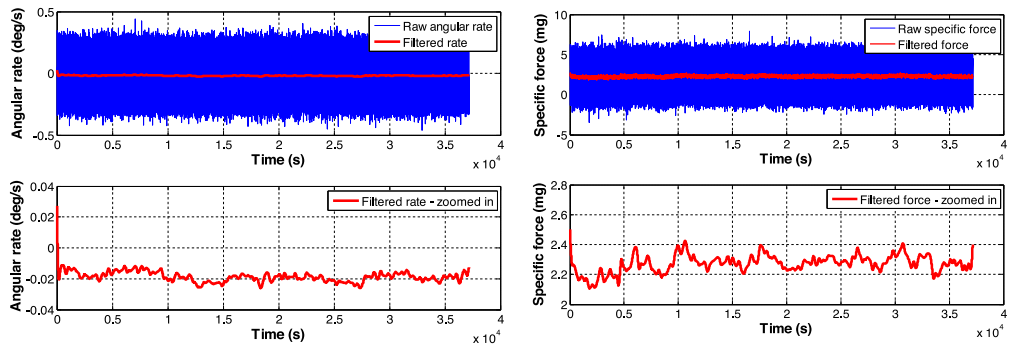**Fig. 10.** FIR filter magnitude response with its parameters.

Fig. 11. Progression of a raw angular rate (left) and specific force (right) – DMU10 IMU – with its filtered variant (top), detailed progression (bottom).
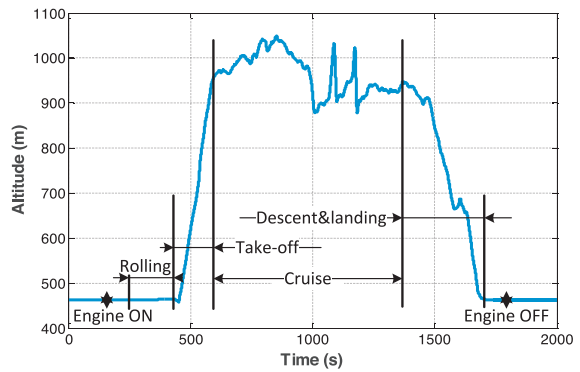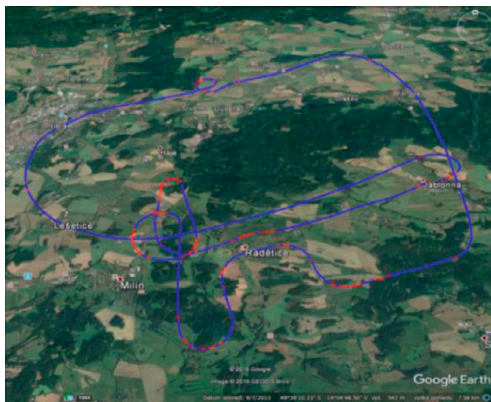

Fig. 12. 2D trajectory of the flight performed – referential data obtained with RTKlib 2.4.2 with an indicated status of the GNSS receiver (blue – fix, red - float) (left); an altitude profile of the flight with emphasized stages (right). (For interpretation of figures in color, the reader is referred to the web version of this article.)
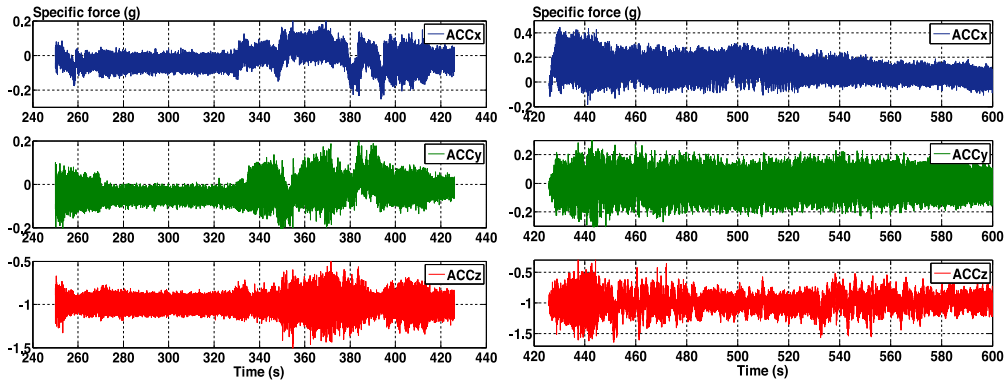
47

Fig. 13. Specific force progressions measured in a body frame of the aircraft during a rolling stage (left) and take-off (right).
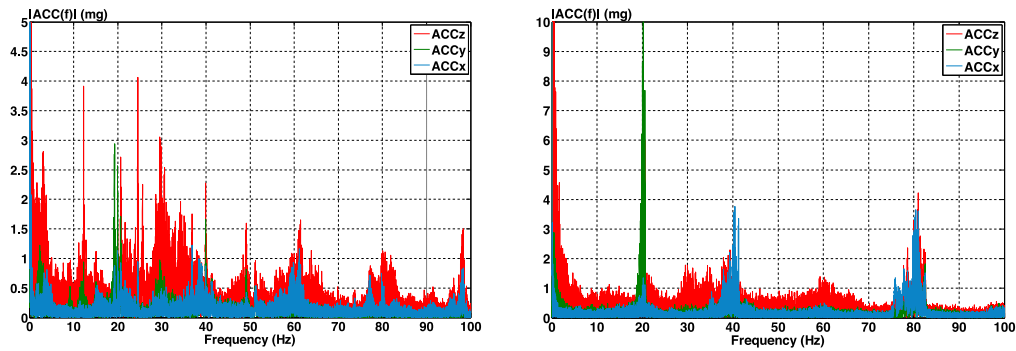

Fig. 14. An amplitude spectrum of the measured specific forces along longitudinal (x), lateral (y), vertical-down (z) axes during a rolling stage (left) and take-off (right).
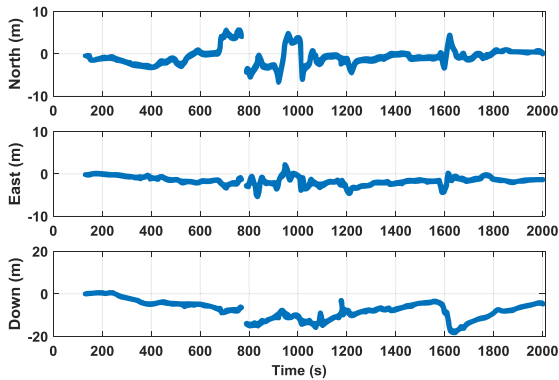

Fig. 15. Deviation between position in NED frame between single point GNSS and RTK-GNSS based evaluation.

igation, i.e. PVA, were estimated in addition to ACC and GYR bias. Before studying the robustness of the proposed navigation solution with respect to GNSS outages it is important to show how these solutions work under ideal conditions, i.e. when GNSS based position is available all the time with a specified update rate, here it is 5 Hz. Fig. 16 depicts progressions of the position (left) and velocity (right) obtained from all available sources supplemented by the three studied approaches. As depicted all progressions are very close to each other, the plots do not show any meaningful deviation via a low resolution, thus a corresponding deviation plot is shown in (Fig. 17). In Fig. 18 there are shown progressions of estimated attitude for the entire flight and additionally for periods

of interest presenting zoomed-in views to see differences in more details. The zoomed view of Fig. 18 (right) shows the advantage of usage ACC based compensation to decrease the effect of free integration of angular rates in the ϕ progression. This time slot of interest corresponds to the situation when the aircraft was descending and landing. Nevertheless, in θ channel this kind of compensation would make a big error in pitch angle during the take-off phase as indicated. Clearly, studied navigation solutions according to mentioned phenomena are fusing ACC based attitude with a calculated one from angular rates by free integration correctly since they are insensitive to potential errors during take-off but still taking ACC based attitude into account which is confirmed by a correct behavior in ϕ channel when the aircraft is steady after landing. From the ψ channel it can be seen how initial information about the heading is treated. It is important to mention that the heading estimation increases its accuracy with the velocity and thus the presented approaches take heading evaluated from GNSS velocity into account only when the horizontal GNSS based velocity overcomes 3 m/s. Cyan doted "rain" indicates when the velocity is under 3 m/s and is not sufficiently accurate for heading evaluation, since it is not reliable as shown in Fig. 18.

ACC and gyro bias progressions are shown in Fig. 19. In these cases, there is no reference value so it is hard to say which progression is correct. Nevertheless, the fluctuation of the bias estimates is a matter of driving noise values set in the matrix Q in the case of EKF and in the case of NLO it is a matter of tuning parameters such as Γ and k_I in addition to the Q matrix values.

The final position estimation was compared with the RTK-GNSS and the root mean square error (RMSE) is summarized in Table 2. The difference among the three presented methods is seen to be small, based on the summarized performance presented in Table 2.

48
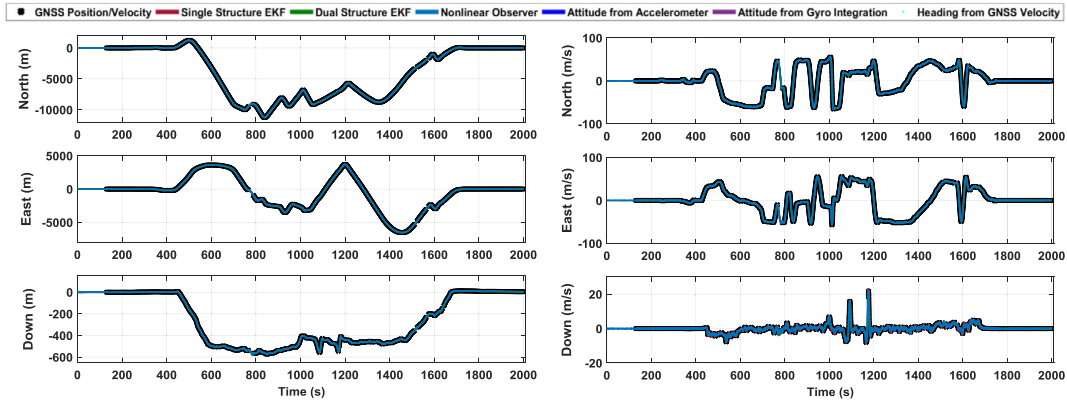
Fig. 16. The whole flight progressions of position (left) and velocity (right) estimation.
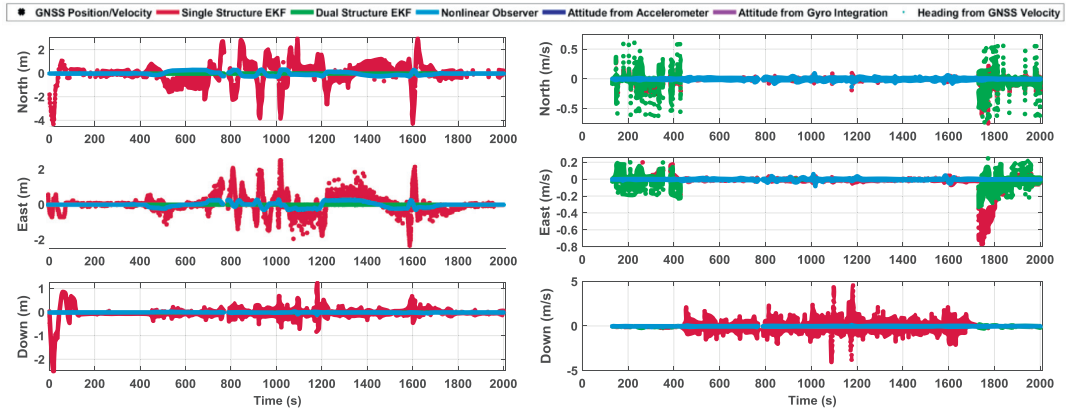
Fig. 17. Deviation plot of estimated and GNNS based position (left) and velocity (right).
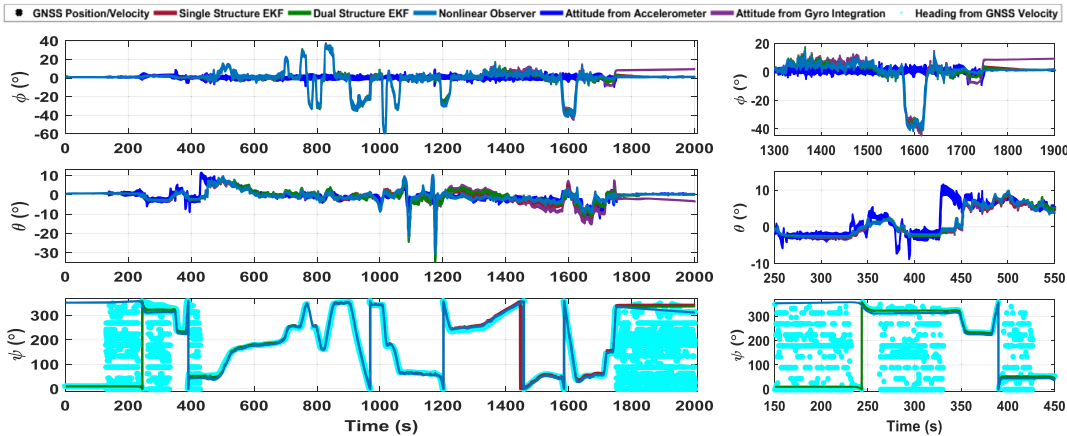
Fig. 18. Attitude estimation – the whole flight progressions (left), zoomed-in parts of interest (right).

Table 2
Resultant RMSE values for NED position estimates with respect to RTK-GNSS estimates (S-EKF – Single Structure EKF; D-EKF – Dual Structure EKF; NLO – Nonlinear Observer) green and red indicate the best and worst results.

RMSE in position without GNSS outage – direction North, East, Down, and 3D											
North (m)			East (m)			Down (m)			3D (m)		
S-EKF	D-EKF	NLO	S-EKF	D-EKF	NLO	S-EKF	D-EKF	NLO	S-EKF	D-EKF	NLO
2.42	1.99	2.02	1.83	1.75	1.73	8.25	8.24	8.25	8.80	8.65	8.67

49
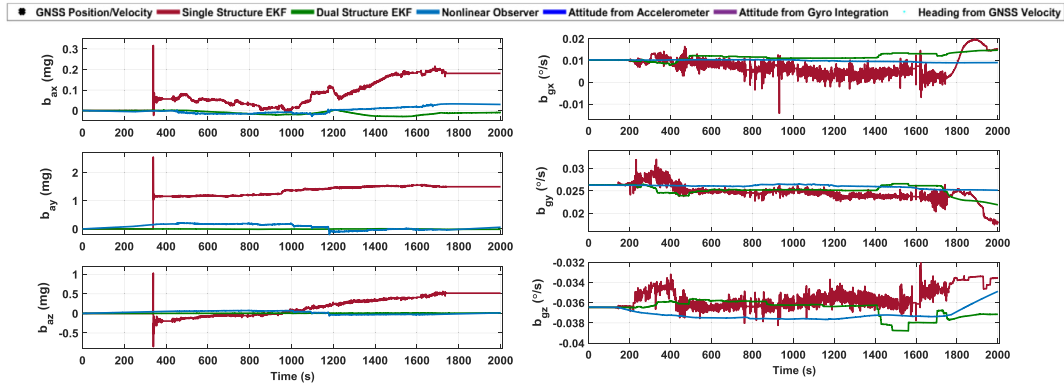
Fig. 19. Accelerometer bias (left) and gyro bias (right) in all 3 body axes.

Fig. 20. Position progressions with GNSS outages marked by red circles. (For interpretation of figures in color, the reader is referred to the web version of this article.)

4.3. Sensitivity analysis under GNSS outage conditions

For the sensitivity analysis of the studied estimation approaches when GNSS data are unavailable via GNSS signal outage we have used artificially induced outages by switching the GNSS data off. In those instances, here calling slots, the GNSS data are used as reference for comparison. The GNSS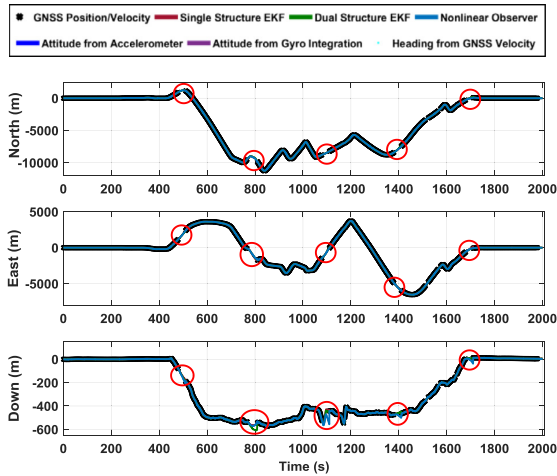 data were artificially turned off for 30 s in each 5 min interval; except the first one which was left for initialization of estimating process. To ascertain the effect of outages for all flight conditions presented by the experimental data, the slots with outages were shifted about 30 s through the

entire 5 min intervals. This leads to 10 series of intervals (INT) for analyzing. For example, the NED position progression for the whole flight data for one outage case (1 INT) is depicted in Fig. 20 where GNSS off slots are indicated by a red circle.

In order to quantify the results of the estimation during the GNSS outages, RMSE was calculated with respect to the absolute GPS position and velocity. Resultant RSME values in position are summarized in Table 3 and velocity in Table 4. The performance of the three proposed methods is seen to be similar, where one method might prevail during one outage interval it might suffer more in another interval, that fact leaves the overall performances similar. The difference among which intervals are handled best for a given method seems to rely more on tuning than on the fundamental algorithms of the proposed methods.

To see individual progressions in few chosen slots, please see Fig. 21 for heading, Fig. 22 for position, and Fig. 23 for velocity progressions. The other flight progressions were very similar to those already shown in Fig. 16 (right) to Fig. 18. The ACC and GYR bias in all studied approaches is frozen during GNSS outage, so the progressions shown in Fig. 19 suffered from a constant value during the outage.

Accuracy in heading estimation is generally crucial in navigation systems since it consequently determines the accuracy in horizontal plane position by resolving North and East component of the position/velocity evaluated in the body frame. According to Figs. 18 and 21 it can be seen that the estimated heading by the presented navigation solutions differs relating to the heading evaluated from GNSS velocities, see (18). First of all it needs to be mentioned that GNSS based heading is insensitive to a real heading fluctuation in the magnitude of up to about 1°. This fluctuation can be observed when GNSS based heading compensation is not strong and thus allows long-term error compensation, however does not affect dynamic changes in heading from gyro outputs. Other impact on differences in heading can be caused by the wind effect producing a side-slip angle. This effect complies
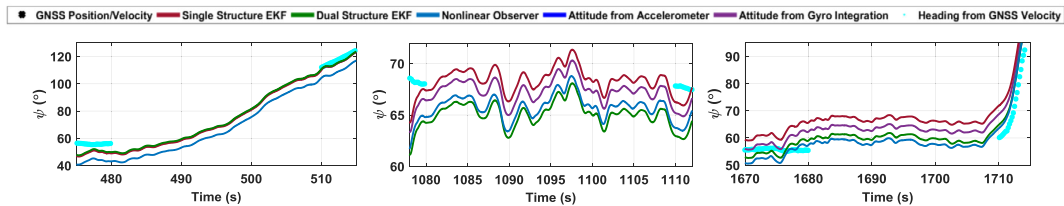

Fig. 21. Zoomed-in heading progressions during GNSS outages.

50

Table 3
Resultant RMSE values for NED position estimates during GNSS outages (S-EKF – Single Structure EKF; D-EKF – Dual Structure EKF; NLO – Nonlinear Observer) green and red indicate the best and worst results.

	RMSE in position – direction North, East, Down, and 3D											
INT	North (m)			East (m)			Down (m)			3D (m)		
	S-EKF	D-EKF	NLO	S-EKF	D-EKF	NLO	S-EKF	D-EKF	NLO	S-EKF	D-EKF	NLO
1	8.2	12.8	9.5	22.9	17.6	8.4	5.5	6.7	5.4	33.7	28.0	16.8
2	20.1	10.0	7.7	14.4	14.0	5.1	5.0	4.7	10.8	32.9	25.9	15.8
3	22.7	11.1	9.8	22.6	14.8	7.9	7.1	3.8	11.3	38.4	28.5	19.7
4	13.8	4.2	6.6	13.4	9.8	4.1	2.8	6.7	19.8	27.5	15.6	25.2
5	7.6	5.9	14.3	16.1	13.3	4.6	3.9	7.8	16.7	21.4	18.5	26.7
6	12	5.5	13.4	21.6	8.4	15.5	3.8	3.9	14.8	28.4	15.2	39.8
7	12.5	9.6	12.4	15.8	6.9	7.8	5.7	8.4	24.9	30.5	23.4	40.4
8	12.7	15.0	11.0	56.4	10.2	23.6	5.0	5.4	16.6	31.1	32.5	41.8
9	24.6	41.0	9.3	25.9	22.9	8.4	1.6	3.7	20.6	38.6	59.6	34.2
10	14.9	16.5	16.3	39.6	32.5	10.8	3.8	5.7	57.6	47.4	50.8	65.8

Table 4
Resultant RMSE values for NED velocity estimates during GNSS outages (S-EKF – Single Structure EKF; D-EKF – Dual Structure EKF; NLO – Nonlinear Observer) green and red indicate the best and worst result.

|	RMSE in velocity – direction North, East, Down, and 3D											
INT	North (m)			East (m)			Down (m)			3D (m)		
	S-EKF	D-EKF	NLO	S-EKF	D-EKF	NLO	S-EKF	D-EKF	NLO	S-EKF	D-EKF	NLO
1	0.99	1.20	0.72	1.95	1.53	0.69	0.69	0.69	0.64	2.92	2.56	1.54
2	1.36	0.73	0.81	1.15	1.46	0.47	0.57	0.62	0.93	2.53	2.44	1.49
3	1.86	0.77	0.81	1.85	1.22	0.68	0.66	0.60	1.08	3.35	2.71	1.64
4	1.24	0.85	0.68	1.33	1.25	0.39	0.52	0.52	1.66	2.49	2.48	2.26
5	0.65	0.51	1.34	1.67	0.96	0.72	0.57	0.64	1.46	2.01	1.52	2.22
6	1.13	0.56	1.02	2.04	1.12	1.20	0.57	0.56	1.35	2.68	1.66	3.65
7	1.26	1.08	1.21	1.39	0.87	0.64	0.72	0.82	2.47	2.63	2.33	3.82
8	1.12	1.84	1.00	1.75	1.35	1.48	0.90	0.86	1.78	2.77	4.05	3.26
9	2.36	3.61	0.66	2.74	1.76	0.60	0.50	0.59	1.84	4.02	5.13	2.77
10	1.19	1.79	1.36	3.29	2.89	0.73	0.66	0.90	4.71	3.95	4.32	5.33
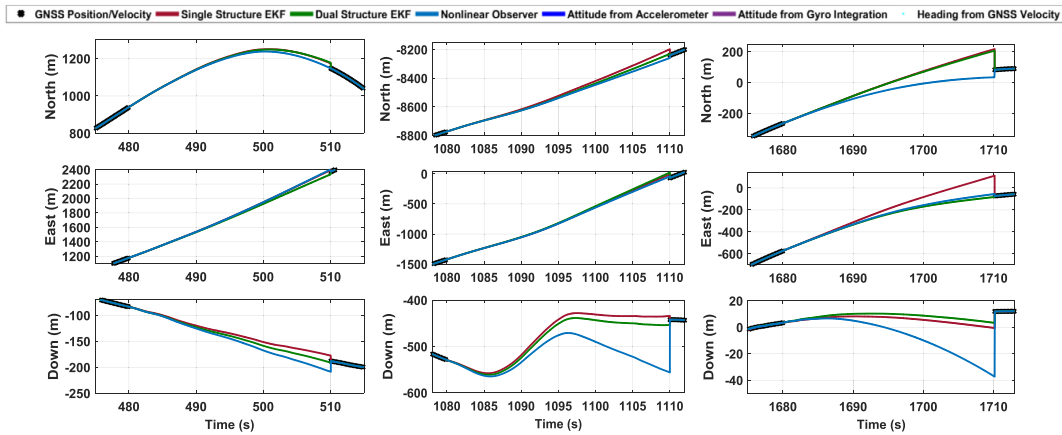
Fig. 22. Zoomed-in position progressions during GNSS outages.

with the difference between heading and the azimuth, where the azimuth is evaluated based on GNSS velocities. The heading and azimuth are equal only when side-slip angle is zero. Deviations seen in Figs. 22 and 23 can have many reasons, e.g. badly estimated heading, badly estimated bias in ACC and/or GYR or side-slip effect making the difference from heading vs azimuth perspectives. When the bias estimates analyzed from progressions shown in Fig. 19 it can be seen they also differ as denoted in Table 5. Since there is no reference, only by position and velocity accuracy reached it can be guessed which progression is more realistic. Moreover, bias instability evaluated by AVAR in Section 3.1 corresponded to a standard deviation of 0.0014°/s for GYR and to 26 µg for ACC. Thus when comparing all these numbers it can be conclude that from the GYR prospective both EKFs seems to be closer
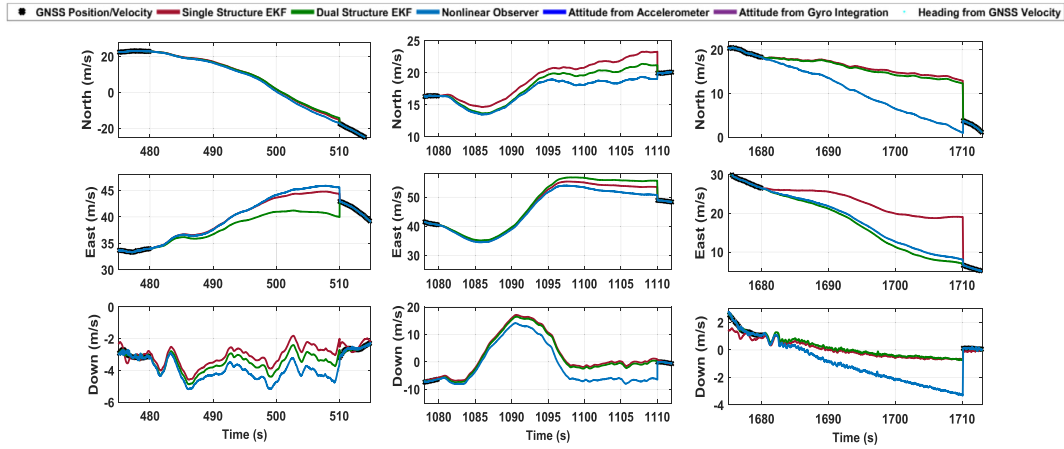
■ GNSS Position/Velocity ━ Single Structure EKF ━ Dual Structure EKF ━ Nonlinear Observer ━ Attitude from Accelerometer ━ Attitude from Gyro Integration · Heading from GNSS Velocity

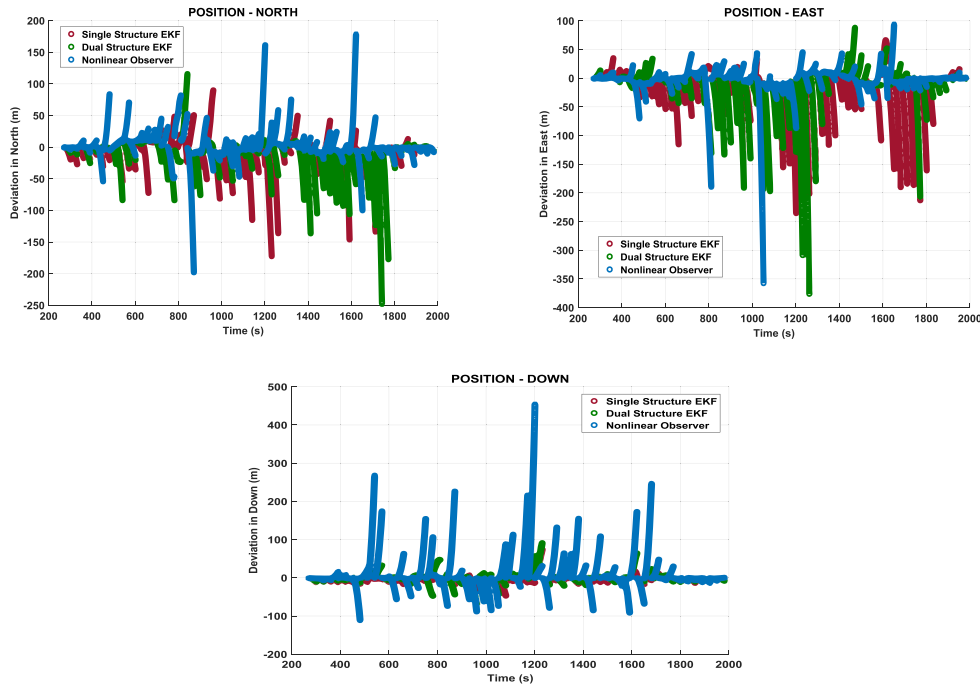**Fig. 23.** Zoomed-in velocity progressions during GNSS outages.

Fig. 24. Summarized deviation plots for the position estimation during the GNSS outage; all 10 series of INT put together.

Table 5
Standard deviation values of estimated bias from Fig. 19.

Approaches	ACC Bias (μg)			GYR Bias (deg/s)		
	b_{a_x}	b_{a_y}	b_{a_z}	b_{g_x}	b_{g_y}	b_{g_z}
S-EKF	66.5	146	237	0.0041	0.0018	0.0014
D-EKF	9.23	5.22	3.23	0.0015	0.0011	0.0008
NLO	16.8	94.3	39.2	0.0005	0.0004	0.0006

to reality; however, in the case of ACC bias the NLO seems to perform better. Nevertheless, as it was mentioned earlier, this kind of behavior is a matter of tuning and adaptation of fusion parameters during an operation. For more details about parameters used, please see Appendix A.

Zoomed-in progressions of position estimated by the three presented navigation solutions shown in Fig. 22 corresponding to different slots could be also put all together. The result is depicted in Fig. 24. It demonstrates the deviations within all slots. So even RMSE values denoted in Table 3 provides general understanding about averaged deviation, in Fig. 24 it can be seen that maximal values of the deviation are larger reaching the magnitude of about 250 m in the North, 370 m in the East, and 450 m in the Vertical-Down direction. Nevertheless, the maximal speed within the flight was about 65 m/s, which leads to 1950 m travelled within 30 s time slot of GNSS outage and that makes the maximal error in a horizontal plane about 13% in the North and 19% in the East direction. However, there is a need to consider the fact and the comparison is done with respect to GNSS single point position where the wind can cause the side-slip effect leading to differences between the

heading and azimuth and thus enlarging the gap between GNSS based position and position estimated by the three presented solutions.

5. Conclusions

This paper addresses a cost-effective navigation solution using commercial grade inertial sensors and studies the performance of three approaches to obtain position, velocity, and attitude estimates. The proposed approaches are validated on real flight data under various operational conditions which differ based on flight stage and on availability of aiding measurements, i.e. from a GNSS receiver providing position and velocity. The resultant performance is compared to the reference position obtained by a dual-frequency X91+ GNSS receiver and consecutive RTK based processing. The paper compares two extended Kalman filters in a single and dual structure configuration and a nonlinear observer. Parameters of individual approaches are set according to results of Allan variance analysis performed on inertial sensors' data. Furthermore, the ability of the presented approaches to estimate bias of inertial sensors is studied. Since no referential data is available for bias estimation we artificially switch off GNSS data and observe the solution behavior relying only on a free integration of inertial data excluded by estimated bias. Via this approach we validate bias estimates which are crucial for robust navigation solutions. Even the studied approaches have roughly the same accuracy during GNSS on conditions, i.e. cm-level RMSE, the situation slightly changes during GNSS outage conditions where deviations reach several meters in evaluated RMSE.

Conflicts of interest

The authors declare no conflict of interest.

Acknowledgments

Appendix A

This chapter provides the tuning parameters used in the estimation algorithms.

A.1. Single structure extended Kalman filter

$$R = \mathrm{diag}([\; 0.8^2, 0.8^2, 0.8^2, 0.05^2, 0.05^2, 5.00^2,$$
$$(1 \cdot 10^{-4})^2, (1 \cdot 10^{-4})^2, (1 \cdot 10^{-4})^2, \dots$$
$$deg2rad(5 \cdot 10^{-3})^2, \; deg2rad(5 \cdot 10^{-3})^2, \; deg2rad(5 \cdot 10^{-3})^2].$$

$$Q = \mathrm{diag}([0.1^2, \; 0.1^2, \; 0.1^2, \dots$$
$$0.3^2, \; 0.3^2, \; 0.15^2, \dots$$
$$(50 \cdot 10^{-3})^2, \; (50 \cdot 10^{-3})^2, \; (50 \cdot 10^{-3})^2, \dots$$
$$deg2rad(0.05)^2, \; deg2rad(0.05)^2, \; deg2rad(0.05)^2, \dots$$
$$deg2rad(0.5)^2, \; deg2rad(0.5)^2m \; deg2rad(0.5)^2, \dots$$
$$deg2rad(1.4 \cdot 10^{-3})^2, \; deg2rad(1.4 \cdot 10^{-3})^2,$$
$$deg2rad(1.4 \cdot 10^{-3})^2])$$

A.2. Dual structure extended Kalman filter

Attitude Estimator
Measurement Noise Covariance:
When compensating using accelerometer only:- $R = \mathrm{diag}$ [50 mg, 50 mg, 50 mg];
When compensating using accelerometer and heading from GNSS velocity:

$$R = \mathrm{diag}[\; 50\,mg, \; 50\,mg, \; 50\,mg, \quad 10^\circ \;];$$

Process Noise Covariance: $Q = \mathrm{diag}\; [0.1^\circ, \; 0.1^\circ, \; 0.1^\circ, 1 \cdot 10^{-6\,\circ}/s, \; 1 \cdot 10^{-6\,\circ}/s, 1 \cdot 10^{-6}\;{}^\circ/s]$

Position Estimator
Process Noise Covariance:

$$Q = \mathrm{diag}\;[1\,m, 1\,m, \; 1\,m, \; 5\,m/s, 5\,m/s\;, \; 5\,m/s,$$
$$50 \cdot 10^{-6}\,g, \; 50 \cdot 10^{-6}\,g, \; 50 \cdot 10^{-6}\,g]$$

A.3. Nonlinear observer

$$M_b = 0.0087\,\mathrm{rad}^2/s^2, \; M_w = 0.1\,\mathrm{m}^2/s^4$$
$$M_f = 0.001, \; \Gamma = \mathrm{diag}([1, 1, 10, 0.1]) \cdot 10^{-6},$$
$$k_1 = 0.2, \quad k_2 = 0.002, \quad k_I = 0.001$$
$$R = \mathrm{diag}([0.08^2 I_3, 0.2^2, 0.08^2, 0.4^2])$$
$$Q = \mathrm{diag}([0.3^2 I_3, 0.5^2 I_3, \left(50 \cdot 10^{-3}\right)^2 \cdot 9.818\, I_3])$$

References

Alam, M., & Rohac, J. (2015). Adaptive data filtering of inertial sensors with variable bandwidth. *Sensors, 15*(2), 3282–3298.

Alam, M., Moreno, G., Sipos, M., & Rohac, J. (2016). INS/GNSS localization using 15 state extended kalman filter. In *International conference in aerospace for young scientists* (pp. 425–435). Beijing: Beijing University of Aeronautics and Astronautics.

Alam, M., Sipos, M., Rohac, J., & Simanek, J. (2015). Calibration of a multi-sensor inertial measurement unit with modified sensor frame. In *IEEE international conference on industrial technology (ICIT)* (pp. 1984–1989). Sevilla, Spain: IEEE.

Allan, D. (1966). Statistics of atomic frequency standards. *Proceedings of the IEEE, 2*(54), 221–230.

Babu, R., & Wang, J. (2009). Ultra-tight GPS/INS/PL integration: A system concept and performance analysis. *GPS Solutions, 13*(1), 75–82.

Bar-Shalom, Y., Li, X., & Kirubarajan, T. (2004). *Estimation with applications to tracking and navigation*. John Wiley & Sons.

Batista, P., Silvestre, C., & Oliveira, P. (2011a). *GES attitude observers – Part I: Multiple general vector observations*. IFAC World Congress.

Batista, P., Silvestre, C., & Oliveira, P. (2011b). *GES attitude observers – Part II: Single vector observations*. IFAC World Congress.

Bristeau, P.-J., & Petit, N. (2011). Navigation system for ground vehicles using temporally interconnected observers. *American control conference*. O'Farrell Street, San Francisco, CA, USA.

Bryne, T. H., Fossen, T. I., & Johansen, T. A. (2014). Nonlinear observer with time–varying gains for inertial navigation aided by satellite reference systems in dynamic positioning. *Mediterranean Conference on Control and Automation*, (June), 1353–1360.

Crassidis, J. L., Markley, F. L., & Cheng, Y. (2007). Survey of nonlinear attitude estimation methods. *Journal of Guidance, Control, and Dynamics, 30*(1), 12–28.

Farrell, J. (2008). *Aided navigation: GPS with high rate sensors*. New York: McGraw Hill Education.

Grewal, M., & Andrews, A. (2001). *Kalman filtering: Theory and practice using MATLAB*. John Wiley&Sons, Inc.

Grip, H. F., Fossen, T. I., Johansen, T. A., & Saberi, A. (2012a). A nonlinear observer for integration of GNSS and IMU measurements with gyro bias estimation. In American control conference, *June* (pp. 4607–4612).

Grip, H. F., Fossen, T. I., Johansen, T. A., & Saberi, A. (2012). Attitude estimation using biased gyro and vector measurements with time-varying reference vectors. *IEEE Transactions on Automatic Control, 57*(5), 1332–1338.

Grip, H. F., Fossen, T. I., Johansen, T. A., & Saberi, A. (2013). Nonlinear observer for GNSS-aided inertial navigation with quaternion-based attitude estimation. *American control conference*.

Grip, H. F., Fossen, T. I., Johansen, T. A., & Saberi, A. (2016). Nonlinear observer for attitude, position and velocity: Theory and experiments. In H. Fourati, & D. C. Belkhia (Eds.), *Multisensor attitude estimation* (pp. 291–314). crc press (taylor & francis group).

Gustafsson, F., Gunnarsson, F., Bergman, N., Forssell, U., Jansson, J., Karlsson, R., et al. (2002). Particle filters for positioning, navigation and tracking. *IEEE Transaction on Signal Processing, 50*, 425–437.

Hamel, T., & Mahony, R. (2006). Attitude estimation on SO(3) based on direct inertial measuremetns. In *Proceedings of IEEE international conference on robotics automation.*

Hansen, J. M., Rohac, J., Sipos, M., Johansen, T. A., & Fossen, T. I. (2016). Validation and experimental testing of observers for robust GNSS-aided inertial navigation. In G. Wang (Ed.), *Recent advances in robotic systems.* Vienna: InTech Open Access http://intechweb.org/.

IEEE Std. 1293. IEEE Standard Specification Format Guide and Test Procedure for Linear, Single-axis, Nongyroscopic Accelerometers. (n.d.). *Technical report, Institute of Electrical and Electronics Engineers.*

IEEE Std. 528. IEEE Standard for Inertial Sensor Terminology. (n.d.). *Technical report, Institute of Electrical and Electronics Engineers.*

IEEE Std. 647. IEEE Standard Specification Format Guide and Test Procedure for SingleAxis Laser Gyros. (n.d.). *Technical report, Institute of Electrical and Electronics Engineers.*

Johansen, T. A., & Fossen, T. I. (2016). The eXogenous Kalman Filter (XKF). *International Journal of Control*, 1–7.

Li, Y., Wang, J., Rizos, C., Mumford, P., & Ding, W. (2006). Low-cost tightly coupled GPS/INS integration based on a nonlinear Kalman filtering design. In *Proceedings of ION national technical meeting* (pp. 18–20).

Mahony, R., Hamel, T., Trumpf, J., & Lageman, C. (2009). Nonlinear attitude observer on SO(3) for complementary and compatible measurements: A theoretical study. *IEEE conference on decision and control.*

Nemra, A., & Aouf, N. (2010). Robust INS/GPS sensor fusion for UAV localization using SDRE nonlinear filtering. *IEEE Sensors Journal, 10*(4), 789–798.

Reinstein, M., & Kubelka, V. (2012). Complementary filtering approach to orientation estimation using inertial sensors only. *IEEE international conference on robotics and automation (ICRA)*, Prague, Czech Republic.

Rezaeian, A., Zarringhalam, R., Fallah, S., Melek, W., Khajepour, A., Chen, S.-K., et al. (2013). *Cascaded dual extended Kalman filter for combined vehicle state estimation and parameter identification* Tech. rep., SAE Technical Paper.

Ristic, B., Arulampalam, S., & Gordon, N. (2004). *Beyond the Kalman filter, pertical filters for tracking applications.* Artech House.

Rohac, J., Sipos, M., & Simanek, J. (2015). Calibration of low-cost triaxial inertial sensors. *IEEE Instrumentation & Measurement Magazine, 18*(6), 32–38.

Salcudean, S. (1991). A globally convergent angular velocity observer for rigid body motion. *IEEE Transactions on Automatic Control, 36*(12), 1493–1497.

Salychev, O. (2004). *Applied inertial navigation: problems and solutions.* Moscow, Russia: BMSTU Press.

Savage, P. G. (1998a). Strapdown inertial navigation integration algorithm design part 1: Attitude algorithms. *Journal of Guidance, Control, and Dynamics, 21*(1), 19–28.

Savage, P. G. (1998b). Strapdown inertial navigation integration algorithm design part 2: Velocity and position algorithms. *Journal of Guidance, Control, and Dynamics, 21*(2), 208–221.

Silicon Sensing. *DMU10 Technical Datasheet.* Retrieved from Silicon Sensing: February 10 http://www.siliconsensing.com/media/30805/dmu10-00-0100-132-rev-6.pdf .

Simanek, J., Reinstein, M., & Kubelka, V. (2014). Evaluation of the EKF-based estimation architectures for data fusion in mobile robots, *20*(2), 985–990.

Simon, D. (2010). Kalman filtering with state constraints: A survey of linear and nonlinear algorithms. *IET Control Theory & Applications, 4*(8), 1303–1318.

Sotak, M., Sopata, M., & Kmec, F. (2006). Navigation systems using Monte Carlo method. *Guidance, Navigation and Control Systems.*

Thienel, J., & Sanner, R. M. (2003). A coupled nonlinear space attitude controller and observer with an unknown constant gyro bias and gyro noise. *IEEE Transactions on Automatic Control, 48*(11), 2011–2015.

Titterton, D., & Weston, J. (2004). *Strapdown inertial navigation technology.* Stevenage, UK: Institution of Engineering and Technology.

Vik, B., & Fossen, T. I. (2001). A nonlinear observer for GPS and INS integration. In *Proc. conference on decision and control.*

Wolf, R., Eissfeller, B., & Hein, G. (1997). A Kalman filter for the integration of a low cost INS and an attitude GPS. In *Proceedings of the international symposium on kinematic systems in geodesy, geomatics and navigation* (pp. 143–150).

Zihajehzadeh, S., Loh, D., Lee, T. J., Hoskinson, R., & Park, E. J. (2015). A cascaded Kalman filter-based GPS/MEMS-IMU integration for sports applications. *Measurement, 73*, 200–210.

Chapter 6

Nonlinear Aircraft Control

6.1 Summary of the contributions

This chapter details about the designing of longitudinal flight controller for a fixed wing aircraft using nonlinear control techniques. Flight control laws are traditionally designed from a set of linearised models, however aircraft are highly nonlinear system. Due to the application of linear control laws on a non-linear system, the real performance ability of the aircraft is not fully utilised. Therefore, this chapter aims at discussing the design of a longitudinal flight controller for a fixed-wing aircraft using non-linear dynamic inversion technique or, in terms of control theory, partial exact feedback linearisation. The novelty in the contribution is in the proposed combination of three different automatic flight controllers that provide complete 3-DOF longitudinal control. The simulation results carried out on a nonlinear aircraft model verified the proposed theoretical results confirming the suitability of the controllers.

6.2 Publication

The work is represented by a publication with modified formatting and follows on the next page.

On the internal stability of non-linear dynamic inversion: application to flight control

Mushfiqul Alam[1] ✉, Sergej Celikovsky[2]

[1]*Department of Measurement, Faculty of Electrical Engineering, Technicka 2, Czech Technical University in Prague, Prague, Czech Republic*
[2]*Institute of Information Theory and Automation, Czech Academy of Sciences, Pod Vodarenskou Vezi 4, CZ-182 08 Prague 8, Czech Republic*
✉ *E-mail: mushfala@fel.cvut.cz*

Abstract: Aircraft are highly non-linear systems, but flight control laws are traditionally designed from a set of linearised models. Due to the application of linear control laws on a non-linear system, the real performance ability of the aircraft is not fully utilised. In addition, in adverse situations like near stall, the aircraft develops significant non-linearities, and linear control laws do not perform well. This study therefore considers the design of a longitudinal flight controller for a fixed-wing aircraft using non-linear dynamic inversion technique or, in terms of control theory, partial exact feedback linearisation. A novel contribution of this study is the proposed combination of three different automatic flight controllers that provide complete 3-DOF longitudinal control. A detailed analysis of the internal dynamics for each controller is also presented. It has been shown that for each controller the internal dynamics are stable. This makes the controller suitable for various flight conditions. The aims of these flight controllers are threefold. First, to provide control of the flight path angle by tracking the pitch angle and the angle of attack. Second, to provide high attitude (pitch up or down) manoeuvrability. Finally, to provide automatic adverse attitude recovery of the aircraft in situations like stall, the switching strategy between the controllers are also discussed. A simulation carried out on a non-linear model of a multi-role fighter aircraft verified the proposed theoretical results confirming the suitability of the controllers.

1 Introduction

The current state-of-the-art automatic flight control system (AFCS) provides efficient methods for pilots to fly the aircraft. The introduction of the fly-by-wire (FBW) system has enabled the aircraft to be stabilised automatically, preventing unsafe operation outside the performance envelope without input from the pilot [1]. However, in the critical conditions, where the aircraft gets outside the flight envelope the automatic flight control known as 'Autopilot' is disengaged, and the pilot is required to take manual corrective actions. An example of critical conditions of this kind is when the aircraft reaches critical angle of attack (or stall angle), beyond which the lift is suddenly reduced. This phenomenon is known as stall [2]. The standard stall recovery procedure (shown in Fig. 1) recommended in the pilot training is to push the control stick down, forcing a nose down motion of the aircraft. This makes the aircraft go faster and restores the required lift [3]. Pilots tend to misread the situation and take wrong corrective measure leading to an accident. A significant number of commercial and military air crash accidents have occurred after loss of control due to stalling caused by pilot error. Indonesia AirAsia Flight 8501, Air France Flight 447, Navy McDonnell-Douglas QF-4S+ Phantom II and United States Air Force Boeing C-17A Lot XII Globemaster III are some recent air accidents caused by pilot error and stall [4–7]. To address this problem, we propose three new different automatic flight controllers that can be used in different phases of flight based on the well-known partial exact feedback linearisation approach within the realm of the non-linear dynamic inversion (NDI) technique.

Flight control laws below the stall angle are designed using linear control design methods such as gain scheduling [1]. The control laws are designed at many flight-operating points [8] and the gain scheduling is chosen as a function of mass, Mach number and altitude. This design procedure requires a great amount of assessment to ensure the adequate stability and performance at off-design points. It is time-consuming and the performance capabilities of the aircraft are not fully realised. As an alternative to gain scheduling robust control algorithms such as $\mathcal{H}_2$ and $\mathcal{H}_\infty$ controllers are proposed [9]. However, at a large angle of attack (near the stall angle) aircraft develop significant non-linearities [10] and for this reason the linearised control laws do no longer hold. An alternative approach is to apply non-linear design techniques in critical flight conditions such as near stall point or high attitude angle (pitch angle) manoeuvres where the aircraft develops non-linearities. NDI directly make use of the non-linear structure of the aircraft model. It uses dynamic models and state feedback to globally linearise dynamics of selected controlled variables by cancelling the non-linearities in the dynamic model. As a result, the NDI method is capable of handling large non-linearities. NDI control law is designed to globally reduce the dynamics of selected controlled variables to integrators. A closed loop system is then designed to make the control variables exhibit specified command responses satisfying the flight-handling qualities and various physical limitation of the aircraft control actuators. Flight control design using NDI was first proposed in the
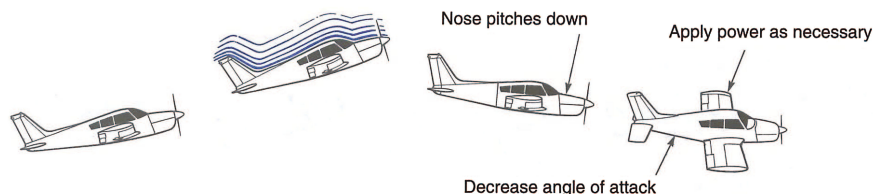

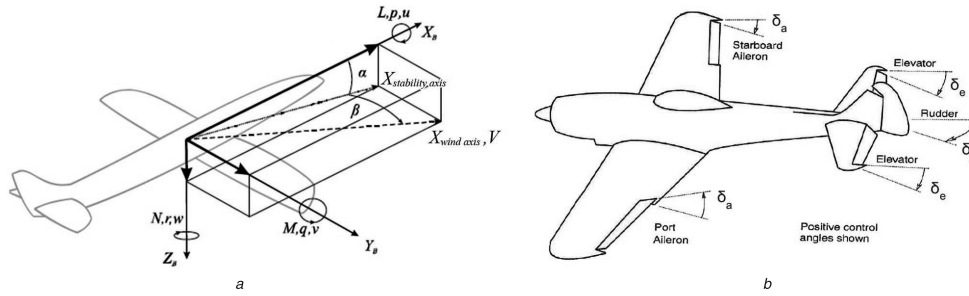**Fig. 1** *Stall recovery procedure*

Fig. 2 *Description of the aircraft system: V, flight path velocity; α, angle of attack; β, side-slip angle; φ, θ, ψ, Euler's angles; δe, δa, δr, control surface deflections; F_T, engine thrust; p, q, r, angular rates; $I_{xx}, I_{yy}, I_{zz}, I_{xz}$, moments of inertia; L, M, N, aerodynamic moments; X_B, Y_B, Z_B, body forces*

late 1970s [11, 12]. Since that time, a number of research efforts have been made to use non-linear control techniques for flight controls, e.g. as incremental NDI [13, 14], adaptive fuzzy sliding control [15, 16]. Various methods for analysing the robustness of the NDI flight controllers for a quasi-linear-parameter varying model were presented in [17, 18]. Stochastic robust non-linear control using control logic for a high incidence research concept aircraft is proposed in [19]. However, this work did not take the internal dynamics into account, and stability was limited to manual pilot inputs.

NDI is widely used for under-actuated mechanical systems [20]. Since the longitudinal dynamics of the aircraft is under-actuated, it is not possible to control all the states using a single controller. The novel approach presented here is a proposal for three different controllers corresponding to the output sets, which are angle of attack and pitch angle; velocity and pitch angle; finally, velocity and angle of attack. The first controller can be used for high pitch angle control for conditions like take-off while retaining control over the angle of attack. The second controller can be used as the pitch autopilot with control over the velocity. Finally, the third controller can be used for stall recovery of the aircraft at the same time preventing dangerous speed. A complete analysis of the internal dynamics for each controller is provided. The switching strategies between these three controllers are discussed. This approach with the use of NDI takes into account all significant non-linearities in the system utilising full performance capability of the aircraft. An original feature in this paper is the designing of the three flight controllers with a detailed outline of the stability of the internal dynamics.

This paper is organised as follows: Section 2 presents the dynamic model of the aircraft. Main results are given in Sections 3 and 4. Namely, Section 3 presents the detailed design of the control laws. Section 4 provides a detailed analysis of the simulation results. Section 5 contains the final concluding remarks.

2 Dynamic modeling

The aircraft configuration is illustrated in Fig. 2. For a conventional fixed-wing aircraft, the aerodynamic control surfaces that produce the moments are the horizontal tail (elevator), the ailerons and the vertical tail (rudder). Only two orientation angles relative to the wind, known as aerodynamic angles are needed to specify the aerodynamic forces and moments (angle of attack (α) and the side-slip angle (β)) acting on the aircraft [10].

2.1 Longitudinal aerodynamics

The aerodynamic forces (drag and lift) and the moment (pitching moment) acting on the aircraft are defined in terms of the non-dimensional aerodynamic coefficients ($C_{L_{Total}}$, $C_{D_{Total}}$, $C_{m_{Total}}$) are calculated as follows:

$$X_B = \frac{1}{2}\rho V^2 S C_{D_{Total}}$$
$$M = \frac{1}{2}\rho V^2 S c_{MAC} C_{m_{Total}} \quad (1)$$
$$Z_B = \frac{1}{2}\rho V^2 S C_{L_{Total}}$$

Here ρ denotes the air density, S denotes the aircraft's effective wing surface area, and c_{MAC} denotes the mean aerodynamic chord. The aerodynamic coefficients are specified as functions of aerodynamic angles, control surface deflections and the aerodynamic derivatives. Each component of the aerodynamic and moment coefficients is represented by a 'look up' table.

$$C_{L_{Total}} = C_{L_o} + C_{L_\alpha}\alpha + C_{L_q}q\frac{c_{MAC}}{2V} + C_{L_{\delta e}}\delta e$$
$$= C_L + C_{L_q}q\frac{c_{MAC}}{2V} + C_{L_{\delta e}}\delta e. \quad (2)$$

$$C_{D_{Total}} = C_{D_0} + C_{D_\alpha}\alpha^2 + C_{D_{\delta e}}\delta e$$
$$= C_D + C_{D_{\delta e}}\delta e; \quad C_D \simeq C_{D_0} + |C_{D_\alpha}\alpha^2|. \quad (3)$$

$$C_{m_{Total}} = C_{m_0} + C_{m_\alpha}\alpha + C_{m_q}q\frac{c_{MAC}}{2V} + C_{m_{\delta e}}\delta e$$
$$= C_m + C_{m_q}q\frac{c_{MAC}}{2V} + C_{m_{\delta e}}\delta e. \quad (4)$$

Here, subscripts stand for the aerodynamic derivative of the respective variables. The aerodynamic coefficients C_L, C_D and C_m are related to the lift, drag, and pitching moments produced by the main wing and are functions of angle of attack (α).

2.2 Rigid body equation of motion for the aircraft

The aerodynamic force and the moment models are combined with the vector equations of motion to obtain the aircraft dynamic motion model. The stability and the wind axes are treated as being fixed to frames that are rotating relative to the vehicle-body frame [10]. Combined with wind and body axes the total 3-DOF longitudinal dynamic motion of the aircraft is written as follows:

Force equations:

$$\dot{V} = -\frac{X_B}{m} + \frac{F_T}{m}\cos\alpha\cos\beta$$
$$+ g(\cos\phi\cos\theta\sin\alpha\cos\beta + \sin\phi\cos\theta\sin\beta - \sin\theta\cos\alpha\cos\beta). \quad (5)$$

$$\dot{\alpha} = -\frac{Z_B}{mV\cos\beta} + q - \tan\beta(p\cos\alpha + r\sin\alpha)$$
$$- \frac{F_T\sin\alpha}{mV\cos\beta} + \frac{g}{V\cos\beta}(\cos\phi\cos\theta\cos\alpha + \sin\theta\sin\alpha). \quad (6)$$

Moment equation:

$$\dot{q} = \frac{(I_{zz} - I_{xx})}{I_{yy}} pr - \frac{I_{xz}}{I_{yy}}(p^2 - r^2) + \frac{M}{I_{yy}}. \quad (7)$$

Kinematic equation:

$$\dot{\theta} = q\cos\phi - r\sin\phi . \quad (8)$$

Assuming that the lateral-directional motion of the aircraft is independently and separately controlled bringing the aircraft to a wing-level flight condition the 3-DOF longitudinal model of the aircraft motion can be further simplified. The side-slip and roll angles are associated with the lateral dynamics, so it can be assumed that the roll angle (ϕ) and the side-slip angle (β) is zero. The 3-DOF longitudinal dynamics equation (5)–(8) get:

$$\dot{V} = -\frac{1}{2}\frac{\rho S}{m}(C_{D_0} + C_{D_\alpha}\alpha)V^2$$
$$-\frac{1}{2}\frac{\rho S}{m}C_{D_{\delta e}}(\alpha)V^2\delta e + \frac{F_T\cos(\alpha)}{m} + g\sin(\alpha - \theta) . \quad (9)$$

$$\dot{\alpha} = -\frac{1}{2}\frac{\rho S}{m}(C_{L_o} + C_{L_\alpha}\alpha)V - \frac{1}{2}\frac{\rho S}{m}c_{MAC}C_{L_q}q - \frac{1}{2}\frac{\rho S}{m}C_{L_{\delta e}}V\delta e$$
$$-\frac{\sin(\alpha)F_T}{mV} + q + \frac{g\cos(\alpha - \theta)}{V} . \quad (10)$$

$$\dot{q} = \frac{1}{2}\frac{\rho S}{I_{yy}}c_{MAC}(C_{m_0} + C_{m_\alpha}\alpha)V^2 + \frac{1}{4}\frac{\rho S}{I_{yy}}c_{MAC}^2 C_{m_q}Vq$$
$$+\frac{1}{2}\frac{\rho S}{I_{yy}}c_{MAC}V^2 C_{m_{\delta e}}\delta e . \quad (11)$$

$$\dot{\theta} = q . \quad (12)$$

3 Control law design

As has already been noted, we will study the case of simplified non-linear dynamics, namely the longitudinal model (9)–(12). This model has four state variables and two control inputs. First, let's put the equations into the standard state-space model form known in non-linear control theory [20]. Now, if we define the state variables as $[x_1, x_2, x_3, x_4]^T = [V, \alpha, q, \theta]^T$, and the control inputs as $[u_1, u_2]^T = [\delta e, F_T]^T$, then the system in (9–12) can be written in the following form: (see (13))

Here, $x \in \mathbb{R}^4$, $u \in \mathbb{R}^2$, $f(x) = (f_i(x)) \in \mathbb{R}^4$, and $g(x) = (g_{ij}(x)) \in \mathbb{R}^{4\times2}$, where $i = 1,2,3,4$ and $j = 1,2$. Furthermore, lets denote $g^j = [g_{1j}, g_{2j}, g_{3j}, g_{4j}]^T$, $j = 1,2$, and $b_1 = -\frac{\rho S}{2m}$; $b_2 = b_1 C_{D_{\delta e}}$; $b_5 = C_{L_0}$; $b_6 = b_1 c_{MAC}C_{L_q}$; $b_7 = b_1 C_{L_{\delta e}}$; $b_8 = \frac{\rho S}{2I_{yy}}c_{MAC}$; $b_9 = b_8 c_{MAC}C_{m_q}$; $b_{10} = b_8 C_{m_{\delta e}}$; $b_3 = \frac{1}{m}$; $b_4 = g$; $b_{11} = C_{D_0}$; $b_{12} = C_{D_\alpha}$; $b_{13} = C_{L_\alpha}$; $b_{14} = C_{m_0}$; $b_{15} = C_{m_\alpha}$. Moreover, $C_{L_{\delta e}}, C_{L_q}, C_{L_\alpha}, C_{D_0} > 0$ and $C_{m_q}, C_{m_{\delta e}}, C_{m_\alpha} < 0$. Thus the variables $b_1, b_2, b_6, b_7, b_9, b_{10} < 0$ and $b_3, b_4, b_5, b_8, b_{11}, b_{13} > 0$.

To compute partial exact feedback linearisation of (13), the notion of the so-called auxiliary/virtual output is used. Namely, by defining a suitable output functions $h(x) = [h_1(x), h_2(x)]^T$, $x \in \mathbb{R}^4$ we can compute the input–output linearisation transforming certain sub-systems to linear form. To proceed with, $h(x)$ is said to have

vector relative degree $r = (r^1, r^2)$ around some equilibrium working point $x_o \in \mathbb{R}^4$ if r^1, r^2 is the integers such that there exists neighbourhood of x_o denoted as N_{x_o}, it holds:

$$\mathscr{L}_{g^j}\mathscr{L}_f^l h_k(x) \equiv 0, \quad x \in N_{x_o}, \quad k, j = 1,2, \quad l = 0, ..., r^{k-2} \quad (14)$$

$$\text{rank}\left[\mathscr{L}_{g^j}\mathscr{L}_f^{(r^k - 1)}h_k(x_o)\right] = 2, \quad k, j = 1,2. \quad (15)$$

Here, $\mathscr{L}_f^m$, $m = 0, 1, ...$, stands for the so-called Lie derivatives and their iterations [20]. More precisely:

$$\mathscr{L}_f h = \nabla h f, \quad \nabla h = \frac{\partial h}{\partial x},$$

$$\mathscr{L}_f^o h = h, \quad \mathscr{L}_f^m h = \mathscr{L}_f\left(\mathscr{L}_f^{m-1}h\right) = \nabla\left(\mathscr{L}_f^{m-1}h\right)f, \quad m = 1, 2, 3, ...$$

It is well-known [20] that the n-dimensional system with vector relative degree $r = (r^1, r^2) \geq 1$ has $(r^1 + r^2)$-dimensional exact feedback linearisable part has $n - (r^1 + r^2)$ residual non-linear part. The residual part of the system dynamics is called 'internal dynamics'. It is important to ensure that the internal dynamics of the residual part or state that is left uncontrolled is stable. The autonomous part which keeps the selected output zero is referred to as the zero-dynamics. In the following sections, we will present three different selections of pairs of outputs giving three different partial linearisations (three different controllers) and their internal dynamics analysis.

3.1 Flight controller for angle of attack and pitch angle (flight controller no. 1)

This flight controller is to be used for situations like take-off where the primary focus is on lifting the aircraft with a desired pitch angle ($\theta = x_4$) at a certain take-off speed and to have a control over the angle of attack ($\alpha = x_2$), so that the aircraft has enough lift to get off the ground without stalling. Following (13) the relation between the pitch rate ($q = x_3$) and the pitch angle ($\theta = x_4$) is a single integrator, so x_4 can be tracked jointly with x_3.

3.1.1 Control design.: The control objective for this controller is to design a tracking controller for x_2 and x_4 while stabilising the x_3. Thus the auxiliary outputs chosen to get the partial exact feedback linearisation for Flight Controller No. 1, denoted as $h^1(x)$ are as follows:

$$h^1(x) = \begin{bmatrix} x_2 \\ x_4 \end{bmatrix}.$$

Let the virtual inputs to stabilise $\dot{x}_3$ be v_1 and to control $\dot{x}_2$ be v_2. Lie derivative computation of $h^1(x)$ following (14) and (15) show that it has relative degrees $r = (1,2)$. This allows us to obtain the feedback linearised form of the system (13) as

$$\dot{x}_2 = v_2,$$
$$\dot{x}_3 = v_1,$$
$$\dot{x}_4 = x_3 .$$

$$\begin{bmatrix} \dot{x}_1 \\ \dot{x}_2 \\ \dot{x}_3 \\ \dot{x}_4 \end{bmatrix} = \begin{bmatrix} b_1 b_{11}x_1^2 + b_1 b_{12}x_2 x_1^2 + b_4\sin(x_2 - x_4) \\ b_1 b_5 x_1 + b_1 b_{13}x_2 x_1 + b_6 x_3 + x_3 + b_4 x_1^{-1}\cos(x_2 - x_4) \\ b_8 b_{14}x_1^2 + b_8 b_{15}x_2 x_1^2 + b_9 x_1 x_3 \\ x_3 \end{bmatrix} + \begin{bmatrix} b_2 x_1^2 & b_3\cos(x_2) \\ b_7 x_1 & -b_3 x_1^{-1}\sin(x_2) \\ b_{10}x_1^2 & 0 \\ 0 & 0 \end{bmatrix}\begin{bmatrix} u_1 \\ u_2 \end{bmatrix}. \quad (13)$$

Now the virtual inputs v_1 and v_2 are defined as follows:

$$\begin{bmatrix} v_1 \\ v_2 \end{bmatrix} = \begin{bmatrix} f_3 \\ f_2 \end{bmatrix} + \begin{bmatrix} g_{31} & 0 \\ g_{21} & g_{22} \end{bmatrix} \begin{bmatrix} u_1 \\ u_2 \end{bmatrix}. \tag{16}$$

The conditions for the existence of the relative degree as mentioned in (14) and (15) hold if and only if $x_1 \neq 0$ and $x_2 \neq l\pi, l$ is an integer. This does not limit the applicability of the designed controller as x_1 is the velocity and x_2 is the angle of attack while lifting the aircraft which always occurs with non-zero angle of attack. Following (16) the input equations for u_1 and u_2 can be rewritten as follows:

$$\begin{bmatrix} u_1 \\ u_2 \end{bmatrix} = \begin{bmatrix} g_{31} & 0 \\ g_{21} & g_{22} \end{bmatrix}^{-1} \left[-\begin{bmatrix} f_3 \\ f_2 \end{bmatrix} + \begin{bmatrix} v_1 \\ v_2 \end{bmatrix} \right],$$

$$u_1 = \frac{-(b_8 b_{14} x_1^2 + b_8 b_{15} x_2 x_1^2 + b_9 x_1 x_3) + v_1}{b_{10} x_1^2}. \tag{17}$$

$$u_2 = \frac{-(b_1 b_5 x_1 + b_1 b_{13} x_2 x_1 + b_6 x_3 + x_3 + b_4 x_1^{-1} \cos(x_2 - x_4)) b_{10} x_1^2}{(b_{10} x_1^2)(-b_3 x_1^{-1} \sin x_2)} +$$
$$+ \frac{(b_8 b_{14} x_1^2 + b_8 b_{15} x_2 x_1^2 + b_9 x_1 x_3) b_7 x_1}{(b_{10} x_1^2)(-b_3 x_1^{-1} \sin x_2)} + \frac{-b_7 x_1 v_1 + b_{10} x_1^2 v_2}{(b_{10} x_1^2)(-b_3 x_1^{-1} \sin x_2)}. \tag{18}$$

Further, consider the subsystem involving x_3, x_4 and the virtual input v_1. This is a system with a double integrator relationship. To track some reference $x_3^{\mathrm{ref}}(t)$, $x_4^{\mathrm{ref}}(t)$, have in mind that it should hold $x_3^{\mathrm{ref}} = \dot{x}_4^{\mathrm{ref}}$. Now to track the references, let us define the tracking error as follows:

$$e_3 = x_3 - \dot{x}_4^{\mathrm{ref}}, \quad \dot{e}_3 = \dot{x}_3 - \ddot{x}_4^{\mathrm{ref}}, \tag{19}$$

$$e_4 = x_4 - x_4^{\mathrm{ref}}, \quad \dot{e}_4 = \dot{x}_4 - \dot{x}_4^{\mathrm{ref}} = e_3. \tag{20}$$

The feedback tracking controller equation for x_3 can be written as

$$\dot{x}_3 = v_1 = \ddot{x}_4^{\mathrm{ref}} + k_3\left(x_3 - \dot{x}_4^{\mathrm{ref}}\right) + k_4\left(x_4 - x_4^{\mathrm{ref}}\right). \tag{21}$$

Here k_3 and k_4 are the feedback control gains. Using (19)–(21) we get:

$$\dot{e}_3 = k_3 e_3 + k_4 e_4; \quad \dot{e}_4 = e_3. \tag{22}$$

Therefore, choosing $k_3 < 0$ and $k_4 < 0$, we gets $e_3 \to 0$ and $e_4 \to 0$ exponentially, which means that exponential tracking is achievable.

Consider the subsystem involving x_2 and the virtual input v_2. This system is directly related as a single integrator. We assume $x_2^{\mathrm{ref}}(t)$ is to be tracked and we define tracking error e_2 as

$$e_2 = x_2 - x_2^{\mathrm{ref}}, \quad \dot{e}_2 = \dot{x}_2 - \dot{x}_2^{\mathrm{ref}}. \tag{23}$$

The feedback tracking controller for x_2 can be written in the form:

$$\dot{x}_2 = v_2 = \dot{x}_2^{\mathrm{ref}} + k_2\left(x_2 - x_2^{\mathrm{ref}}\right). \tag{24}$$

Here k_2 is the feedback tracking control gain. Now, combining (23) and (24) gives

$$\dot{e}_2 = k_2 e_2.$$

By choosing $k_2 < 0$, $e_2 \to 0$, hence exponential tracking is possible for the reference angle of attack x_2^{ref}. Substituting (21) and (24) into (17) and (18) gives the complete closed form expression for u_1 and u_2 as (see (25))
(see (26))

Combining the two controllers enables us to control both the pitch angle x_4 and the angle of attack x_2, provided that the corresponding internal non-linear residual dynamics of the velocity x_1 has favourable properties.

3.1.2 Internal dynamics of the velocity (x_1).: During the design of the controller the velocity x_1 is left uncontrolled. This corresponds to the hidden uncontrolled internal dynamics. It is essential to check and ensure that the internal dynamics of the velocity is stable. To check the stability of the internal dynamics, substitute the expression of control input u_1 and u_2 (25) and (26) into the equation of $\dot{x}_1$ in (13). For simplicity zero-dynamics are studied, hence for reference tracking $x_2^{\mathrm{ref}}(t)$, $x_4^{\mathrm{ref}}(t)$, $x_3^{\mathrm{ref}}(t)$ the virtual inputs $v_1 = v_2 = 0$. For the purposes of the analysis constant reference tracking is considered. This means $x_2^{\mathrm{ref}} \equiv x_2^e$, $x_4^{\mathrm{ref}} \equiv x_4^e$, $\dot{x}_3^{\mathrm{ref}} \equiv 0$, here x_2^e and x_4^e are constant and therefore we have to analyze stability of the equilibrium of the one dimensional velocity internal dynamics given by

$$\dot{x}_1 = \bar{f}_1(x_1),$$

Here $\bar{f}_1(x_1)$ is given by (51) derived in Appendix 1. To analyse the stability, we have to first compute the equilibrium velocity by solving (52) and then to analyse the Jacobian of $\bar{f}_1(x_1)$ at x_1^e, i.e. $(\partial \bar{f}_1 / \partial x_1)(x_1^e)$. We will show that $(\partial \bar{f}_1 / \partial x_1)(x_1^e) < 0$ and therefore by the first method of Lyapunov x_1^e is the locally exponentially stable equilibrium of (51). To be more specific, rewrite (52) as follows:

$$0 = \left((x_1^e)^2\right)\left[\cot(x_2^e)\left(b_1 b_5 - \frac{b_7 b_8 b_{14}}{b_{10}}\right) \right.$$
$$+ x_2^e \cot(x_2^e)\left(b_1 b_{13} - \frac{b_7 b_8 b_{15}}{b_{10}}\right) + b_1 b_{11} + b_1 b_{12} x_2^e \right]$$
$$+ \left[b_4 \cot(x_2^e)\cos(x_2^e - x_4^e) - \frac{b_2}{b_{10}}(b_2 b_{14} + b_8 b_{15} x_2^e) + b_4 \sin(x_2^e - x_4^e)\right], \tag{27}$$

here x_2^e, x_4^e are given required reference angle of attack and pitch angle and x_1^e is the velocity to be determined. Equation (27) is obviously a simple quadratic equation of the form $A(x_1^e)^2 + B = 0$.

$$u_1 = \frac{-(b_8 b_{14} x_1^2 + b_8 b_{15} x_2 x_1^2 + b_9 x_1 x_3) + \ddot{x}_4^{\mathrm{ref}} + k_3\left(x_3 - \dot{x}_4^{\mathrm{ref}}\right) + k_4\left(x_4 - x_4^{\mathrm{ref}}\right)}{b_{10} x_1^2}. \tag{25}$$

$$u_2 = \frac{-(b_1 b_5 x_1 + b_1 b_{13} x_2 x_1 + b_6 x_3 + x_3 + b_4 x_1^{-1} \cos(x_2 - x_4)) b_{10} x_1^2 + (b_8 b_{14} x_1^2 + b_8 b_{15} x_2 x_1^2 + b_9 x_1 x_3) b_7 x_1}{(b_{10} x_1^2)(-b_3 x_1^{-1} \sin x_2)}$$
$$+ \frac{\left(\dot{x}_2^{\mathrm{ref}} + k_2\left(x_2 - x_2^{\mathrm{ref}}\right)\right) b_{10} x_1^2 - b_7 x_1\left(\ddot{x}_4^{\mathrm{ref}} + k_3\left(x_3 - \dot{x}_4^{\mathrm{ref}}\right) + k_4\left(x_4 - x_4^{\mathrm{ref}}\right)\right)}{(b_{10} x_1^2)(-b_3 x_1^{-1} \sin x_2)}. \tag{26}$$

The coefficient of $(x_1^e)^2$ is $A = \cot(x_2^e)[(b_1b_5 - (b_7b_8b_{14}/b_{10})) + x_2^e(b_1b_{13} - (b_7b_8b_{15}/b_{10}))] + b_1b_{11} + b_1b_{12}x_2^e$, and $B = [b_4\cot(x_2^e)\cos(x_2^e - x_4^e) - (b_2/b_{10})(b_2b_{14} + b_8b_{15}x_2^e) + b_4\sin(x_2^e - x_4^e)]$.

Consider the term A, here $\cot(x_2^e)[(b_1b_5 - (b_7b_8b_{14}/b_{10})) + x_2^e(b_1b_{13} - (b_7b_8b_{15}/b_{10}))]$ is associated with the lift. Here by definition, for $x_2^e > 0$, the lift produced is considered to be negative (by convention), hence $(b_1b_5 - (b_7b_8b_{14}/b_{10})) + x_2^e(b_1b_{13} - (b_7b_8b_{15}/b_{10})) < 0$. In addition when $x_2^e > 0$, $\cot(x_2^e) > 0$ and $x_2^e < 0$, $\cot(x_2^e) < 0$. Also the term $(b_1b_{11} + b_1b_{12}x_2^e)$ is associated with drag and by definition it is always negative. This implies that the coefficient of $(x_1^e)^2$ is always negative.

Now consider the term B. Here the term $(b_2/b_{10})(b_2b_{14} + b_8b_{15}x_2^e)$ is associated with the coefficient of pitching moment. Hence for $x_2^e > 0$, $(b_2/b_{10})(b_2b_{14} + b_8b_{15}x_2^e) > 0$ and $x_2^e < 0$, $(b_2/b_{10})(b_2b_{14} + b_8b_{15}x_2^e) < 0$. Therefore for B to be positive, it is necessary to satisfy that

$$\cos(x_2^e - x_4^e) + \sin(x_2^e - x_4^e) > 0. \tag{28}$$

From (28), it can be said that for every combination of x_2^e and x_4^e B is positive. Hence, it can be concluded that for every selection of x_2^e, x_4^e (27) can be solved to find a unique equilibrium velocity x_1^e.

To study the local stability of (27) its linear approximation around the selected equilibrium points $x = (x_1^e, x_2^e, 0, x_4^e)$ is considered. Thus the partial derivative of (27) (Jacobian) becomes:

$$\dot{x}_1 = [2x_1^e\cot(x_2^e)(b_1b_5 + b_1b_{13}x_2^e) - \frac{2b_2x_1^e}{b_{10}}(b_8b_{14} + b_8b_{15}x_2^e) + \\ - \frac{b_7\cot(x_2^e)x_1^e}{b_{10}}(b_8b_{14} + b_8b_{15}x_2^e)][x_1 - x_1^e] + \mathcal{O}[x_1 - x_1^e]. \tag{29}$$

The simplified Jacobian (J_{x1}) from (29) can be written as

$$J_{x1} = x_1^e\Big[2\cot(x_2^e)(b_1b_5 + b_1b_{13}x_2^e) + 2(b_1b_{11} + b_1b_{12}x_2^e) \\ + \Big(-\frac{2b_2}{b_{10}} - \frac{b_7\cot(x_2^e)}{b_{10}}\Big)(b_8b_{14} + b_8b_{15}x_2^e)\Big]. \tag{30}$$

Following (30), it can be seen that for $x_2^e > 0$ or $x_2^e < 0$ the terms $2\cot(x_2^e)(b_1b_5 + b_1b_{13}x_2^e) < 0$ and $2(b_1b_{11} + b_1b_{12}x_2^e) < 0$. For $x_2^e > 0$ the term $\Big(-\frac{2b_2}{b_{10}} - \frac{b_7\cot(x_2^e)}{b_{10}}\Big)(b_8b_{14} + b_8b_{15}x_2^e) > 0$ and for $x_2^e < 0$, $\Big(-\frac{2b_2}{b_{10}} - \frac{b_7\cot(x_2^e)}{b_{10}}\Big)(b_8b_{14} + b_8b_{15}x_2^e) < 0$. Also

$$\Big|2\cot(x_2^e)(b_1b_5 + b_1b_{13}x_2^e) + 2(b_1b_{11} + b_1b_{12}x_2^e)\Big| \\ \gg \Big|\Big(-\frac{2b_2}{b_{10}} - \frac{b_7\cot(x_2^e)}{b_{10}}\Big)(b_8b_{14} + b_8b_{15}x_2^e)\Big|.$$

Thus it holds that the term J_{x1} in (30) is always negative. Therefore linear approximation in (29) takes the form:

$$\dot{x}_1 = \tau x_1^e(x_1 - x_1^e).$$

Here,

$$\tau = \Big|2\cot(x_2^e)(b_1b_5 + b_1b_{13}x_2^e) + 2(b_1b_{11} + b_1b_{12}x_2^e) \\ + \Big(-\frac{2b_2}{b_{10}} - \frac{b_7\cot(x_2^e)}{b_{10}}\Big)(b_8b_{14} + b_8b_{15}x_2^e)\Big| < 0.$$

This confirms that any positive equilibrium velocity x_1^e is exponentially stable, i.e. the zero-dynamics of the controller is exponentially stable. It should be noted that the value of τ is small. Therefore, during tracking the target values of pitch angle and angle of attack, the change in the velocity will not be very fast or rapid. It can be noted that flight path angle $\gamma = x_4 - x_2$, so by choosing appropriate angle of the attack and pitch angle, flight patch angle can controlled.

3.2 Flight controller for pitch angle and velocity (Flight Controller No. 2)

This flight controller can be used for pitch angle (x_4) control while maintaining or tracking a certain desired velocity (x_1), when, e.g. during the cruising or steady climb. In this controller, x_4 is controlled using the elevator deflection (u_1) and x_1 is controlled by the engine throttle (u_2).

3.2.1 Control design.: The control objective for this controller is to design a tracking controller for x_1 and x_4. Thus the auxiliary outputs chosen to get the partial exact feedback linearisation for Flight Controller No. 2, denoted as $h^2(x)$ are as follows:

$$h^2(x) = \begin{bmatrix} x_1 \\ x_4 \end{bmatrix}.$$

Let the virtual inputs to stabilise $\dot{x}_3$ be v_1 and to control $\dot{x}_1$ be v_2. Lie derivative computation of $h^2(x)$ following (14) and (15) shows that the relative degrees $r = (1, 2)$. This allows us to obtain the feedback linearised form of the system (13) as

$$\dot{x}_1 = v_2,$$
$$\dot{x}_3 = v_1,$$
$$\dot{x}_4 = x_3.$$

The virtual inputs v_1 and v_2 are defined as follows:

$$\begin{bmatrix} v_1 \\ v_2 \end{bmatrix} = \begin{bmatrix} f_3 \\ f_1 \end{bmatrix} + \begin{bmatrix} g_{31} & 0 \\ g_{11} & g_{12} \end{bmatrix}\begin{bmatrix} u_1 \\ u_2 \end{bmatrix}. \tag{31}$$

The conditions for the existence of the relative degree as mentioned in (14 and 15) hold if and only if $x_1 \neq 0$ and $x_2 \neq (l/2)\pi$, l is an integer. Therefore, in the control design we consider the aircraft is in some state where $x_1 \neq 0$, $x_2 \neq (l/2)\pi$. These conditions are satisfied in all real flight conditions because the aircraft velocity can never be zero and the angle of attack cannot be $(l/2)\pi$. Following (31) the input equations for u_1 and u_2 can be rewritten as follows:

$$\begin{bmatrix} u_1 \\ u_2 \end{bmatrix} = \begin{bmatrix} g_{31} & 0 \\ g_{11} & g_{12} \end{bmatrix}^{-1}\Big[-\begin{bmatrix} f_3 \\ f_1 \end{bmatrix} + \begin{bmatrix} v_1 \\ v_2 \end{bmatrix}\Big].$$

$$u_1 = \frac{-(b_8b_{14}x_1^2 + b_8b_{15}x_2x_1^2 + b_9x_1x_3) + v_1}{b_{10}x_1^2}. \tag{32}$$

(see (33))

The complete closed form expression for u_2 is given as (see (34)) k_3, k_4, x_3^{ref}, x_4^{ref} are the same as in Section 3.1.1. Here x_1^{ref} is the desired reference velocity, k_1 is the feedback tracking control gain and has the value $k_1 < 0$. Combining these two controllers enables us to control pitch angle x_4 and velocity x_1 at the same time, provided that the corresponding hidden internal dynamics of the angle of attack x_2 has favourable properties.

3.2.2 Internal dynamics of the angle of attack (x_2).: During the design of the controller, the angle of attack x_2 is left uncontrolled.

5

This corresponds to the hidden uncontrolled internal dynamics. It is essential to check and ensure that this internal dynamics of the angle of attack is stable. Now, to check the stability of the internal dynamics, substitute the expression of control input u_1 (25) and u_2 (33) into the equation of $\dot{x}_2$ in (13). For simplicity, zero-dynamics are studied. Hence for reference tracking $x_1^{\text{ref}}(t)$, $x_4^{\text{ref}}(t)$, $x_3^{\text{ref}}(t)$ the virtual inputs $v_1 = v_2 = 0$. For purposes of the analysis, constant reference tracking are considered. This means $x_1^{\text{ref}} \equiv x_1^e$, $x_4^{\text{ref}} \equiv x_4^e$, $\dot{x}_3^{\text{ref}} \equiv 0$ and therefore we have to analyse stability of the equilibrium of the angle of attack's internal dynamics given by

$$\dot{x}_2 = \bar{f}_2(x_2),$$

Here $\bar{f}_2(x_2)$ is given by (55) derived in Appendix 2. To analyse the stability, we have to first compute the equilibrium of the one-dimensional angle of attack by solving (56) and than to analyse the Jacobian of $\bar{f}_2(x_2)$ at x_1^e, i.e. $(\partial \bar{f}_2/\partial x_2)(x_2^e)$. We will show that $(\partial \bar{f}_2/\partial x_2)(x_2^e) < 0$ and therefore by the first method of Lyapunov x_2^e is the locally exponentially stable equilibrium of (55). To be more specific, rewrite (56) as follows:

$$
\begin{aligned}
&b_1 b_5 x_1^e(x_1^e) + b_1 b_{13} x_1^e x_2^e x_1^e + (b_4\cos(x_2^e - x_4^e)) \\
&+ (b_8 x_1^e \tan(x_2^e) x_1^e)(b_{14} + b_{15} x_2^e) + \\
&- (b_{10}^{-1}(b_7 + b_2 x_1^e \tan(x_2^e))(b_4 \sin(x_2^e - x_4^e))) \\
&- (b_{10}^{-1}(b_1 b_{11} x_1^{e2} + b_1 b_{12} x_1^{e2} x_2^e)) = 0.
\end{aligned}
\tag{35}
$$

The above equation can be solved numerically for the equilibrium x_2^e. However, the crucial aspect here is to check that for every selection of x_1^e and x_4^e, the equilibrium solution for x_2^e is within the stall angle range. As a matter of fact, when choosing x_1^e and x_4^e it is important to solve (35) for x_2^e and to ensure that x_2^e is less than stall angle.

To study the local stability of (35) around the equilibrium point $(x_1^e, x_2^e, 0, x_4^e)$, its linear approximation is considered. The partial derivative of (35) (Jacobian), J_{x2} becomes

$$\dot{x}_1 = J_{x2}[x_2 - x_2^e] + \mathcal{O}[x_2 - x_2^e].\tag{36}$$

$$
\begin{aligned}
J_{x2} = {}& b_1 b_{13} x_1^e + b_8 b_{15} x_1^e \tan(x_2^e) \\
& + \frac{(b_2 \sec^2(x_2^e))(b_4 \sin(x_4^e - x_2^e) + b_1 b_{11} x_1^{e2} + b_1 b_{12} x_1^{e2} x_2^e)}{b_{10}} \\
& + \frac{b_4 \sin(x_4^e - x_2^e)}{x_1^e} + (b_8 x_1^e \sec^2(x_2^e))(b_{14} + b_{15} x_2^e) \\
& - \frac{(b_7 + b_2 x_1^e \tan(x_2^e))(b_1 b_{12} x_1^{e2} + b_4 \cos(x_4^e - x_2^e))}{b_{10} x_1^e}
\end{aligned}
\tag{37}
$$

The term

$$\frac{(b_2 \sec^2(x_2^e))(b_4 \sin(x_4^e - x_2^e) + b_1 b_{11} x_1^{e2} + b_1 b_{12} x_1^{e2} x_2^e)}{b_{10}}$$

is related to the drag and engine thrust, hence it is always zero or negative (in practice aircraft cannot fly backward) for any values of x_2^e. The term $b_1 b_{13} x_1^e + b_8 b_{15} x_1^e \tan(x_2^e) < 0$ in (37) for any values of x_2^e. The term $(b_8 x_1^e \sec^2(x_2^e))(b_{14} + b_{15} x_2^e)$ is related to the pitching moment, therefore for $x_2^e > 0$, the term $(b_8 x_1^e \sec^2(x_2^e))(b_{14} + b_{15} x_2^e) > 0$ and for $x_2^e < 0$, $(b_8 x_1^e \sec^2(x_2^e))(b_{14} + b_{15} x_2^e) < 0$. The term

$$\frac{(b_7 + b_2 x_1^e \tan(x_2^e))(b_1 b_{12} x_1^{e2} + b_4 \cos(x_4^e - x_2^e))}{b_{10} x_1^e} < 0$$

is related to the drag, lift, pitching moment produced by the elevator deflection (δe). Hence term

$$\frac{(b_7 + b_2 x_1^e \tan(x_2^e))(b_1 b_{12} x_1^{e2} + b_4 \cos(x_4^e - x_2^e))}{b_{10} x_1^e} > 0$$

for or any values of x_2^e. The condition for J_{x1} to be negative is (see (38))

The condition in (38) is easily satisfied because the terms on the right hand side are much smaller than the terms on the left hand side. Hence, (36) can be written as

$$\dot{x}_2 = \lambda(x_2 - x_2^e).$$

Here $\lambda = J_{x2} < 0$. This confirms that the state x_2^e is exponentially stable, i.e. the zero-dynamics of the controller is exponentially stable. It has been shown that for any combination of velocity x_1^e and pitch angle x_4^e the zero-dynamics of the angle of

$$
\begin{aligned}
u_2 = {}& \frac{-(b_1 b_{11} x_1^2 + b_1 b_{12} x_2 x_1^2 + b_4 \sin(x_2 - x_4))b_{10} x_1^2 + (b_8 b_{14} x_1^2 + b_8 b_{15} x_2 x_1^2 + b_9 x_1 x_3)b_2 x_1^2}{(b_3\cos(x_2))(b_{10} x_1^2)} \\
& + \frac{-b_2 x_1^2 v_1 + b_{10} x_1^2 v_2}{(b_3 \cos(x_2))(b_{10} x_1^2)}.
\end{aligned}
\tag{33}
$$

$$
\begin{aligned}
u_2 = {}& \frac{-(b_1 b_{11} x_1^2 + b_1 b_{12} x_2 x_1^2 + b_4 \sin(x_2 - x_4))b_{10} x_1^2 + (b_8 b_{14} x_1^2 + b_8 b_{15} x_2 x_1^2 + b_9 x_1 x_3)b_2 x_1^2}{(b_3 \cos(x_2))(b_{10} x_1^2)} \\
& \frac{-b_2 x_1^2(\ddot{x}_4^{\text{ref}} + k_3(x_3 - \dot{x}_4^{\text{ref}}) + k_4(x_4 - x_4^{\text{ref}})) + b_2 x_1^2(\dot{x}_1^{\text{ref}} + k_1(x_1 - x_1^{\text{ref}}))}{(b_3 \cos(x_2))(b_{10} x_1^2)}.
\end{aligned}
\tag{34}
$$

$$
\begin{aligned}
&\left| \frac{(b_7 + b_2 x_1^e \tan(x_2^e))(b_1 b_{12} x_1^{e2} + b_4 \cos(x_4^e - x_2^e))}{b_{10} x_1^e} \right| + \left| b_1 b_{13} x_1^e + b_8 b_{15} x_1^e \tan(x_2^e) \right| \\
&\left| \frac{(b_2 \sec^2(x_2^e))(b_4 \sin(x_4^e - x_2^e) + b_1 b_{11} x_1^{e2} + b_1 b_{12} x_1^{e2} x_2^e)}{b_{10}} \right| \\
&> \left| (b_8 x_1^e \sec^2(x_2^e))(b_{14} + b_{15} x_2^e) + b_4 \sin(x_4^e - x_2^e) \right|.
\end{aligned}
\tag{38}
$$

attack x_2^e is exponentially stable. However, it is crucial to calculate the equilibrium angle of attack x_2^e and to check that if it lies within the operational range to avoid stall.

3.3 Flight controller for angle of attack and velocity (Flight Controller No. 3)

This controller can be used in critical conditions where the aircraft is about to exceeded the stall angle and/or exceeded the maximum construction velocity. A quick automatic recovery controller is needed to bring the angle of attack (x_2) back to a reasonable value. Two crucial tasks in aircraft stall recovery are to get the angle of attack (x_2) within the normal operation range and to control the velocity (x_1) of the aircraft so that it does not fly too fast or too slow. Here the velocity (x_1) is controlled by the engine throttle (u_2), and the angle of attack (x_2) by the elevator deflection (u_1).

3.3.1 Control design.: The control objective for this controller is to design a tracking controller for x_2 and x_1. Thus the auxiliary outputs chosen to get the partial exact feedback linearisation for Flight Controller No. 3, denoted as $h^3(x)$ are as follows:

$$h^3(x) = \begin{bmatrix} x_1 \\ x_2 \end{bmatrix}.$$

Let the virtual inputs to control $\dot{x}_2$ and $\dot{x}_1$ be v_1 and v_2. Lie derivative computation of $h^3(x)$ following (14) and (15) shows that it has the relative degrees $r = (1, 1)$. This gives a two-dimensional internal dynamics. Hence, the feedback linearised form of the system (13) is obtained as follows:

$$\dot{x}_1 = v_2,$$
$$\dot{x}_2 = v_1,$$

The virtual inputs v_1 and v_2 are defined as follows:

$$\begin{bmatrix} v_1 \\ v_2 \end{bmatrix} = \begin{bmatrix} f_2 \\ f_1 \end{bmatrix} + \begin{bmatrix} g_{21} & g_{22} \\ g_{11} & g_{12} \end{bmatrix} \begin{bmatrix} u_1 \\ u_2 \end{bmatrix}. \tag{39}$$

The conditions for the existence of the relative degree as mentioned in (14) and (15) hold if and only if, $x_1 \neq 0$, i.e. for any non-zero velocity of the aircraft. Following (39) the input equations for u_1 and u_2 can be rewritten as follows:

$$\begin{bmatrix} u_1 \\ u_2 \end{bmatrix} = \begin{bmatrix} g_{21} & g_{22} \\ g_{11} & g_{12} \end{bmatrix}^{-1} \left[-\begin{bmatrix} f_2 \\ f_1 \end{bmatrix} + \begin{bmatrix} v_1 \\ v_2 \end{bmatrix} \right].$$

$$u_1 = \frac{(b_1 b_{11} x_1^2 + b_1 b_{12} x_2 x_1^2 + b_4 \sin(x_2 - x_4))(-b_3 x_1^{-1} \sin(x_2))}{(b_3 \cos(x_2))(b_7 x_1) - (b_2 x_1^2)(-b_3 x_1^{-1} \sin(x_2))}$$
$$+ \frac{(b_3 \cos(x_2) v_1) - (-b_3 x_1^{-1} \sin(x_2) v_2)}{(b_3 \cos(x_2))(b_7 x_1) - (b_2 x_1^2)(-b_3 x_1^{-1} \sin(x_2))}$$
$$- \frac{(b_1 b_5 x_1 + b_1 b_{13} x_2 x_1 + b_6 x_3 + x_3 + b_4 x_1^{-1} \cos(x_2 - x_4))b_3 \cos(x_2)}{(b_3 \cos(x_2))(b_7 x_1) - (b_2 x_1^2)(-b_3 x_1^{-1} \sin(x_2))}. \tag{40}$$

$$u_2 = \frac{-(b_1 b_{11} x_1^2 + b_1 b_{12} x_2 x_1^2 + b_4 \sin(x_2 - x_4))b_7 x_1}{(b_3 \cos(x_2))(b_7 x_1) - (b_2 x_1^2)(-b_3 x_1^{-1} \sin(x_2))}$$
$$+ \frac{-(b_2 x_1^2) v_1 + (b_7 x_1) v_2}{(b_3 \cos(x_2))(b_7 x_1) - (b_2 x_1^2)(-b_3 x_1^{-1} \sin(x_2))}$$
$$+ \frac{(b_1 b_5 x_1 + b_1 b_{13} x_2 x_1 + b_6 x_3 + x_3 + b_4 x_1^{-1} \cos(x_2 - x_4))b_2 x_1^2}{(b_3 \cos(x_2))(b_7 x_1) - (b_2 x_1^2)(-b_3 x_1^{-1} \sin(x_2))} \tag{41}$$

Combining the two controllers enables us to control the angle of attack (x_2) and the velocity (x_1), provided that the two-dimensional internal dynamics are stable and have favourable properties.

3.3.2 Internal dynamics of pitch rate (x_3) and pitch angle (x_4).: During design of the controller, the pitch rate x_3 and the pitch angle x_4 are left uncontrolled. This corresponds to the hidden uncontrolled internal dynamics. In this controller, the internal dynamics is two dimensional. Now, to checking the internal dynamics, substitute the expression of control input u_1 and u_2 (40) and (41) into the equation of $\dot{x}_3$ and $\dot{x}_4$ in (13). For simplicity, zero-dynamics are studied. Hence, for reference tracking $x_1^{ref}(t), x_2^{ref}(t)$, the virtual inputs are set to $v_1 = v_2 = 0$. For the purposes of the analysis, constant reference tracking is considered. This means $x_1^{ref} \equiv x_1^e, x_2^{ref} \equiv x_2^e$. Thus, the equilibrium equation for x_3 and x_4 gets

$$\begin{bmatrix} \dot{x}_3 \\ \dot{x}_4 \end{bmatrix} = \begin{bmatrix} f_3 + (b_{10} x_1^2) u_1 \\ f_4 \end{bmatrix} = \begin{bmatrix} 0 \\ 0 \end{bmatrix}.$$

This can be expanded to give (see Appendix 3 for details of the derivation):

$$\begin{bmatrix} \dot{x}_3 \\ \dot{x}_4 \end{bmatrix} = \begin{pmatrix} \Phi_3 \\ \Phi_4 \end{pmatrix} = 0$$

(see (42))

Here Φ is the internal dynamics function. For every selection of x_1^e and x_2^e, there are unique equilibrium x_3^e and x_4^e such that (42) is zero. For analysing the local stability, we need to analyse the Jacobian of (42). The Jacobian of (42) will be a 2×2 square matrix due to two-dimensional internal dynamics. For the stability proof, we will show that real parts of the eigenvalues of the Jacobian of (42) are negative at the equilibrium.

To study the local stability of (42), its linear approximation around the selected equilibrium points $x = (x_1^e, x_2^e, x_3^e, x_4^e)$ is considered. Here, $x_3^e = 0$ because at the equilibrium pitch angle x_4^e, the pitch rate x_3^e must be zero. The partial derivative of (42) (Jacobian) becomes:

$$\begin{bmatrix} \dot{x}_3 \\ \dot{x}_4 \end{bmatrix} = \begin{bmatrix} \dfrac{\partial \Phi_3}{\partial x_3} & \dfrac{\partial \Phi_3}{\partial x_4} \\ \dfrac{\partial \Phi_4}{\partial x_3} & \dfrac{\partial \Phi_4}{\partial x_4} \end{bmatrix} \begin{bmatrix} (x_3 - x_3^e) \\ (x_4 - x_4^e) \end{bmatrix}.$$

Thus the Jacobian for $\dot{x}_3$ and $\dot{x}_4$ becomes:

$$\frac{\partial \Phi_3}{\partial x_3} = b_9 x_1 - \frac{b_3 b_{10} x_1^2 \cos(x_2)(b_6 + 1)}{b_3 b_7 x_1 \cos(x_2) + b_2 b_3 x_1 \sin(x_2)}, \tag{43}$$

(see (44))

$$\begin{bmatrix} \Phi_3 \\ \Phi_4 \end{bmatrix} = \begin{bmatrix} f_3 + (b_{10} x_1) \left(\dfrac{-(b_1 b_5 x_1 + b_1 b_{13} x_2 x_1 + b_6 x_3 + x_3 + b_4 x_1^{-1} \cos(x_2 - x_4) + (-b_3 x_1^{-1} \sin(x_2)) u_2) + \dot{x}_2^{ref} + k_2 (x_2 - x_2^{ref})}{b_7} \right) \\ x_3 \end{bmatrix}. \tag{42}$$

$$\frac{\partial \Phi_4}{\partial x_3} = 1, \quad \frac{\partial \Phi_4}{\partial x_4} = 0. \tag{45}$$

For the stability of the internal dynamics, the roots of the characteristic equation should be negative real roots. The roots of the characteristic equations can be calculated as follows:

$$\left\| sI - \begin{vmatrix} \dfrac{\partial \Phi_3}{\partial x_3} & \dfrac{\partial \Phi_3}{\partial x_4} \\ \dfrac{\partial \Phi_4}{\partial x_3} & \dfrac{\partial \Phi_4}{\partial x_4} \end{vmatrix} \right\| = 0.$$

$$s_{1,2} = \frac{(\partial \Phi_3/\partial x_3) \pm \sqrt{(\partial \Phi_3/\partial x_3)^2 + 4(\partial \Phi_3/\partial x_4)}}{2}.$$

Here s is the complex frequency in the Laplace transform. The condition for stability is that the real part of the roots should be negative, i.e.

1. $\partial \Phi_3/\partial x_3 < 0$ and $\partial \Phi_3/\partial x_4 < 0$.

Consider $\partial \Phi_3/\partial x_3$ (43). It can be simplified to:

$$\frac{\partial \Phi_3}{\partial x_3} = b_8 x_1 \left(c_{mac} C_{m_q} - \frac{C_{m_{\delta e}} \cos(x_2)\left(C_{L_0} + 1\right)}{b_1 \left(C_{L_{\delta e}} \cos(x_2) + C_{D_{\delta e}} \sin(x_2)\right)} \right). \tag{46}$$

The term is always $b_8 x_1 > 0$, by definition from (15). The terms C_{m_q}, $C_{m_{\delta e}} < 0$, $C_{L_{\delta e}}$, $C_{D_{\delta e}} > 0$ and $C_{L_0} \geq 0$ by definition. Substituting all these inequalities in (46) gives that $(\partial \Phi_3/\partial x_3) < 0$.

Now consider the term, $(\partial \Phi_3/\partial x_4)$ in (44), it can be simplified to give:

$$\begin{aligned} \frac{\partial \Phi_3}{\partial x_4} &= \frac{b_{10} b_4 (b_3 b_4 \cos(x_2 - x_4)\sin(x_2) - b_3 b_4 \sin(x_2 - x_4)\cos(x_2))}{b_3 b_7 \cos(x_2) + b_2 b_3 \sin(x_2)} \\ &= \frac{b_4 b_{10}(\sin(x_4))}{b_7 \cos(x_2) + b_2 \sin(x_2)}. \end{aligned} \tag{47}$$

$$\frac{\partial \Phi_3}{\partial x_4} = \frac{g b_8 C_{m_{\delta e}} \sin(x_4)}{b_1 C_{L_{\delta e}} \cos(x_2) + b_1 C_{D_{\delta e}} \sin(x_2)}. \tag{48}$$

To recover from a stall, the aircraft has to go into a nose dive motion, as such $x_4 < 0$. This implies that the numerator of (48) is always positive due to the term $\sin(x_4)$ being multiplied by $C_{m_{\delta e}} < 0$. The denominator of (48) is also always negative because it is multiplied by the term b_1 which by definition in (15) is negative. It can be therefore be concluded that for this controller $\partial \Phi_3/\partial x_3 < 0$ and $\partial \Phi_3/\partial x_4 < 0$. It can be said that the two-dimensional internal dynamics of the proposed controller is stable.

3.4 Controllers gain selection and robustness

It has been shown in Sections 3.1–3.3 that the relation between the virtual inputs and the selected the auxiliary outputs are integral (integrator). Each feedback gains (k_1, k_2, k_3 and k_4) can be computed by specifying the time constant of the closed loop. For implementation, flight-handling quality requirements should be taken into account. The flight control system should provide responses satisfying the existing specifications (MIL-STD-1797A and MIL-F-9490D) [21]. Methods for choosing the flight controller gains considering the actuator lag are presented in [22]. While choosing the gain, it is important to make a trade-off between the

response of the controlled variable and the physical actuator's limit, so as not to saturate the control inputs.

The robustness properties of the dynamic inversion have received too little attention in the literature. Some robustness analysis of the NDI controllers is presented in [23, 24]. In [23], authors proposed a sum-of-squared method to analyse the robustness properties of non-linear controller for longitudinal aircraft dynamics. In [24], authors proposed a robust NDI in combination with sliding mode control. Individual studies of each methods are out of scope in this paper. However, to study the basic parametric uncertainties, we have added $\pm 10\%$ uncertainties as an upper bound and lower bound to the nominal values of the controller gains during the simulations (see Section 4).

3.5 Switching of the flight controllers

Flight Controller No.1 can be used for situations like take-off, steady climb of the aircraft when the angle of attack is non-zero. This will allow controlling the aircraft's both angle of attack (α) and pitch angle (θ). For the steady but steep climbing, angle of attack should stay high and singularity at $\alpha = 0$ is not crucial. While using this controller, the velocity of the aircraft will be left uncontrolled. For each combination of angle of attack and pitch angle, there is a stable equilibrium velocity. Difference between the pitch angle and angle of attack is the flight path angle. Hence, this controller can be used for controlling the flight path angle by independently choosing desired angle of attack and pitch angle. For example, for horizontal cruising same tracking values of angle of attack and pitch angle resulting in zero flight path angle.

Using Flight Controller No. 2 velocity and pitch are controlled, while angle of attack is left uncontrolled. This controller can be used for situations where rapid change in pitch up or pitch down manoeuver is required while having control over the aircraft velocity. Alternatively, this flight controller can be used for faster cruise conditions. For example, assume the aircraft is flying with some reasonable angle of attack using the Flight controller No. 1. Then, for faster cruising, we can set $\theta = x_4 = 0$ and velocity (x_1) to some desired cruising fast velocity to achieve it. In conditions where the angle of attack is critically big (close to stall angle) and the velocity is too slow, Flight Controller No. 3 should be used to get angle of attack within some acceptable range.

Flight Controller No. 3 can be primarily used to recover the aircraft from critical conditions like stall while controlling the velocity while preventing the aircraft from exceeding the maximum construction velocity. The linearising feedback influences of elevator input (u_1) and engine thrust (u_2) on both velocity and angle of attack. Mainly the engine thrust is responsible for controlling the velocity and elevator for controlling the angle of attack. Coupling terms in this controller are smaller, and are rather treated as undesired coupling, which is actually compensated by the linearising feedback. Using this controller, both the angle of attack and the velocity are controlled while leaving pitch angle uncontrolled, which is not very crucial. Indeed, in situations like stall, the 'dangerous' variables are the angle of attack and the velocity. As soon as the aircraft is brought within some acceptable limits of α and velocity the controller can be switched to Flight controller No. 1 or 2.

4 Simulation results and discussion

Simulations are performed with MATLAB/Simulink to verify the proposed controllers on the aircraft model (13). The non-linear aircraft model used for the control design and validation is based on the aerodynamic and flight dynamic data of the F-16 multi-role fighter aircraft (Fig. 3). F-16 is a single-engine supersonic fighter developed by Lockheed Martin for United States Air Force. The physical parameters for the aircraft that are used are as follows [25]: $m = 636.94 \text{ slug}$, $I_{yy} = 55814 \text{ slug ft}^2$, $S = 300 \text{ ft}^2$,

$$\frac{\partial \Phi_3}{\partial x_4} = \frac{b_{10} x_1^2 ((b_3 b_4 \cos(x_2 - x_4)\sin(x_2)/x_1) - (b_3 b_4 \sin(x_2 - x_4)\cos(x_2)/x_1))}{b_3 b_7 x_1 \cos(x_2) + b_2 b_3 x_1 \sin(x_2)}, \tag{44}$$

Fig. 3 *F-16 Fighter Aircraft [26]*

$c_{\text{MAC}} = 11.32$ ft, $b = 30$ ft. The airfoil used by the F-16 aircraft is NACA 64A-204 and has $\sim 15°$ stall angle [10]. The maximum thrust of the engine (F_T) is $19,000$ lbs at the rate limited by $\pm 10,000$ lbs/s. The maximum and minimum elevator deflection (δe) is $\pm 25°$ limited by $60°$/s. The opensource MATLAB/Simulink model used for the demonstration of controller performance verification is found in [26] (https://www.aem.umn.edu/people/faculty/balas/darpa_sec/SEC.Software.html). During the simulation, changes in parameters such as ρ (air density) and ambient air temperature with respect to the altitude were considered to follow International Standard Atmospheric (ISA) condition model. The controller performances are tested using specific manoeuvres. To carry out the robustness analysis, we have considered adding $\pm 10\%$ uncertainty to the nominal values of the controller gains k_1, k_2, k_3 and k_4. For example, if the nominal controller gain value, $k_o = 100$, then the upper bound of the controller gain, $k_{\text{upper}} = 110$ and the lower bound of the controller gain, $k_{\text{lower}} = 90$.

4.1 Flight Controller No. 1

Flight path angle can be controlled by tracking pitch angle (x_4 or θ) and angle of attack (x_2 or α). To demonstrate the controller performance, the trimmed flight condition were chosen to be at velocity, $V = 550$ ft/s, and altitude 10,000 ft. For demonstrating the controller performance two different manoeuvres were chosen. For the first manoeuvre, pitch angle tracking (x_4) was set to 4° and the angle of attack (x_2) tracking was set to 3°. For the second manoeuvre, x_4 and x_2 tracking were set to $-1°$ and 1°. Both the manoeuvres were set to start from the initial trimmed condition with $x_4 = x_3 = 2.5°$. Following (22) and (24) controller parameters are listed as follows: $k_2 = -60\,\text{s}^{-1}$, $k_3 = -20\,\text{rad s}^{-1}$, and $k_4 = -40\,\text{rad s}^{-2}$. For each manoeuvre the influence of the controller uncertainties are demonstrated. Fig. 4 illustrates the simulation results.

It can be seen that the pitch angle and the angle of attack are exponentially tracked by the controller. In the first manoeuvre, for positive flight path the velocity reduces by exponentially decaying towards 500 ft/s for going against the gravity. However, for controlling the angle of attack with engine thrust, it is essential to provide more thrust to achieve exponential tracking of the angle of attack. In general providing more thrust should increase the velocity, but in the presented case it does not happen because the rate of reduction of velocity (due to pitch of motion) is much larger than the thrust used to control the angle of attack. Hence, irrespective of increasing the thrust to control increase the angle of attack, the decay of velocity decays, but rather slowly.

In the second manoeuvre, a negative flight path angle is demonstrated. It can be seen the that the velocity of the aircraft increases and stabilises at around 670 ft/s. At the beginning, higher thrust is required due to large difference between the reference angle of attack and actual angle of attack. However, gradually the thrust requirement settles down.
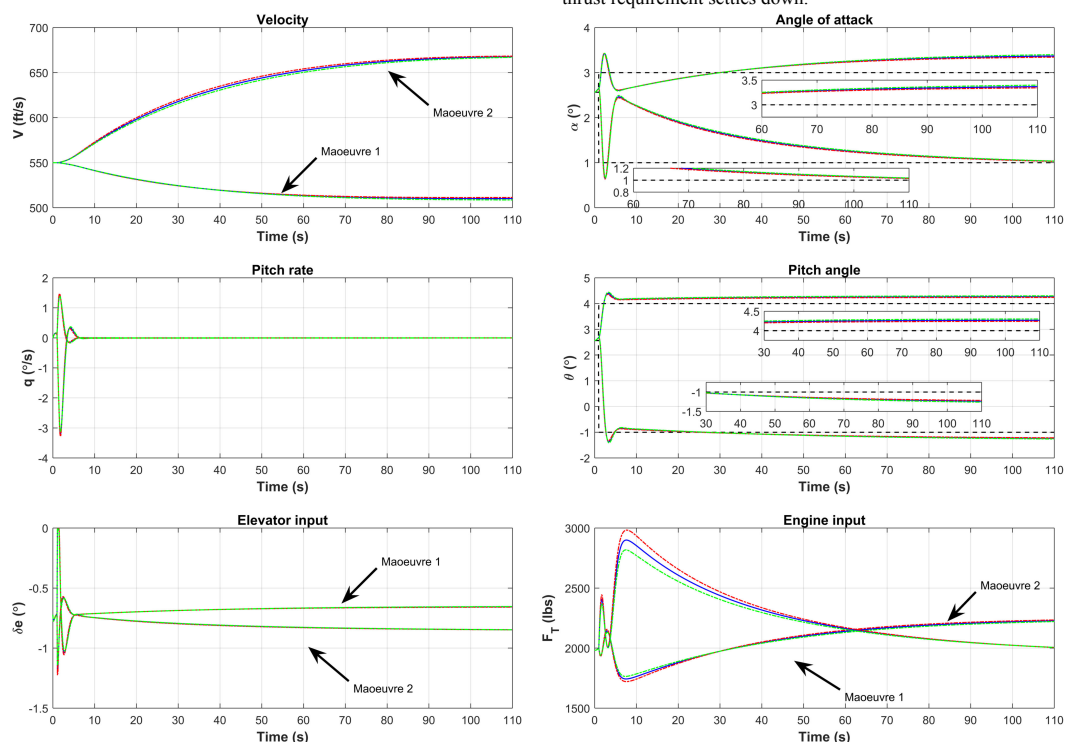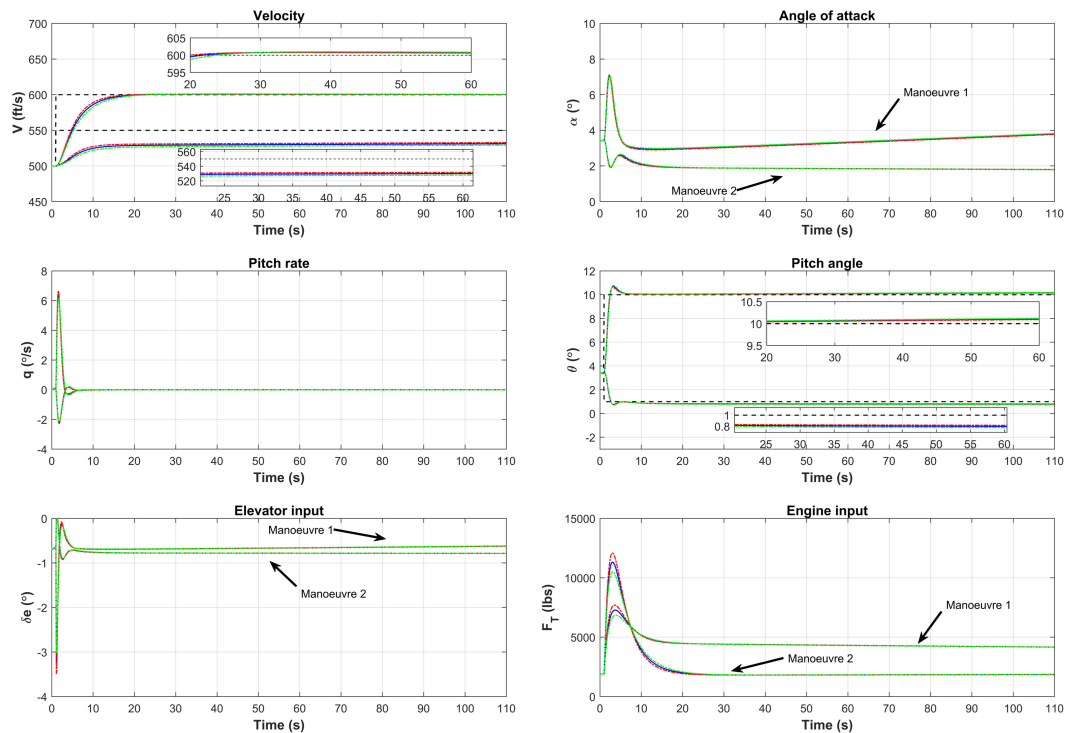

Fig. 4 *Angle of attack and pitch angle controller. Blue, red, and green show the controller performance with nominal gains, upper bound gains, and lower bound gains*

Fig. 5 *Pitch angle and velocity controller. Blue, red, and green show the controller performance with nominal gains, upper bound gains, and lower bound gains*

To demonstrate the robustness of the control gains, we carried out the simulation of each manoeuvres separately with nominal (blue), upper bound (red), and lower bound (green). For all the cases, the controller exponentially tracked the pitch angle and angle of attack. It is important to notice that for all the cases the uncontrolled velocity stabilises.

4.2 Flight Controller No. 2

To demonstrate the tracking of pitch angle (x_4 or θ) and the velocity (x_1 or V) control, the chosen initial flight condition was cruising velocity of 500 ft/s at an altitude of $10,000$ ft. Two different manoeuvres were chosen to show the performance of the controller. Firstly, a nose up motion while tracking the x_4 and x_1 at $10°$ and 550 ft/s. The second manoeuvre was chosen to be a nose dive motion while tracking the x_4 and x_1 at $1°$ and 600 ft/s, respectively. Both the manoeuvre initialised from the trimmed condition with $x_4 = 3.4°$. Following (33) and (34), the controller parameters are listed as follows: $k_1 = -100\,\mathrm{s}^{-1}$, $k_3 = -20\,\mathrm{rad\,s}^{-1}$, and $k_4 = -40\,\mathrm{rad\,s}^{-2}$. For each manoeuvre, the influence of the controller uncertainties are demonstrated in terms of nominal, upper bound, and lower bound of the controller gains. Fig. 5 illustrates the simulation results.

It can be seen that the velocity V and the pitch angle θ are exponentially tracked. It is noticeable for the pitch down motion (manoeuvre 2), the angle of attack (α) exponentially stabilises at the equilibrium value of $2°$. However, for the pitch up motion (manoeuvre 1), the angle of attack stabilised as well but a slower rate. This is because the tracking of velocity while making a pitch up motion is slower. However, it is important to notice the tracking error in pitch angle converges to the zero, and the tracking error for the velocity converges to a small value near zero. The slow convergence of the velocity tracking is due to the chosen controller gains so as not to saturate the engine thrust. To demonstrate the robustness of the control gains, we carried out the simulation of each manoeuvres separately with nominal (blue), upper bound (red), and lower bound (green). In all the cases, the desired pitch angle and velocity were exponentially tracked.

4.3 Flight Controller No. 3

The performance of the Flight Controller No.3 has been verified assuming the worst case scenario, where the aircraft has reached the stall angle x_2 or $\alpha = 14.87°$ and stall velocity x_1 or $V = 375$ ft/s at an altitude of $30,000$ ft. The two important objectives of the controller are: firstly, to bring back the angle of attack of the aircraft within the operating range and secondly, to ensure that the aircraft is not flying too slowly or too fast. Hence, for α and V tracking reference is set to $8°$ and 550 ft/s. The primary focus of the controller is to get the aircraft out of stall as quick as possible, resulting in vigorous control actions. Following (40) and (41), the controller parameters are listed as follows: $k_2 = -60\,\mathrm{s}^{-1}$ and $k_1 = -86\,\mathrm{rad\,s}^{-1}$. For the manoeuvre, the influence of the controller uncertainties are demonstrated in terms of nominal, upper bound, and lower bound of the controller gains. Fig. 6 illustrates the simulation performance of the controller.

It can be seen the that angle of attack and the velocity converges to the reference value. It is important to notice that at the start of the manoeuvre the control actions are vigorous and operates at the maximum limits. This is because the high gain values chosen for the tracking controllers of x_1 and x_2 for faster recovery from stall causing maximum control efforts from the actuators (elevator deflection (δe) and thrust (F_T)). It can also be noticed that the pitch rate (q) is exponentially stable and slowly converges to zero. It is important to note that pitch angle (θ) is directly related to pitch rate (q). This residual pitch rate causes a change in the pitch angle (θ) over a long period of time. Here, the controller is only for use in adverse situations, such as stalling. This controller is always in use
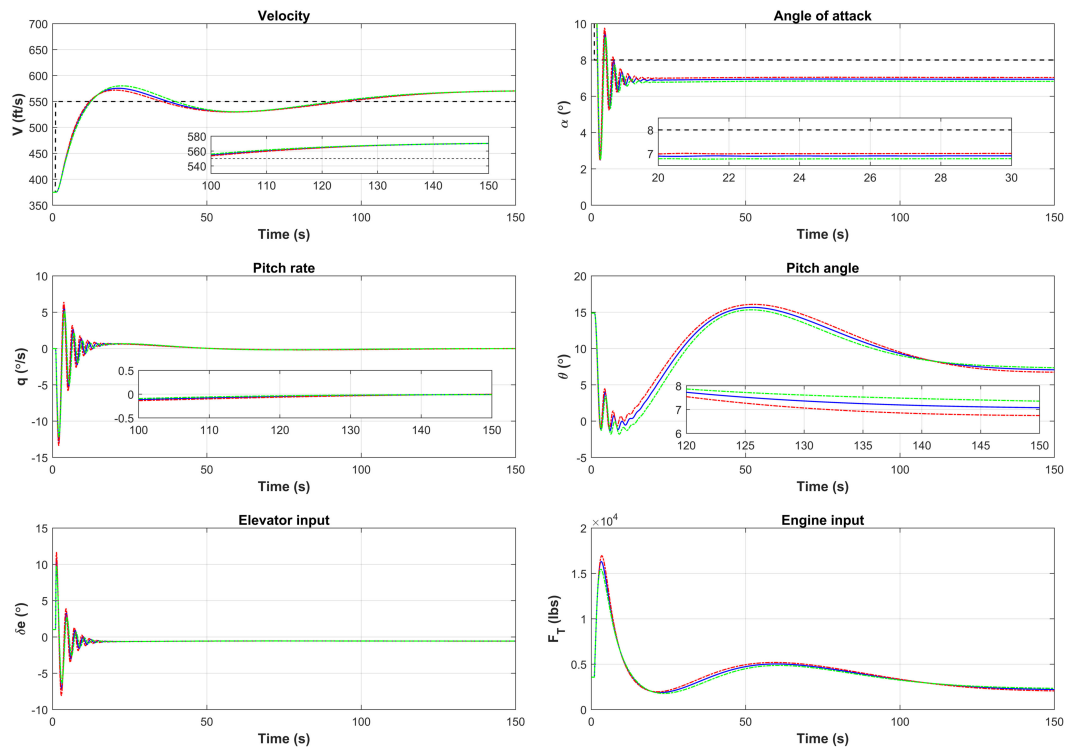
10

Fig. 6 *Angle of attack and velocity controller. Blue, red, and green show the controller performance with nominal gains, upper bound gains, and lower bound gains*

for a short duration. Exponential stability of q is not therefore a problem for this controller.

5 Conclusions

In this paper, automatic longitudinal flight controller is presented for conventional fixed-wing aircraft using non-linear dynamic inversion (NDI) technique or, in control theoretic terms, the partial exact feedback linearisation. Main theoretical results include designing of three different tracking flight controllers which provides full control of longitudinal states (velocity, angle of attack and pitch angle) of the aircraft. A detailed study on the stability of the internal dynamics for each controller are carried out and has been showed to be stable. Combination of these three flight controllers depending on the flight condition provided full 3-DOF longitudinal control authority of a fixed-wing aircraft. Simulation results demonstrate that with the proposed controllers, longitudinal motion of a conventional multi-role combat aircraft can be controlled with small tracking error.

6 Acknowledgments

7 References

[1] Goupil, P.: 'Airbus state of the art and practices on fdi and ftc in flight control system', *Control Eng. Pract.*, 2011, **19**, (6), pp. 524–539
[2] Anderson, J.D.: *Fundamentals of aerodynamics* (McGraw Hill, 2007)
[3] Schroeder, J.A., Burke, R.H.: 'Upset prevention and recovery training–a regulator update'. AIAA Modeling and Simulation Technologies Conf., 2016, pp. 1429
[4] Transportasi, K.N.K.: 'Aircraft accident investigation report'. Ministry of Transportation, Indonesia, Report, 2015
[5] 'Final Report On the accident on 1st June 2009 to the Airbus A330-203', French Civil Aviation Safety Investigation Authority Std.
[6] Wise, J., Rio, A., Fedouach, M.: 'What really happened aboard air france 447', *Popular Mech.*, 2011, **6**
[7] Johnson, E.: '*American Military Transport Aircraft since 1925*' (McFarland, 2013)
[8] Lu, B., Wu, F., Kim, S.: 'Switching lpv control of an f-16 aircraft via controller state reset', *IEEE Trans. Control Syst. Technol.*, 2006, **14**, (2), pp. 267–277
[9] Santoso, F., Liu, M., Egan, G.: 'H 2 and h α robust autopilot synthesis for longitudinal f light of a special unmanned aerial vehicle: a comparative study', *IET Control Theory Applic.*, 2008, **2**, (7), pp. 583–594
[10] Stevens, B.L., Lewis, F.L., Johnson, E.N.: '*Aircraft control and simulation: dynamics, controls design, and autonomous systems*' (John Wiley & Sons, 2015)
[11] Lane, S.H., Stengel, R.F.: 'Flight control design using nonlinear inverse dynamics'. American Control Conf., 1986, IEEE, 1986, pp. 587–596
[12] McLean, D.: 'Globally stable nonlinear flight control system', *IEE Proc. Control Theor. Appl.*, 1983, **130**, (3), pp. 93
[13] Sieberling, S., Chu, Q., Mulder, J.: 'Robust flight control using incremental nonlinear dynamic inversion and angular acceleration prediction', *J. Guid. Control Dyn.*, 2010, **33**, (6), pp. 1732–1742
[14] Chen, H., Zhang, S.: 'Robust dynamic inversion flight control law design'. 2nd Int. Symp. on Systems and Control in Aerospace and Astronautics, ISSCAA, IEEE, 2008, pp. 1–6
[15] Norton, M., Khoo, S., Kouzani, A., *et al.*: 'Adaptive fuzzy multi-surface sliding control of multiple-input and multiple-output autonomous flight systems', *IET Control Theory Applic.*, 2015, **9**, (4), pp. 587–597
[16] Khoo, S., Xie, L., Zhao, L.: 'Multi surface sliding control for fast finite time leader follower consensus with high order siso uncertain nonlinear agents', *Int. J. Robust Nonlinear Control*, 2014, **24**, (16), pp. 2368–2404
[17] Papageorgiou, C., Glover, K.: 'Robustness analysis of nonlinear flight controllers', *J. Guid. Control Dyn.*, 2005, **28**, (4), pp. 639–648
[18] Reveley, M., Briggs, J., Leone, K., *et al.*: 'Assessment of the state of the art of flight control technologies as application to adverse conditions (nasa/tm2010-216226)'. NASA TM, 2010, vol. 216226, p. 2010
[19] Wang, Q., Stengel, R.F.: 'Robust nonlinear flight control of a high-performance aircraft', *IEEE Trans. Control Syst. Technol.*, 2005, **13**, (1), pp. 15–26
[20] Slotine, J.-J.E., Li, W., *et al.*: '*Applied nonlinear control*' (Prentice-Hall, Englewood Cliffs, NJ, 1991), vol. **199**, no. 1

[21] Enns, D., Dan, B., Russ, H., *et al.*: 'Dynamic inversion: an evolving methodology for flight control design', *Int. J. Control*, 1994, **59**, (1), pp. 71–91

[22] Baba, Y., T.L., Sano, M.: 'Design of a nonlinear flight controller based on dynamic inversion'. IEEE Proc. of the 34th SICE Annual Conf. Int. Session Papers, 1995, pp. 1487–1492

[23] Ataei, A., Qian, W.: 'Non-linear control of an uncertain hypersonic aircraft model using robust sum-of-squares method', *IET Control Theory Applic.*, 2012, **6**, (2), pp. 203–215

[24] Yang, I., Dongik, L., Dong, H.: 'Designing a robust nonlinear dynamic inversion controller for spacecraft formation flying', *Math. Probl. Eng.*, 2014

[25] Nguyen, L.T. 'Simulator study of stall/post-stall characteristics of a fighter airplane with relaxed longitudinal static stability'. National Aeronautics and Space Administration, Technical Report NASA Technical Paper 1538, 1979

[26] Russell, R.S. 'Non-linear f-16 simulation using Simulink and Matlab', University of Minnesota, Technical Paper, 2003

8 Appendix

8.1 Appendix 1: derivation of Flight Controller No. 1

Deriving the equation of the control inputs u_1 and u_2 in the form of $f(x)$ and $g(x)$, we get

$$u_1 = \frac{-f_3 + v_1}{g_{31}}. \tag{49}$$

$$u_2 = \frac{(f_3 - v_1)g_{21}}{g_{22}g_{31}} - \frac{f_2 - v_2}{g_{22}}. \tag{50}$$

Substituting $v_1 = v_2 = 0$, in (49) and (50) we get,

$$u_1 = \frac{-f_3}{g_{31}}, \quad u_2 = \frac{(f_3)g_{21}}{g_{22}g_{31}} - \frac{f_2}{g_{22}}.$$

Now substitute the expression of control input u_1 and u_2 above into the equation of $\dot{x}_1$ in (13), we get

$$\dot{x}_1 = f_1 + g_{11}u_1 + g_{12}u_2.$$

$$\dot{x}_1 = f_1 + g_{11}\frac{-f_3}{g_{31}} + g_{12}\frac{(f_3)g_{21}}{g_{22}g_{31}} - \frac{f_2 g_{12}}{g_{22}}$$

$$= f_1 + \left(\frac{g_{12}g_{21}}{g_{22}g_{31}} - \frac{g_{11}}{g_{31}}\right)f_3 - \frac{f_2 g_{12}}{g_{22}}.$$

$$\frac{g_{12}g_{21}}{g_{22}g_{31}} - \frac{g_{11}}{g_{31}} = \frac{-b_7\cot(x_2^e) - b_2}{b_{10}}, \quad \frac{g_{12}}{g_{22}} = -x_1^e\cot(x_2^e).$$

$$\frac{g_{12}g_{21}}{g_{22}g_{31}} - \frac{g_{11}}{g_{31}} = \frac{-b_7\cot(x_2) - b_2}{b_{10}}, \quad \frac{g_{12}}{g_{22}} = -x_1\cot(x_2).$$

Now substitute $x_3^e = 0$ in the equation of $\dot{x}_1$ above, we get the internal dynamics as follows:

$$\dot{x}_1 = \bar{f}_1(x_1),$$

Here, (see (51))

The equilibrium point of this zero-dynamics (or also equilibrium velocity) x_1^e can be computed solving the following algebraic equation:

$$\bar{f}_1(x_1^e) = 0. \tag{52}$$

8.2 Appendix 2: derivation of Flight Controller No. 2

Deriving the equation of the control inputs u_1 and u_2 in the form of $f(x)$ and $g(x)$, we get

$$u_1 = \frac{-f_3 + v_1}{g_{31}}. \tag{53}$$

$$u_2 = \frac{(f_3 - v_1)g_{11}}{g_{12}g_{31}} - \frac{f_1 - v_2}{g_{12}}. \tag{54}$$

Substituting $v_1 = v_2 = 0$, in (53) and (54) we get,

$$u_1 = \frac{-f_3}{g_{31}}, \quad u_2 = \frac{(f_3)g_{11}}{g_{12}g_{31}} - \frac{f_1}{g_{12}}.$$

Now substitute the expression of control input u_1 and u_2 above into the equation of $\dot{x}_2$ in (13), we get:

$$\dot{x}_2 = f_2 + g_{21}u_1 + g_{22}u_2$$

$$\dot{x}_2 = f_2 + g_{21}\frac{-f_3}{g_{31}} + g_{22}\frac{(f_3)g_{11}}{g_{12}g_{31}} - \frac{f_1 g_{22}}{g_{12}}$$

$$= f_2 + \left(\frac{g_{22}g_{11}}{g_{12}g_{31}} - \frac{g_{21}}{g_{31}}\right)f_3 - \left(\frac{g_{22}}{g_{12}}\right)f_1$$

(see equation below)

$$\frac{g_{22}}{g_{12}} = \frac{-b_3 x_1^{e-1}\sin(x_2^e)}{b_3\cos(x_2^e)} = \frac{-\tan(x_2^e)}{x_1^e}.$$

Now substitute $x_3^e = 0$ in the equation of $\dot{x}_2$ above, we get the internal dynamics as follows:

$$\dot{x}_2 = \bar{f}_2(x_2),$$

here,

$$\bar{f}_2(x_2) = b_1 b_5 x_1^e + b_1 b_{13} x_1^e x_2 + \frac{(b_4\cos(x_2 - x_4^e))}{x_1^e}$$

$$+ (b_8 x_1^e\tan(x_2))((b_{14} + b_{15}x_2))$$

$$- \left(\frac{(b_7 + b_2 x_1^e\tan(x_2))(b_4\sin(x_2 - x_4^e))}{b_{10}x_1^e}\right) \tag{55}$$

$$- \left(\frac{(b_1 b_{11} x_1^{e2} + b_1 b_{12} x_1^{e2} x_2)}{b_{10}x_1^e}\right).$$

$$\bar{f}_1 = \left((x_1^e)^2\right)\left[\cot(x_2^e)\left(b_1 b_5 - \frac{b_7 b_8 b_{14}}{b_{10}}\right)\right.$$

$$+ x_2^e\cot(x_2^e)\left(b_1 b_{13} - \frac{b_7 b_8 b_{15}}{b_{10}}\right) + b_1 b_{11} + b_1 b_{12} x_2^e\right] \tag{51}$$

$$+ \left[b_4\cot(x_2^e)\cos(x_2^e - x_4^e) - \frac{b_2}{b_{10}}(b_2 b_{14} + b_8 b_{15}x_2^e) + b_4\sin(x_2^e - x_4^e)\right]$$

$$\frac{g_{22}g_{11}}{g_{12}g_{31}} - \frac{g_{21}}{g_{31}} = \frac{b_2 x_1^{e2}(-b_3 x_1^{e-1}\sin(x_2^e))}{b_3\cos(x_2^e)b_{10}x_1^e} - \frac{b_7 x_1^e}{b_{10}x_1^{e2}} = \frac{-b_3 x_1^e\tan(x_2^e) - b_7}{b_{10}x_1^e}.$$

Simplifying the equation above, the equilibrium point of this zero-dynamics (or also equilibrium angle of attack x_2^e can be computed solving the following algebraic equation:

$$\bar{f}_2(x_2^e) = b_1 b_5 x_1^e(x_1^e) + b_1 b_{13} x_1^e x_2^e x_1^e + (b_4 \cos(x_2^e - x_4^e)) \\ + (b_8 x_1^e \tan(x_2^e) x_1^e)((b_{14} + b_{15} x_2^e)) \\ - (b_{10}^{-1}(b_7 + b_2 x_1^e \tan(x_2^e))(b_4 \sin(x_2^e - x_4^e))) \\ - (b_{10}^{-1}(b_1 b_{11} x_1^{e2} + b_1 b_{12} x_1^{e2} x_2^e)) = 0. \tag{56}$$

8.3 Appendix 3: derivation of Flight Controller No. 3

Deriving the equation of the control inputs u_1 and u_2 in the form of $f(x)$ and $g(x)$, we get

$$u_1 = -\frac{f_2}{g_{21}} - \frac{g_{22}}{g_{21}} u_2 + \frac{v_1}{g_{21}}, \quad u_2 = -\frac{f_1}{g_{12}} - \frac{g_{11}}{g_{12}} u_2 + \frac{v_2}{g_{12}}. \tag{57}$$

$$u_1 = \frac{g_{12}(f_2 - v_1)}{g_{11}g_{22} - g_{12}g_{21}} - \frac{g_{22}(f_1 - v_2)}{g_{11}g_{22} - g_{12}g_{21}}. \tag{58}$$

$$u_2 = \frac{g_{21}(f_1 - v_2)}{g_{11}g_{22} - g_{12}g_{21}} - \frac{g_{11}(f_2 - v_1)}{g_{11}g_{22} - g_{12}g_{21}}. \tag{59}$$

Substituting $v_1 = v_2 = 0$, in (57) and replacing them into the equation of $\dot{x}_3$ and $\dot{x}_4$ in (13), we get

$$\begin{bmatrix} \dot{x}_3 \\ \dot{x}_4 \end{bmatrix} = \begin{bmatrix} f_3 + g_{31} u_1 \\ f_4 \end{bmatrix} = \begin{bmatrix} f_3 + (g_{31})\left(\dfrac{-f_2 - g_{22} u_2}{g_{21}}\right) \\ f_4 \end{bmatrix}. \tag{60}$$

Now substituting expression for $f(x)$ and $g(x)$ in (60) gives the two-dimensional zero-dynamics:

$$\begin{bmatrix} \dot{x}_3 \\ \dot{x}_4 \end{bmatrix} = \begin{pmatrix} \Phi_3 \\ \Phi_4 \end{pmatrix}$$

(see equation below)

$$\begin{pmatrix} \Phi_3 \\ \Phi_4 \end{pmatrix} = \begin{bmatrix} f_3 + (b_{10} x_1)\left(\dfrac{-\left(b_1 b_5 x_1 + b_1 b_{13} x_2 x_1 + b_6 x_3 + x_3 + b_4 x_1^{-1}\cos(x_2 - x_4) + (-b_3 x_1^{-1}\sin(x_2))u_2\right) + \dot{x}_2^{\text{ref}} + k_2(x_2 - x_2^{\text{ref}})}{b_7}\right) \\ x_3 \end{bmatrix}.$$

Chapter 7

Load Alleviation System for Aircraft

7.1   Summary of the contributions

This chapter covers mainly the contribution of active control technique for reducing the gust loading on a flexible aircraft. Light weight aircraft suffers from reduced stiffness for disturbance loads such as gusts. A robust feedforward gust load alleviation system (GLAS) is developed to alleviate the gust loading. The research is focused on designing a combined feedforward/feedback controller to improve performance in reducing the peaks in wing root moments at very short gust lengths. The complex 2 DoF structural load alleviation system has been developed for a flexible aircraft. The detectable wind gust signal was considered as driving excitation factor of the aircraft structure for this study. The feedback part of the load alleviation system has been developed using a robust and optimal control system design techniques in order to augment feedforward part and its robust properties, respectively. While designing the controller via the root locus method, frequency domain requirements were taken into account so that the low frequency dynamics of the aircraft was not affected. The robust performance of designed structural load alleviation system was assessed and results show significant reduction of the wing root bending moments. Reduction of aircraft structural load might offer potential possibility aircraft structural weight savings or increase predicted life time of structure.

7.2   Publication

The work is represented by a publication with modified formatting and follows on the next page.

Short communication

Active gust load alleviation system for flexible aircraft: Mixed feedforward/feedback approach

CrossMark

Mushfiqul Alam [a,*], Martin Hromcik [b], Tomas Hanis [c]

[a] *Department of Measurement, Faculty of Electrical Engineering, Technicka 2, Czech Technical University in Prague, Czech Republic*
[b] *Department of Control Engineering, Faculty of Electrical Engineering, Karlovo Namesti 13, Czech Technical University in Prague, Czech Republic*
[c] *Department of Wind Energy, Building 114, Technical University of Denmark, DK*

ARTICLE INFO

ABSTRACT

Lightweight flexible blended-wing-body (BWB) aircraft concept seems as a highly promising configuration for future high capacity airliners which suffers from reduced stiffness for disturbance loads such as gusts. A robust feedforward gust load alleviation system (GLAS) was developed to alleviate the gust loading. This paper focuses on designing a feedback controller which would improve the robust performance of the feedforward controller in reducing the peaks in wing root moments at very short gust lengths. The simulation results show that when the new feedback compensator is engaged with the feedforward controller, the performance of the GLAS system is improved significantly in terms of reduction in wing root moments for shorter as well as for longer gusts. This reduction in the wing root moment's peak provides potential structural benefits and weight savings.

© 2015 Elsevier Masson SAS. All rights reserved.

1. Introduction

Current state-of-the-art aircraft such as Airbus A380 and Boeing 787 Dreamliner have pushed the limits of efficient conventional tube-wing configuration. As a result the aircraft designers investigate now alternative aircraft configurations such as the Blended Wing Body (BWB) concept. Several projects were undertaken in the European research programmes content such as ACFA (Active Control for Flexible Aircraft) 2020, NACRE (New Aircraft Concepts Research), VELA (Very Efficient Light Aircraft) and ROSAS (Research on Silent Aircraft Concepts) [2,18,15,7].

The transport aircraft BWB research and design efforts can be traced back to the 1980s. A comprehensive documentation of the US research efforts on the design of BWB subsonic transport aircraft, corresponding design issues and constraints, advantages and drawbacks existing with such configurations, as well as results from wind tunnel tests are presented in [17]. The research progress is demonstrated starting from a preliminary design study in 1988 for novel configurations up to the highly efficient Boeing BWB-450 baseline aircraft. Basically, three generations of BWB configurations are documented which were successively improved.

The European VELA project aimed at the development of skills, capabilities and methodologies required for the design and optimization of civil flying wing aircraft. Within VELA two baseline flying wing BWB configurations were developed [24]. The project was focused on development of aerodynamic and control derivatives and their impact on flight stability. In addition low speed tunnel tests were performed while comparing the results from the experiment with the predictions made using CAD and CFD software tools. Special setup of dynamic tests was dedicated to the validation of the effects of deflecting control surfaces and other dynamic characteristics of flying wing configurations. Optimization techniques were then applied to maximize the efficiency of these configurations, varying parameters such as chord length, twist angle and airfoil section shape [8].

Later on NACRE project was undertaken to drive the development of the key capabilities required for the improvement of the novel aircraft concepts from the experience gained in VELA. The NACRE project was broken down to mainly four work packages; first, novel aircraft concept; second, novel lifting surfaces; third, novel power plant installation and fourth, novel fuselage. The key technical achievements can be classified in two key areas: (1) Multidisciplinary Design and Analysis Capabilities for Components, which includes, (a) Open Rotor propulsion integration for noise shielding; (b) Powered Tail innovative integrated design & analysis; (c) Natural Laminar Flow wing design and transition prediction and (d) Flying wing configuration design and multidisciplinary assessment [14]. (2) Experimental Validation & Testing Techniques, which includes, (a) Rear engine integration (Aerodynamics & Noise improvement); (b) High-Energy absorption; (c) Fly-
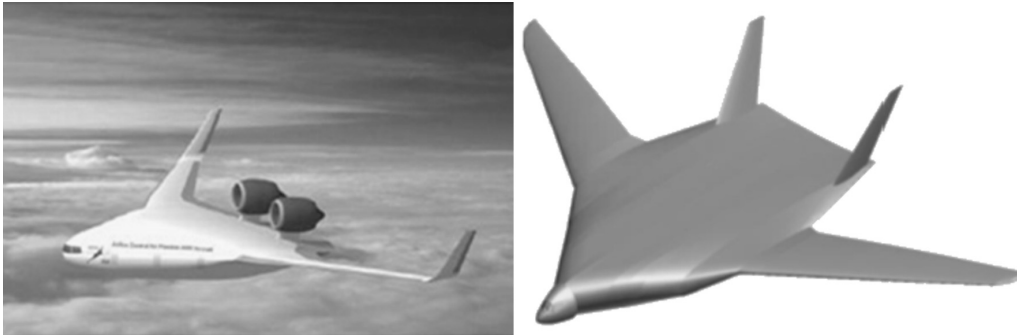
Fig. 1. Visualization of two selected BWB concepts ACFA2020 (left) [2] and NACRE (right) [3].

ing Wing cabin evacuation; (d) Innovative evaluation platform development [3,10,1].

Finally, within the ACFA2020 the predesign of a 450 passenger BWB aircraft is finalized achieving the major aircraft efficiency objectives regarding reduced fuel consumption and external noise. The project further studied robust as well as adaptive multi-channel control architectures for loads alleviation and improvement of ride comfort and handling qualities of BWB type aircraft. One of the main goals of the project, however, was to investigate the system's aeroelastic properties with respect to modern control design methodologies. Thereby, the potential in structural load reduction, improving of ride comfort and attainable handling qualities were main drivers [9].

The dynamical models of the finalized BWB aircraft were developed for carrying out the controller design. The models were generated based on a refined Finite Element Model (FEM) and aerodynamic data [2]. Fig. 1 shows the two above mentioned finalized BWB concepts within the European projects.

For future high capacity airliners, the BWB concept appears to be highly promising. The aircraft configuration presents a compact lifting body with significantly increased lift-to-drag ratio with obvious environmental (lower noise level and CO_2 emissions) and economic (lower fuel consumption, reduced operational expenses) consequences [17,20,23,21]. The lightweight BWB structure suffers however from reduced stiffness compared to the classical tube-wing configuration.

This aspect of reduced stiffness is further emphasized if thin lifting surfaces and the use of composite materials for aircraft structures are considered, leading to light weight flexible structures. When this type of aircraft passes through the turbulent atmosphere, it develops significant structural vibrations. Aircraft motion of this kind results in reduction of structural lifetime due to large dynamic loads and the consequent level of stresses. The amplitude of the aircraft's structural response, caused by gust excitation depends upon two factors. First, the amount of energy transferred from the gust disturbance to the structural modes; and second, the dissipation of any energy absorbed from gust by active structural damping. In addition, when the amplitude of the response of the elastic motions is comparable to that of the rigid body motion, an interaction or coupling of the rigid body energy and the elastic energy can appear leading to detriment of the flying qualities of the aircraft [19,22].

Current Gust Load Alleviation systems work primarily on the error feedback principle [5,30,33]. The first peak in the wing root moments (induces maximum load in the construction) determines the required sizing of the wing root joint reinforcement. Potential weight savings can be realized if the reduction in wing root moments is achieved. What is of special concern is therefore the 1st peak's reduction in the wing root moments, which is regarded as non-achievable by purely feedback solution [27]. Therefore com-
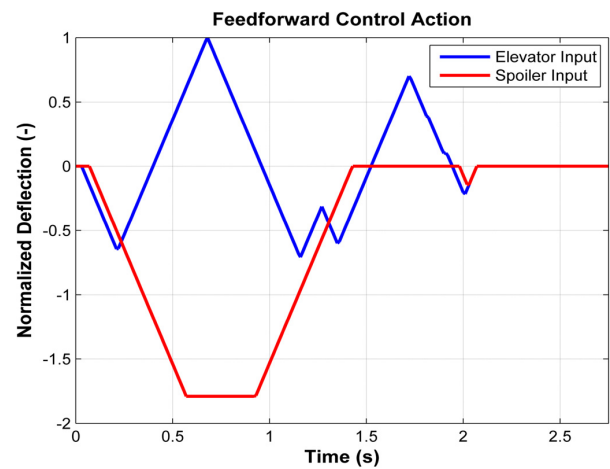

Fig. 2. Normalized feedforward control inputs [29].

bined feedforward plus feedback control can significantly minimize structural deflection due to air turbulence such as gusts [31,28]. If the sensors are placed smartly they could measure the r.m.s. (root mean square) vertical acceleration (along z-axis) at a number of locations on the aircraft. In order to precisely determine the effects of the wing bending relative to the center of gravity (CG) of the aircraft sensors are to be placed at the CG, wingtip right node and wingtip left node in principle. A related detailed treatment on optimal placement of sensors for this problematic issue is outlined in [12,16,25]. The acceleration of the wing relative to the CG is defined as η_z law (see Section 3.1) which actually gives the measure of wing bending, induced by a gust for instance.

To alleviate this gust loading, a triggered feedforward (FF) control strategy, see Fig. 2, was elaborated at EADS Innovation Works, Munich. Fig. 2 shows the normalized control signal with respect to the maximum elevator deflection. A pre-computed control sequence for ailerons and spoilers is triggered once the aircraft hits a gust, which is detected by an alpha-probe (angle-of-attack probe) placed at the node of the aircraft [29]. The pre-defined FF control sequence was designed to be robust with respect to different aircraft mass cases, altitudes, Mach numbers and gust lengths.

This FF control approach appears very efficient, according to high-fidelity simulations [29] for alleviation of the wing root bending and torsional moments for long gusts especially, which are the "sizing gusts" in fact – they produce largest impacts on the construction. However, a price paid for this are slightly increased wing root moments for shorter gusts, compared to the non-controlled
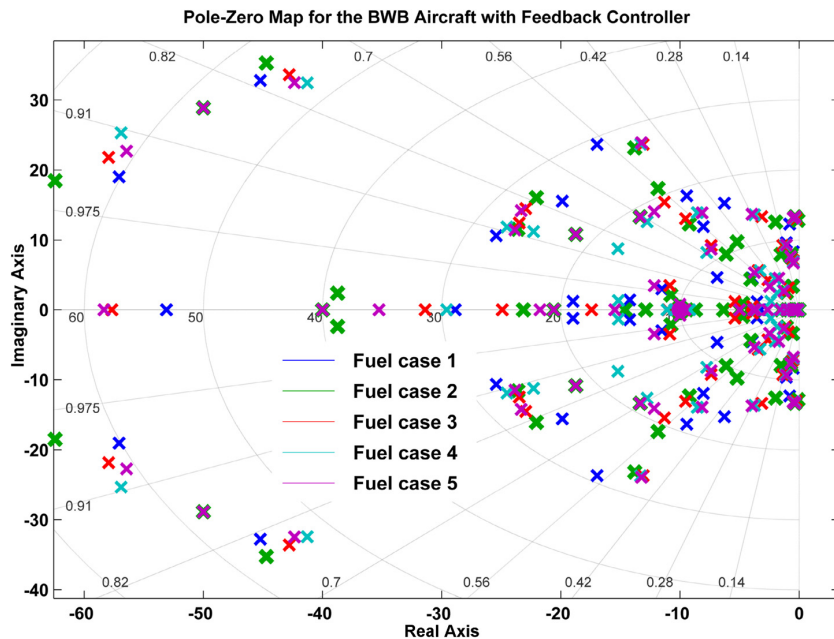
Fig. 3. Pole-zero plots of the original BWB aircraft with the stabilizing $\mathcal{H}_\infty$ feedback controller [33].

case (bear in mind that the control sequence is pre-calculated and fixed for any gust length). These short gust cases are not the sizing ones, and the overall first-peak value throughout the gust length cases is significantly reduced, still this effect can be regarded as undesirable and disturbing.

Earlier attempts were made in [4] to improve the performance of the GLAS using linear quadratic regulators (LQR). The controller design and simulation showed promising improvement by reducing the wing root moments. However this type of controller was constrained by the difficulties of state estimation. Generally BWB aircraft are large systems with significantly high number of unmeasurable flexible states and, as a result it is difficult to implement full-order optimal controllers in this case.

Therefore a different concept is proposed in this paper. It is suggested to use additional simple feedback loops that would work along with the triggered FF GLAS system which would improve the FF control sequence performance over shorter gust lengths and further improve the performance for "sizing gusts". The classical SISO control design methods were investigated.

The paper is organized in the following order. Section 2 presents a discussion on the development and generation of the aircraft's dynamic model. Section 3 describes the detailed design of the control law. Section 4 provides a detailed comparative analysis on the improved results. Section 5 contains final concluding remarks.

2. Dynamic modeling

2.1. Aircraft model

The aircraft model used for loads analysis and design and validation of the GLAS is based on aerodynamic and structural data of the BWB configuration NACRE developed in the European project NACRE and modified in ACFA2020 [33]. The aircraft model was not originally developed for dynamic analysis. Necessary modifications were made so that the dynamic analysis could be performed. Components such as cockpit, elevator and wing's leading edge, engine pylons and structures were added as concentrated

Table 1
Mass variation cases.

No. of cases	Fuel (as a fraction of full load)
1	1/16th
2	1/8th
3	1/4th
4	1/2nd
5	3/4th
6	1

point masses [33]. Non-structural masses of systems and equipment as well as operational masses were integrated into the structural model. Finally, various passenger/payload and fuel configurations were modeled with concentrated masses and also integrated into the structural model of the NACRE configuration. Aerodynamic polars, damping derivatives, and control surface derivatives were provided by the NACRE project for various mass cases and cruise speeds. For the gust load analysis six different varying fuel mass cases were considered as shown in Table 1.

The phugoid mode of the aircraft is not considered, the analysis is focused on short period model only. The considered aircraft, NACRE aircraft, was statically unstable in large regions of mass and flight envelope. Therefore, the flight control system required artificial pitch stabilization. The original aircraft model was stabilized by a robust (with respect to fuel/mass cases, altitude, and velocity) feedback $\mathcal{H}_\infty$ controller [13,26,32]. Artificial pitch stiffness is achieved by feedback of the vertical CG load factor η_z to the elevator. In order to achieve neutral pitch stability this feedback is done via a PI controller [19,6]. An additional pitch damper (i.e. feedback from pitch rate q to the elevators) allows placement of the poles of the short period mode [33]. The original NACRE short period model has 20 states which include the rigid body short period mode and a number of flexible modes. By adding the stabilizing $\mathcal{H}_\infty$ controller, the overall state count increased to sixty. The pole-zero map of the stabilized aircraft is shown in Fig. 3.
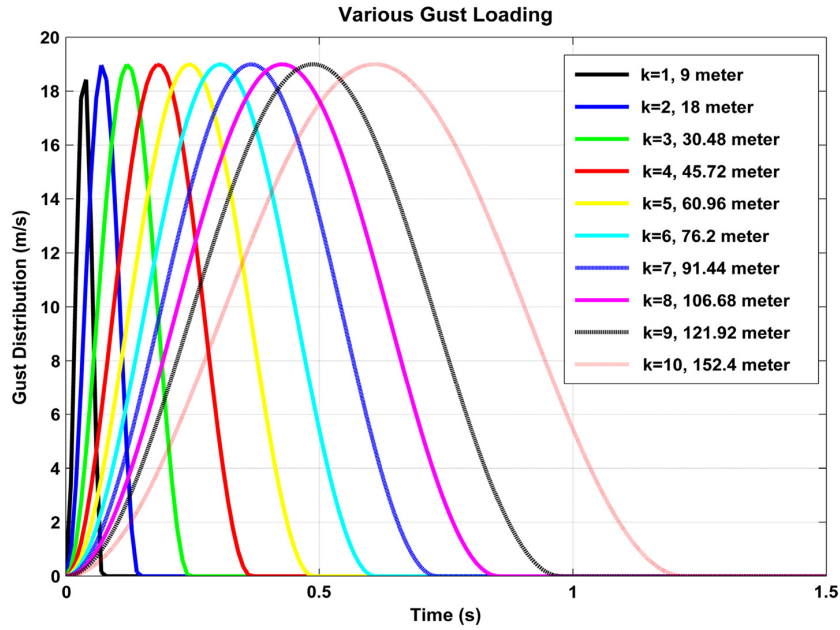
Various Gust Loading

Fig. 4. Gust distribution of various gust lengths.

2.2. Gust modeling

Vertical wind gusts are traditionally modeled as a function of $(1 - \cos\beta)$ defined by the equation

$$x_g(t) = \frac{a}{T}\left(1 - \cos(2\pi/T)t\right) \tag{1}$$

where "T" is the duration of the gust, which is defined by

$$T = k/U_o \tag{2}$$

"k" is the gust length and U_o is the aircraft cruise speed. 10 different gust lengths were chosen for the simulation as shown in Fig. 4.

3. Control law design

3.1. η_z law

The wing bending of the flexible aircraft was assessed by attaching sensors that measure the r.m.s. values of vertical acceleration at a number of locations on the aircraft. For precise determination of the effects of wing bending, the sensors should be placed at the (CG), wingtip node right and wingtip node left. Details description for the placement of the sensors can be found in [12]. The acceleration of the wing relative to the CG is defined as η_z law, and it is calculated by:

$$\eta_{z_{law}} = \overbrace{\frac{1}{2}\eta_{z_{wingtip}}}^{left\ node} + \overbrace{\frac{1}{2}\eta_{z_{wingtip}}}^{right\ node} - \eta_{z_{CG}} \tag{3}$$

3.2. Control design

Fig. 5 shows the primary control surfaces of the NACRE aircraft. The non-linear models of the actuators were approximated by 2nd order linear model. The sensor delays were estimated by 2nd order Pade approximations. The FF control sequence works simultaneously with Spoiler 1 and 2 and Elevator 1 and 2.

In case of a gust disturbance, the proposed concept was to feedback the η_z law to the Flap 1 (inner aileron) and Flap 2 (center aileron), which would work together with the FF controller. Fig. 6 shows the control block diagram for the new control strategy.

In such a way, a two-stage feedback control law is devised; a separate control augmentation system (CAS) taking care of the flight dynamics primarily and the feedback active damping system (the newly designed SISO controllers) taking care — jointly with the triggered FF GLAS system — of the gust performance improvement. Such control structure has obvious advantages. First regarding tuning the controllers (both parts can be designed/tuned independently). Second, in the flight testing the newly designed controller can be turned on/off while keeping the aircraft under full control. Third, the point of flight safety is important, loss of such an add-on simple feedback controller is not a critical failure and would not take the aircraft out of control.

Flap 1 controller design

The first wind bending mode from $\eta_{z_{law}}$ to Flap 1 (inner aileron) lies between 2–3 Hz. $\eta_{z_{law}}$ controller was designed using the root locus method in MATLAB [11]. Eq. (4) shows the Flap 1 controller transfer function. In frequency domain the channel from Flap 1 to $\eta_{z_{law}}$ was already damped by 5–7 dB by the stabilizing $\mathcal{H}_\infty$ controller [26]. While designing the controller using root locus method it was ensured that the lower frequency of the aircraft is not affected.

$$\eta_{z_{law}} \text{ to Flap } 1 = \frac{6}{s^2 + 12s + 20} \tag{4}$$

The designed controller is a lowpass filter with approximately 1 Hz bandwidth (Fig. 7).

Flap 2 controller design

The first wind bending mode from $\eta_{z_{law}}$ to Flap 2 (center aileron) lies between 6–10 Hz. $\eta_{z_{law}}$ controller was designed using the root locus method. Eq. (5) shows the transfer function of the designed $\eta_{z_{law}}$ controller.
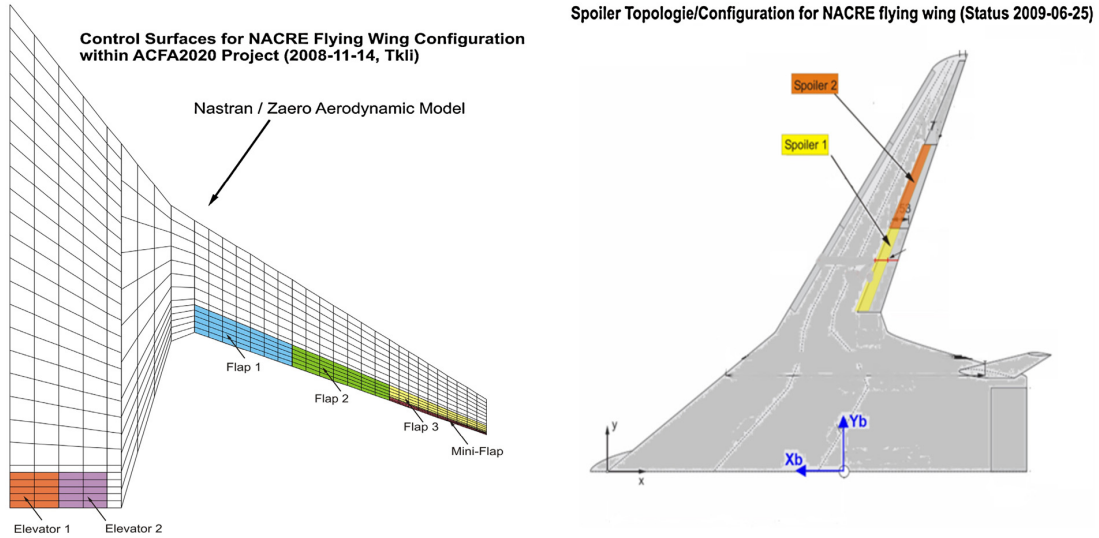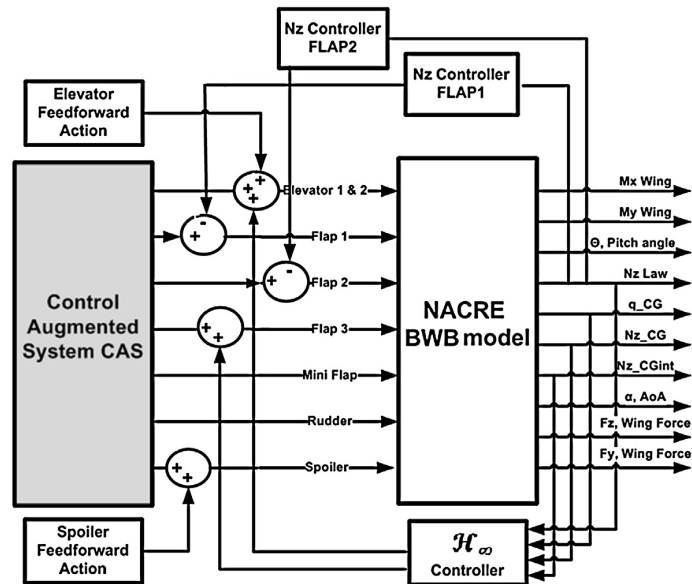
73

Fig. 5. Control surfaces of NACRE aircraft.

Fig. 6. New SISO control strategy by feeding back η_z law to Flap 1 and Flap 2.

$$\eta_{z_{law}} \text{ to Flap } 2 = \frac{0.1s + 1}{s + 1} \tag{5}$$

A design requirement again is that the low frequency region is left untouched. Fig. 8 shows the frequency response of the $\eta_{z_{law}}$ controller over different mass cases. The designed controller is a first order filter with one zero and one pole.

4. Simulation results

Different mass cases (6 mass cases) were considered along with the gust lengths (10 gust lengths). The rate limiters and the saturation point of Flap 1 and Flap 2 were also taken into account during the simulation. Flap 1 and Flap 2 were constrained by rate limiter at ± 40 deg/s and saturation point at $\pm 25°$. The gust was used as an exogenous disturbance input signal to the flight dynamics model (to the angle of attack channel, more precisely).

M_x is defined as the wing root bending moment and M_y is defined as the wing root torsional moment. Fig. 9 to Fig. 11 show the response of the wing root moments M_x and M_y for the gust cases $k = 1$, 5 and 10 (other gust cases are shown in Appendix A). Simulations were done using SIMULINK [11]. All other gust cases had similar responses. The wing root moment values were normalized with respect to the maximum value of M_x & M_y which occurs at the longest gust case ($k = 10$). The cyan line corresponds to the original aircraft with only stabilizing $\mathcal{H}_\infty$ controller engaged; blue line corresponds to aircraft with stabilizing $\mathcal{H}_\infty$ controller engaged with only FF control action; finally the red line corresponds to the aircraft with stabilizing $\mathcal{H}_\infty$ controller engaged with FF control action and newly designed $\eta_{z_{law}}$ controller to Flap 1 and 2 with $\mathcal{H}_\infty$ controller engaged.

Observing Fig. 9, comparing the cyan and blue lines, the triggered FF action at short gust lengths ($k = 1$) artificially gives rise
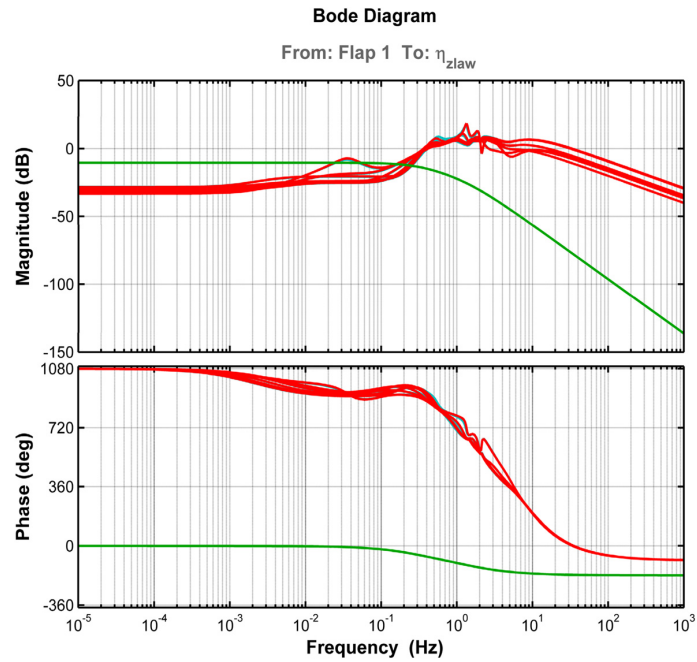
Fig. 7. Frequency response for different mass cases for (1 to 6) using $\eta_{z_{law}}$ to Flap 1. Cyan shows the response of original aircraft with stabilizing $\mathcal{H}_\infty$ controller engaged. Red shows the response with new Flap 1 controller engaged. Green shows the controller frequency response. (For interpretation of the references to color in this figure legend, the reader is referred to the web version of this article.)

Fig. 8. Frequency response for different mass cases for (1 to 6) using $\eta_{z_{law}}$ to Flap 2. Cyan shows the response of original aircraft with stabilizing $\mathcal{H}_\infty$ controller engaged. Red shows the response with new Flap 2 controller engaged. Green shows the controller frequency response. (For interpretation of the references to color in this figure legend, the reader is referred to the web version of this article.)
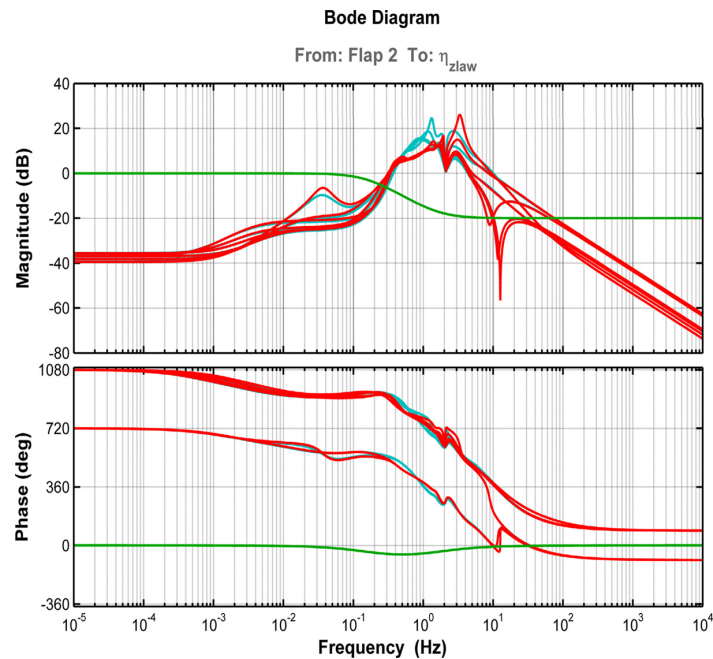
to first peak in wing bending and torsional moments compared to free, uncontrolled aircraft (FF control action disengaged). This is the undesired effect of the FF control sequence at short gusts. Fig. 10 and Fig. 11 show that the triggered FF action at longer gust lengths $k \geq 5$, for the "sizing gusts", significantly reduces the

first peak in wing bending and torsional moments, compared to the original aircraft. It is the key feature of the triggered FF GLAS system to reduce the 1st peak in the wing root moments.

The reduced performance of the FF control at shorter gust lengths can be attributed to the spoiler deflections. Now being
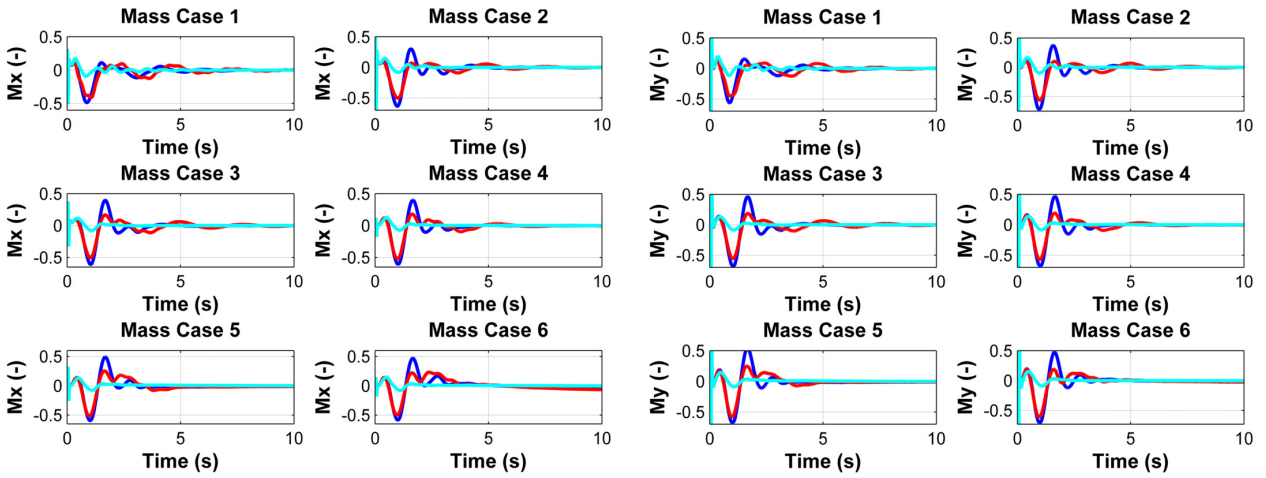
Fig. 9. Normalized wing root moment, M_x and M_y at gust length 9 m ($k = 1$) for different mass cases using SISO controller. (For interpretation of the references to color in this figure legend, the reader is referred to the web version of this article.)

Fig. 10. Normalized wing root moment, M_x and M_y at gust length 60.96 m ($k = 5$) for different mass cases using SISO controller. (For interpretation of the references to color in this figure legend, the reader is referred to the web version of this article.)

Fig. 11. Normalized wing root moment, M_x and M_y at gust length 152.4 m ($k = 10$) for different mass cases using SISO controller. (For interpretation of the references to color in this figure legend, the reader is referred to the web version of this article.)
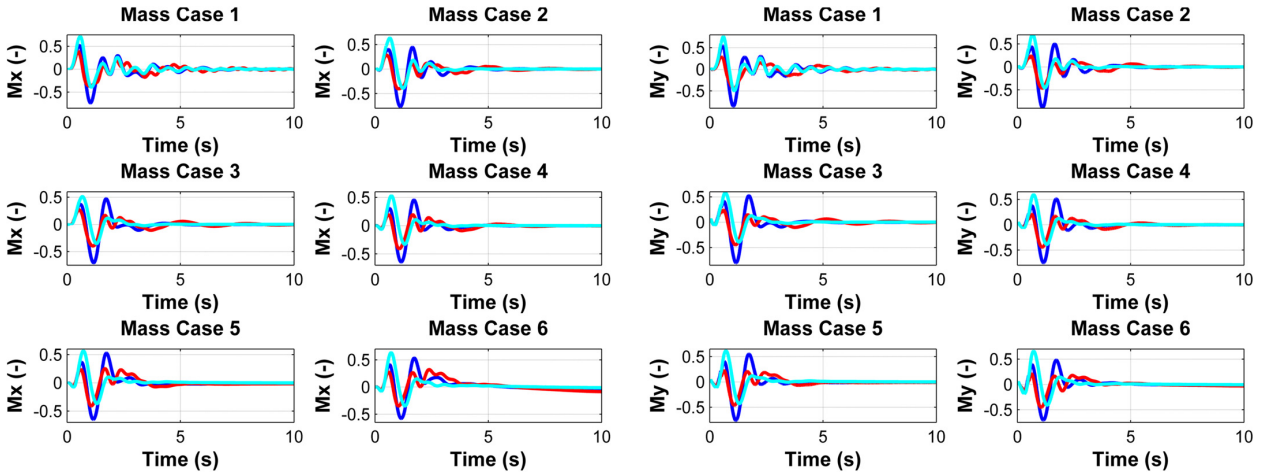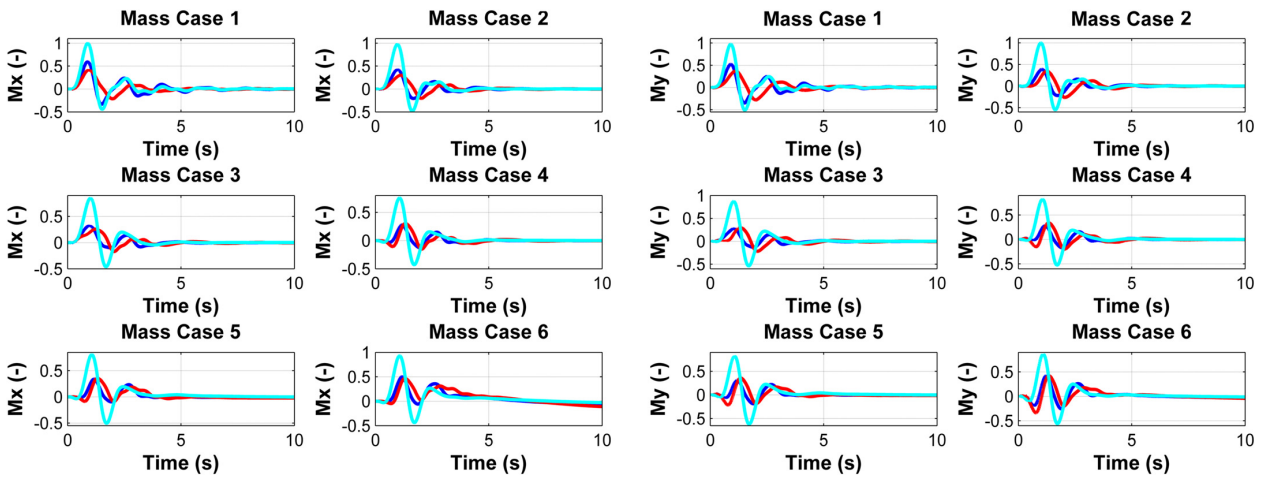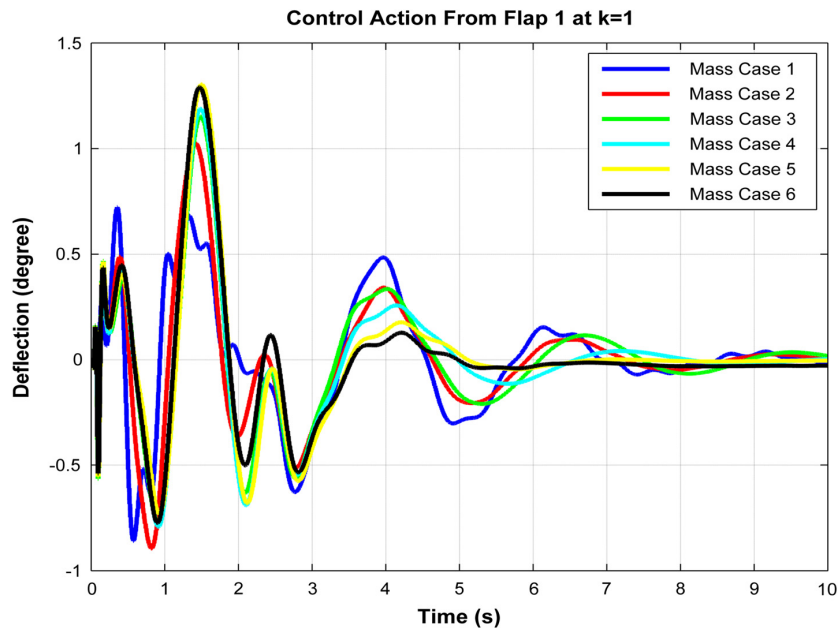
Fig. 12. Flap 1 control action at gust length $k = 1$.
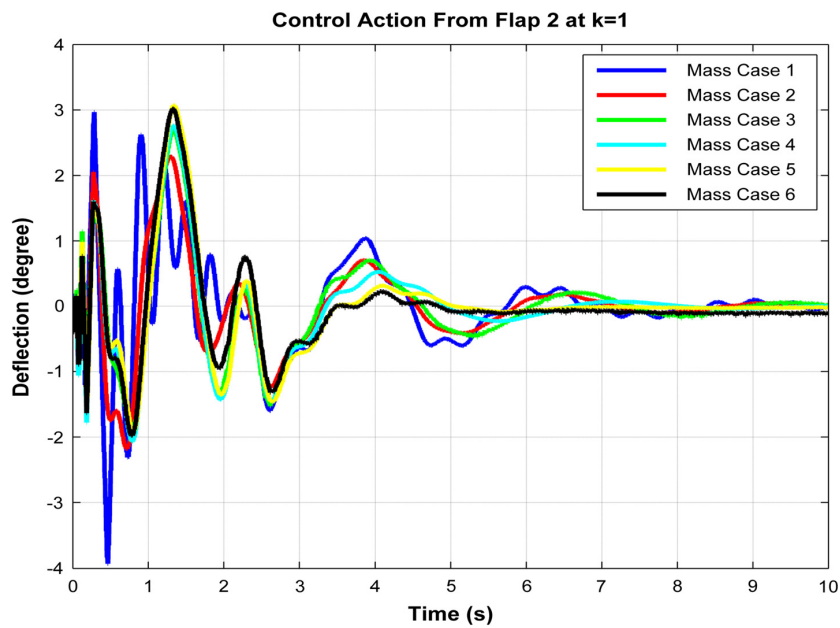
Fig. 13. Flap 2 control action at gust length $k = 1$.

Flap 1 and Flap 2 positioned right below Spoiler 1 and 2, it makes these control surfaces most effective to improve the performance. If Fig. 2 is considered for FF control deflection, it can be seen that Spoilers 1 and 2 deflect with a negative angle (which means the spoilers deflect upward) this produces a downward for force on the wing. This downward force on the wing gave rise to wing root bending moment, M_x, and wing root torsional moment, M_y.

Of course the deflection of the spoilers and elevators and flaps during the flight is aerodynamically inefficient due to increased drag. However the deflections are made for a very short period of

time therefore the trade-off between drag and reduction of wing root moment is always beneficial.

When the newly designed feedback controller is engaged jointly with the FF triggered GLAS compensator, the simulation results show significant improvements in reducing the first peak in wing root bending moment and wing root torsional moments. From Fig. 9 to Fig. 11 (blue and red line), it can be appreciated that the new controller improves the FF control performance by reducing the 1st peak at low gust lengths $k = 1$ which was the primary design goal. In Fig. 10 and Fig. 11 it can be observed however that even for longer gust lengths $k \geq 5$ the newly designed controller

enhances the FF controller's performance by further reducing the wing root moments. Tables B.1 and B.2 (in Appendix B) provide detailed values regarding this improvement in the performance.

Fig. 12 and Fig. 13 show the resulting control deflection of Flap 1 and Flap 2. It can be seen that both the flap deflections start with a negative deflection and slowly move to higher positive values (which means the flaps deflect down), this produces a counter upward force on the wing which eventually reduces the wing root bending moment M_x and wing root torsional moment, M_y. The figures show the situation for the shortest gust load, the control action for other gust cases are similar.

One other important fact to consider is that the performance of the controller gets better from mass case 6 to 1. This means the performance of the newly designed controller gets better from high-mass case to low-mass case. This is practically beneficial due to the fact that during the flight the aircraft gradually loses weight due to the fuel burn.

The simulation results from Fig. 9 to Fig. 11 show therefore that by adding a feedback controller to the feedforward GLAS system, significantly improved performance is achieved in terms of reduction in wing root moments at shorter gust lengths as well as longer gust lengths. The feedforward controller gives a significant reduction in the wing root moments for gusts longer than 60.9 m (the sizing ones), while the additional feedback controller with Flap 1 and Flap 2 targets primarily the shorter gusts and has marginal positive effect on long gusts as well. On an average by adding the newly designed feedback controller the performance of the FF GLAS was improved by 39% in case of wing root bending moment M_x and 36% in case of wing root torsional moment M_y.

The 1st peak of wing root moments indicates the maximum load in the wing root constructions which provides the required sizing of the reinforcement needed at the wing root joints. Therefore the proposed improved GLAS system indicates a potential possibility in structural weight savings, in other words cost reduction and economic benefits.

5. Conclusions

The newly proposed control method improves the robustness performance of a previously developed feedforward gust load alleviation system. The proposed SISO controller provides a significant performance improvement to the feedforward controller at short gust lengths especially. While designing the controller via the root locus method, frequency domain requirements were taken into account so that the low frequency dynamics of the aircraft was not affected. The first peak in the wing root moments was attenuated significantly which provides a potential possibility for structural weight savings for wing root joint reinforcement or increase in predicted life time of structure. In this research work only wing root moments were analyzed. The future works should carefully investigate and verify the moment distribution along the wing span.

Conflict of interest statement

None declared.

Acknowledgement

Appendix A

Fig. A.1 and Fig. A.2 show the aircraft's wing root moment at gust cases $k = 2, 9$.

Appendix B

The reductions in the peaks of the system are summarized in Tables B.1 and B.2. The 1st column of the first peak represents the percentage improvement in the performance using feedforward controller compared to the original aircraft response without the FF controller engaged. And it is calculated by

% Improvement using FF controller
$$= \frac{peak\ of\ original\ aircraft - peak\ i\ using\ FF}{peak\ of\ original\ aircraft} * 100 \qquad (B.1)$$
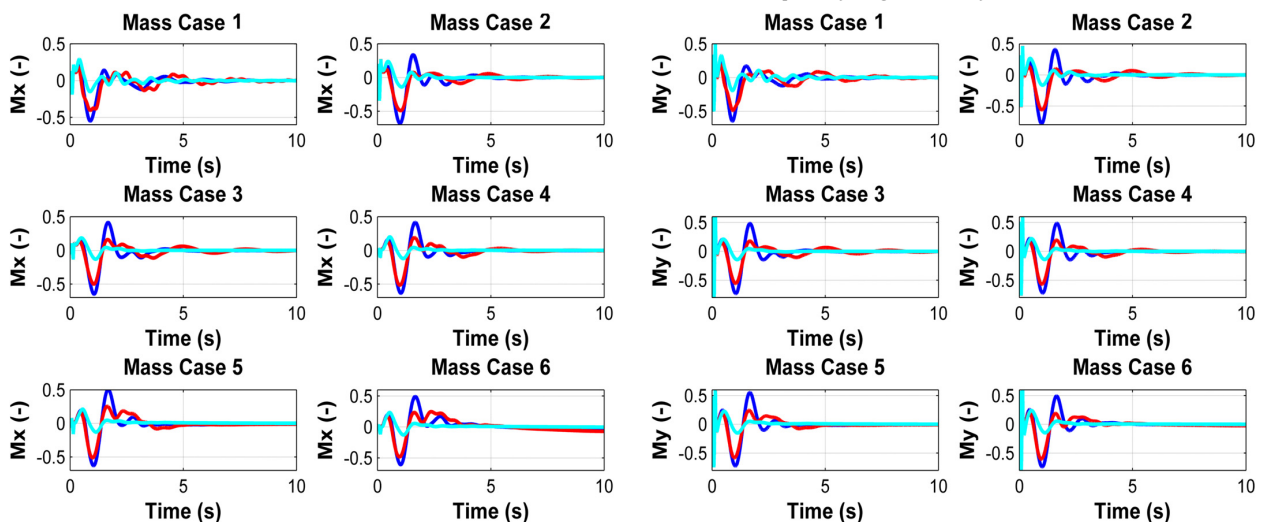

Fig. A.1. Normalized wing root moment, M_x and M_y at gust length 18 m ($k = 2$) for different mass cases using SISO controller.
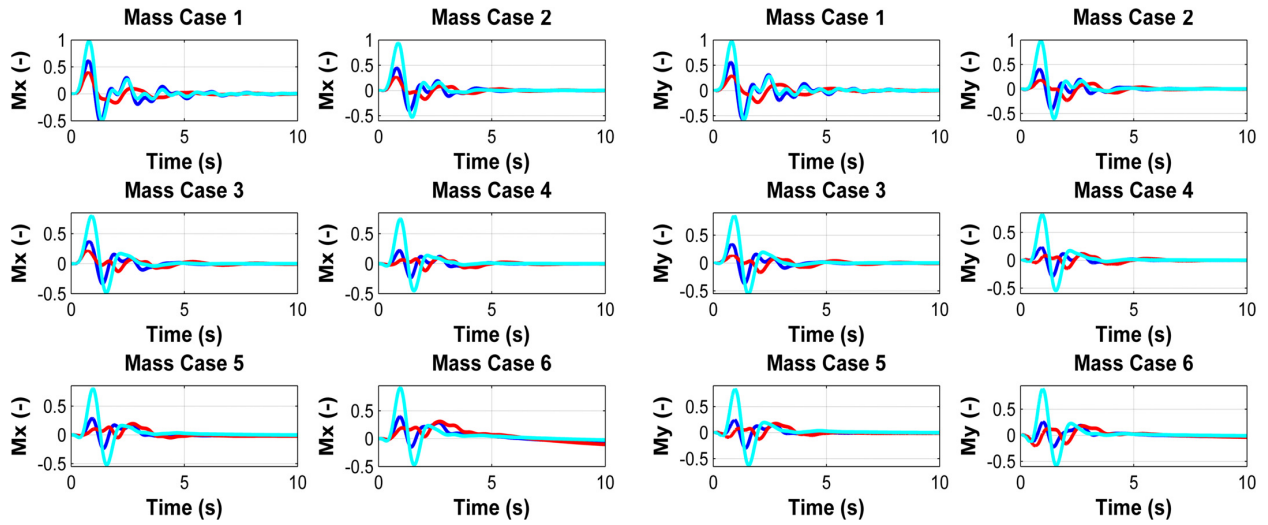
Fig. A.2. Normalized wing root moment, M_x and M_y at gust length 121.92 m ($k = 9$) for different mass cases using SISO controller.

Table B.1
Comparison of peak reduction in wing root moment M_x between original aircraft, using feedforward action and feedforward action with SISO controllers.

Mass case	$K = 1$				$K = 2$				$K = 3$			
	1st peak		2nd peak		1st peak		2nd peak		1st peak		2nd peak	
	FF (%)	SISO (%)	FF (%)	SISO (%)	FF (%)	SISO (%)	FF (%)	SISO (%)	FF (%)	SISO (%)	FF (%)	SISO (%)
1	32.49	2.82	−434.51	21.54	25.40	16.82	−268.15	24.90	25.63	15.29	−178.64	31.13
2	43.91	6.42	−700.65	21.06	29.73	27.15	−397.74	27.90	31.68	14.43	−240.02	34.45
3	2.22	27.90	−678.94	17.14	20.81	10.23	−418.63	23.01	17.84	10.28	−254.08	28.32
4	18.56	−0.15	−779.63	13.79	6.46	32.98	−428.14	18.71	27.29	15.20	−262.97	23.65
5	−1.49	0.45	−680.15	12.86	6.22	10.89	−411.20	18.39	19.32	13.11	−228.26	23.36
6	2.64	2.93	−669.94	14.79	12.88	17.88	−375.07	20.50	21.70	10.49	−222.89	25.72

Mass case	$K = 4$				$K = 5$				$K = 6$			
	1st peak		2nd peak		1st peak		2nd peak		1st peak		2nd peak	
	FF (%)	SISO (%)	FF (%)	SISO (%)	FF (%)	SISO (%)	FF (%)	SISO (%)	FF (%)	SISO (%)	FF (%)	SISO (%)
1	26.10	22.86	−120.12	34.58	27.55	23.61	−87.39	49.82	28.97	30.25	−63.79	59.96
2	33.42	27.88	−146.97	39.79	36.99	24.33	−95.27	47.38	37.53	31.10	−58.83	55.29
3	22.65	25.57	−154.54	37.18	28.33	25.59	−99.58	43.80	32.71	29.16	−60.75	51.17
4	34.56	27.29	−154.87	29.78	42.53	36.44	−94.74	36.31	50.82	44.01	−51.84	155.56
S	27.21	21.02	−131.44	30.07	35.65	30.71	−76.40	36.92	44.17	37.22	−36.57	46.15
6	27.66	17.63	−122.55	32.09	34.83	184.85	−66.02	155.54	42.43	22.88	−25.18	50.68

Mass case	$K = 7$				$K = 8$				$K = 9$			
	1st peak		2nd peak		1st peak		2nd peak		1st peak		2nd peak	
	FF (%)	SISO (%)	FF (%)	SISO (%)	FF (%)	SISO (%)	FF (%)	SISO (%)	FF (%)	SISO (%)	FF (%)	SISO (%)
1	32.26	34.23	−43.24	67.45	37.14	35.24	−5.76	68.46	37.14	35.17	−5.76	68.35
2	42.62	34.53	−28.63	62.31	52.28	34.55	23.91	56.37	52.26	40.28	23.91	57.05
3	39.70	32.36	−28.43	59.65	52.99	32.68	31.09	60.06	52.99	41.31	31.09	61.79
4	58.68	52.57	−16.25	55.90	70.82	50.71	47.68	51.68	70.82	52.13	47.68	51.25
5	52.46	158.03	−3.67	55.66	64.48	92.93	54.83	71.53	64.48	31.73	54.83	78.73
6	49.31	22.09	8.61	69.25	57.05	20.23	68.50	33.28	57.05	21.13	68.50	30.49

Mass case	$K = 10$			
	1st peak		2nd peak	
	FF (%)	SISO (%)	FF (%)	SISO (%)
1	39.86	31.09	25.14	36.03
2	56.83	28.45	57.12	2.32
3	61.96	20.30	78.70	−70.30
4	63.32	−8.59	70.71	−1.06
5	57.58	−3.26	81.34	7.51
6	46.24	6.58	82.91	134.08

Table B.2

Comparison of peak reduction in wing root moment M_x between original aircraft, using feedforward action and feedforward action with SISO controllers.

Mass case	$K = 1$				$K = 2$				$K = 3$			
	1st peak		2nd peak		1st peak		2nd peak		1st peak		2nd peak	
	FF (%)	SISO (%)	FF (%)	SISO (%)	FF (%)	SISO (%)	FF (%)	SISO (%)	FF (%)	SISO (%)	FF (%)	SISO (%)
1	13.69	15.87	−393.75	336.02	15.18	30.58	−223.19	24.37	18.08	27.41	−153.37	28.80
2	0.09	31.30	−644.70	22.19	19.13	36.59	−373.68	28.65	25.57	26.79	−238.35	33.95
3	0.00	29.67	17.10	18.11	2.07	28.03	−587.31	43.72	11.81	22.94	464.24	29.53
4	0.00	0.00	−764.34	15.31	−1.32	9.61	−415.59	21.67	14.40	21.22	−176.90	26.75
5	0.00	0.00	−704.76	15.30	2.84	12.63	−378.85	19.88	8.79	17.98	−177.39	25.07
6	0.00	0.00	−787.75	14.06	13.30	15.28	−397.06	20.37	13.22	6.84	−242.87	23.50

Mass case	$K = 4$				$K = 5$				$K = 6$			
	1st peak		2nd peak		1st peak		2nd peak		1st peak		2nd peak	
	FF (%)	SISO (%)	FF (%)	SISO (%)	FF (%)	SISO (%)	FF (%)	SISO (%)	FF (%)	SISO (%)	FF (%)	SISO (%)
1	22.19	39.80	−100.89	32.94	28.09	0.00	−72.52	0.00	28.45	46.98	−52.32	60.36
2	31.15	43.19	−35.41	39.29	37.41	46.19	−95.13	47.76	44.36	46.34	−57.45	56.56
3	20.55	36.55	−161.62	37.65	28.99	41.60	−104.24	44.23	38.98	35.75	−63.17	51.92
4	26.31	36.08	−153.61	33.74	36.96	44.09	−93.76	40.68	48.99	52.83	−50.67	48.78
5	22.39	35.09	−132.24	32.28	34.17	43.66	−76.76	39.08	47.24	50.02	−36.74	47.67
6	27.72	34.52	−134.62	29.59	40.13	46.15	−73.24	35.93	53.29	47.91	−29.28	44.78

Mass case	$K = 7$				$K = 8$				$K = 9$			
	1st peak		2nd peak		1st peak		2nd peak		1st peak		2nd peak	
	FF (%)	SISO (%)	FF (%)	SISO (%)	FF (%)	SISO (%)	FF (%)	SISO (%)	FF (%)	SISO (%)	FF (%)	SISO (%)
1	35.03	48.71	−34.40	71.70	43.06	47.24	1.34	63.19	43.06	48.10	1.34	59.10
2	47.33	50.27	−25.55	65.23	59.25	50.20	30.12	47.06	59.23	55.36	30.12	44.58
3	41.81	46.50	−28.53	60.86	60.22	46.96	33.59	59.69	60.22	59.72	33.59	54.64
4	56.99	62.62	−14.79	59.76	71.82	51.11	47.48	53.43	71.82	51.95	47.48	48.05
5	57.20	45.05	−3.55	59.41	70.61	29.05	52.48	63.61	70.61	29.64	52.48	57.31
6	64.93	36.55	6.29	59.12	70.89	30.45	62.01	29.21	70.89	31.06	62.01	7.14

Mass case	$K = 10$			
	1st peak		2nd peak	
	FF (%)	SISO (%)	FF (%)	SISO (%)
1	46.55	29.16	31.09	20.46
2	61.31	11.01	60.16	−21.74
3	68.47	−7.24	75.63	−65.87
4	65.02	−18.48	67.78	13.44
5	61.70	−13.84	69.73	−13.87
6	50.74	1.09	54.51	40.49

Performance improvement using the SISO controller is presented in the 2nd column and it is calculated by

$$\% \, Improvement \, using \, SISO \, controller$$
$$= \frac{peak \, using \, FF - peak \, i \, using \, SISO}{peak \, using \, FF} * 100 \qquad (B.2)$$

The negative values in the tables mean that there is a rise in the peak than expected, meaning deterioration in the performance. And the positive value tells the percentage improvement in the performance.

Appendix C. Supplementary material

Supplementary material related to this article can be found online at http://dx.doi.org/10.1016/j.ast.2014.12.020.

References

[1] A. Abbas, J.d. Vicente, E. Valero, Aerodynamic technologies to improve aircraft performance, Aerosp. Sci. Technol. 28 (1) (2013) 100–132.

[2] ACFA 2020 Consortium, Active control of flexible 2020 aircraft (ACFA 2020), EU FP7 project No. 213321, URL: http://www.acfa2020.eu, last retrieved: Sep. 8th, 2011.

[3] M. Aikawa, K. Arai, M. Arnould, K. Takahashi, H. Utsunomiya, NACRE update and extension project, in: Frontiers in Nuclear Structure, Astrophysics, and Reactions – Finustar, 2006.

[4] M. Alam, Combined feedforward/feedback gust load alleviation control for highly flexible aircraft, in: Proceedings of 2014 PEGASUS-AIAA Student Conference, Prague, 2014.

[5] N. Aouf, B. Boulet, R. Botez, Robust gust load alleviation for a flexible aircraft, Can. Aeronaut. Space J. 46 (3) (2000) 131–139.

[6] R. Brockhaus, Flugregelung, Springer DE, 2001.

[7] L. Cambier, N. Kroll, MIRACLE – a joint DLR/ONERA effort on harmonization and development, Aerosp. Sci. Technol. 12 (7) (2008) 555–566.

[8] European Commission, CORDIS: Projects and Results: Bringing 'flying wing' to the passenger, Cordis.europa.eu, 2014 [online]. Available: http://cordis.europa.eu/result/rcn/85652_en.html [accessed 05 11 2014].

[9] European Commission, CORDIS: Projects and Results: Final Report Summary – ACFA 2020 (Active control for flexible 2020 aircraft), Cordis.europa.eu, 2014 [online]. Available: http://cordis.europa.eu/result/rcn/53860_en.html [accessed 05 11 2014].

[10] J. Frota, NACRE novel aircraft concepts, Aeronaut. J. 114 (1156) (2010) 399–404.

[11] M.U. Guide, The MathWorks, Inc., Natick, MA, 1998, vol. 5.

[12] T. Hanis, Active control for high capacity flexible aircraft, 2012.

[13] T. Hanis, V. Kucera, M. Hromcik, Low order H optimal control for ACFA blended wing body aircraft, 2011.

[14] L. Hansen, W. Heinze, P. Horst, Representation of structural solutions in Blended Wing Body preliminary design, in: Proc. of the 25th International Congress on Aeronautical Sciences, ICAS2006, Hamburg, 2006.

[15] M. Hepperle, The VELA Project, 2005.

[16] D.C. Kammer, Optimal sensor placement for modal identification using system-realization methods, J. Guid. Control Dyn. 19 (3) (1996) 729–731.

[17] R.H. Liebeck, Design of the blended wing body subsonic transport, J. Aircr. 41 (1) (2004) 10–25.

[18] E. Maury, J. Frota, NACRE – New Aircraft Concepts Research, in: AeroSME FP6-Batch2 Meeting, 2003.

[19] D. McLean, Automatic Flight Control Systems, 1st edition, Prentice Hall, New York, 1990.

[20] M. Meheut, R. Grenon, G. Carrier, M. Defos, M. Duffau, Aerodynamic design of transonic flying wing configurations, in: KATnet II: Conference on Key Aerodynamic Technologies, Bremen, Germany, 2009.

[21] B. Mialon, M. Hepperle, Flying wing aerodynamics studies at ONERA and DLR, MH, vol. 150, 2005, p. 3.

[22] R.C. Nelson, Flight Stability and Automatic Control, 2nd edition, WCB/McGraw–Hill, 1998.

[23] N. Qin, A. Vavalle, A.L. Moigne, M. Laban, K. Hackett, P. Weinerfelt, Aerodynamic considerations of blended wing body aircraft, Prog. Aerosp. Sci. 40 (6) (2004) 321–343.

[24] H. Struber, M. Hepperle, Optimization of flying wing transport aircraft configurations in the VELA project, DLR, German Aerospace Center TR-DLR-IB-124-2005/905, Braunschweig, Germany, 2005.

[25] H. Tomas, M. Hromcik, Information-based sensor placement optimization for BWB aircraft, in: Proceedings of the 18th IFAC World Congress, 2011.

[26] M. Voskuijl, G.L. Rocca, F. Dircken, Controllability of blended wing body aircraft, in: 26th International Congress of the Aeronautical Sciences, 2008.

[27] A. Wildschek, An adaptive feed-forward controller for active wing bending vibration alleviation on large transport aircraft, 2009.

[28] A. Wildschek, Combined feed back control and feedforward control in order to actively reduce oscillations in aircraft, 2009.

[29] A. Wildschek, T. Hanis, Method and apparatus for minimizing dynamic structural loads of an aircraft, 2013.

[30] A. Wildschek, T. Hanis, F. Stroscher, E.I. Works, L optimization of an open loop gust load alleviation system for a large blended wing body airliner, 2012.

[31] A. Wildschek, R. Maier, F. Hoffmann, M. Jeanneau, H. Baier, Active wing load alleviation with an adaptive feedforward control algorithm, in: AIAA Guidance, Navigation, and Control Conference and Exhibit, 2006.

[32] A. Wildschek, R. Maier, M. Hromcik, T. Hanis, A. Schirrer, M. Kozek, C. Westermayer, M. Hemedi, Hybrid controller for gust load alleviation and ride comfort improvement using direct lift control flaps, in: Proceedings of Third European Conference for Aerospace Sciences, EUCASS, 2009.

[33] A. Wildschek, F. Stroscher, T. Klimmek, Z. Šika, T. Vampola, M. Valášek, D. Gangsaas, N. Aversa, A. Berard, A. France, Gust load alleviation on a large blended wing body airliner, in: Proceedings of ICAS, 2010.

Chapter 8

Adaptive Bandwidth Filtering in Attitude and Heading Reference System

8.1 Summary of Contribution

This chapter presents an extension of the work explained in Chapter 4 and 5. Here the adaptive data filtering as a data pre-processing step is combined with the final attitude estimation problem while eliminating the low frequency vibration impacts. First, the adaptive bandwidth filtering is applied as a pre-processing step to the ACC data for attenuating the vibration effects, afterwards the data is used to fuse with the ARS data to obtain the final attitude estimation based on the dual stage EKF fusion algorithm presented in Chapter 5. A method is presented for treating the ACC data with variable delay due to the usage of variable bandwidth filter. Finally, a comparative analysis has been presented on the improvement of the final attitude estimation by using and not using the proposed adaptive bandwidth filtering.

8.2 Introduction

In the cost effective navigation solution attitude evaluation using inertial sensors are primarily based on ARS data integration aided by ACC based attitude evaluation. The aiding from the ACC measurement can only be applied under strict steady state conditions when only gravity affects the ACC measurement and no external acceleration is present [52], [48] and [49]. However, these ideal aiding conditions are hardly achievable in harsh environments due to the presence of strong vibrations on light or small aircraft. The situation gets complicated as the frequency of

those vibrations cannot be simply isolated from the aircraft dynamics.

The vibration effect often dominates the ACC measurements. In addition, the vibration effects on the ACC measurements are generally periodic and sinusoidal in nature around a mean-value with a low frequency. Finite impulse response (FIR) filters are used for inertial data pre-processing to guarantee the stability. Depending on the class of aircraft, the ideal choice for pre-processing the ACC data is to apply a band-pass (BP) filter [3]; nevertheless, a narrow bandwidth BP filter would require a very high order filter, which is not desirable for navigation purposes due to the long delays. While applying a low pass (LP) filter with constant low bandwidth would loose the aircraft's motion information from the ACC measurement. Hence the concept of using variable bandwidth filter adapted based on the sinusoidal data estimation from the signal history is proposed.

The ACC measurements will experience variable time-delays due to the use of variable bandwidth filtering. The filter bandwidth is adapted by changing the order of the filter (as described in Chapter 4). Hence, the ACC data have variable time delays depending on the bandwidth chosen to filter the data. Therefore, delayed ACC data cannot be fused together with the non-delayed ARS data. In addition, for vehicles with fast dynamics, such as small aircraft it is not desirable to fuse the delayed ACC data with the non-delayed ARS data to obtain the final attitude.

Thus a two-step procedure is proposed to fuse the delayed ACC data with ARS to obtain the final attitude estimation. In the first step, the ARS bias is estimated as a delayed state by using the delayed ACC data and artificially delayed ARS data. In the second step, the estimated ARS bias as a delayed state is fedforward to the attitude estimator for calculating the final attitude. The next section describe in details the procedure to treat the delayed ACC data.

8.3   Treatment of Delayed ACC Data

The proposed adaptive pre-processing of ACC measurements for vibration suppression is based on the FIR filters, hence, the time-delays of the filter is precisely known depending on the chosen bandwidth. Therefore, the ARS data can be delayed to coincide the ACC data delay across a certain time window. An extra time-delayed estimator is proposed in addition to the presented scheme in the dual stage EKF in Chapter 5 (Section 2.1.2). The proposed time-delayed estimator structure consists of an attitude estimator which are time delayed. Then the time delayed attitude and the ARS bias is fedforward to a real-time attitude estimator. Afterwards a PVA estimator is used to obtain the final position, velocity estimates in real-time, see Fig 8.1.
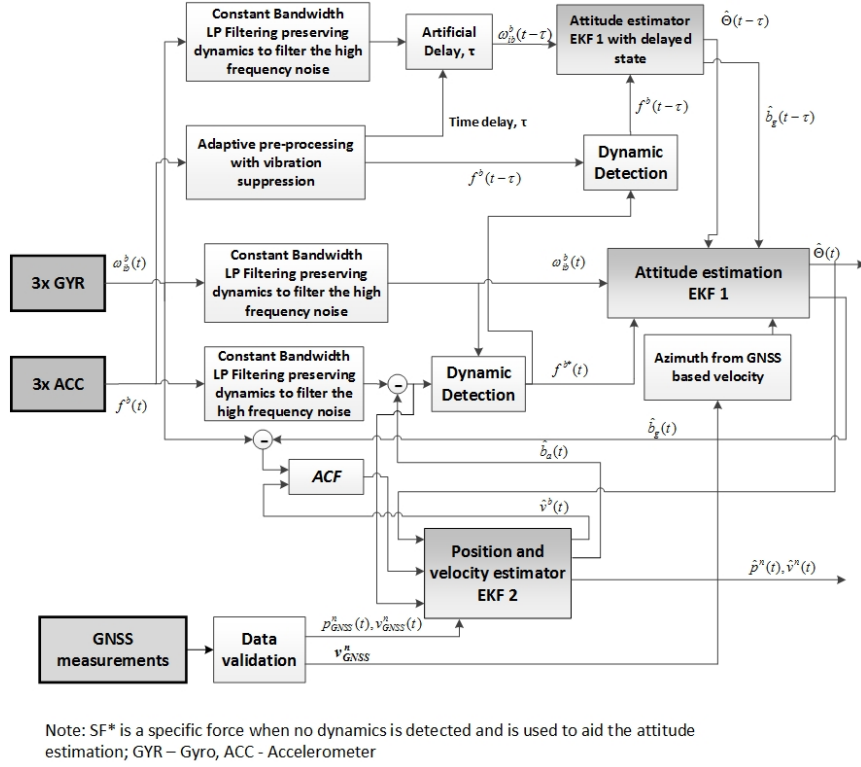
Note: SF* is a specific force when no dynamics is detected and is used to aid the attitude
estimation; GYR – Gyro, ACC - Accelerometer

Figure 8.1: Block scheme of treating delayed ACC data for the final PVA estimation.

The time-delay τ of filtered ACC data is variable depending on the bandwidth used for filtering. Therefore, the time-delayed attitude estimator from t to $t-\tau$ is adapted to accommodate the delayed ACC data by delaying ARS measurement at the input of the delayed attitude estimator. When there is no dynamics present in the ACC data, the ARS is continuously adapted to coincide the ACC delay. The modified kinematic model of the estimation of delayed attitude and ARS bias is written as:

$$\boldsymbol{\omega}_{ib}^{b}(t-\tau) = \omega_{ib}^{b}(t)e^{-\tau s}$$

$$\boldsymbol{x} = \left[\phi,\ \theta,\ \psi,\ b_{g_x},\ b_{g_y},\ b_{g_z}\right]^T, \boldsymbol{u} = \left[\ \omega_{b_x},\ \omega_{b_y},\ \omega_{b_z}\ \right]^T \tag{8.1}$$

$$\dot{\boldsymbol{x}}(t-\tau) = \left[\begin{array}{c} \left[\begin{array}{ccc} 1 & sin\phi(t-\tau)tan\theta(t-\tau) & cos\phi(t-\tau)tan\theta(t-\tau) \\ 0 & cos\phi(t-\tau) & -sin\phi(t-\tau) \\ 0 & sin\phi(t-\tau)sec\theta(t-\tau) & cos\phi(t-\tau)sec\theta(t-\tau) \end{array} \right] \left(\left[\begin{array}{c} \omega_{b_x}(t-\tau) \\ \omega_{b_y}(t-\tau) \\ \omega_{b_z}(t-\tau) \end{array} \right] - \left[\begin{array}{c} b_{g_x}(t-\tau) \\ b_{g_y}(t-\tau) \\ b_{g_z}(t-\tau) \end{array} \right] \right) \\ \begin{array}{c} 0 \\ 0 \\ 0 \end{array} \end{array} \right] \tag{8.2}$$

$$\boldsymbol{z} = \left[\begin{array}{c} a_x \\ a_y \\ a_z \end{array} \right], \boldsymbol{z} = \left[\begin{array}{c} sin\theta \\ -cos\theta sin\phi \\ -cos\phi sin\theta \end{array} \right] \tag{8.3}$$

It must be noted that using the equation (8.1) to (8.3) the output of the time-delayed attitude estimator are delayed attitude and ARS bias . In order to get the current attitude, the delayed states are fedforward to the real-time attitude estimator. The input of the real-time attitude estimator is the bias compensated ARS measurements.

8.4   Experimental Evaluation

In this section, the goal is to present the assessment and related discussions on the application of variable bandwidth filtering on the final attitude estimation. The experimental evaluations are carried out on the same flight data set as presented in Chapter 5. The following results are a continuation of the work presented in Chapter 4 and 5.

Fig 8.2 shows the ACC measurement during the whole flight and the filtered data using constant bandwidth filter and the newly proposed adaptive bandwidth filtering. Time instances where the ACC measurements are affected by low frequency vibration are zoomed and shown in Fig 8.3a and 8.3b. For the constant LP bandwidth filter a cut off frequency of 10 Hz was chosen. For the variable bandwidth filter, the filtering bandwidth was chosen all the way from 1 Hz to 10 Hz at regular intervals of 1 Hz. If the estimated/predicted frequency of the ACC measurement based on the signal history was bigger than 10 Hz, a simple LP filter (similar to constant bandwidth filter) with cut-off 10 Hz frequency is used.
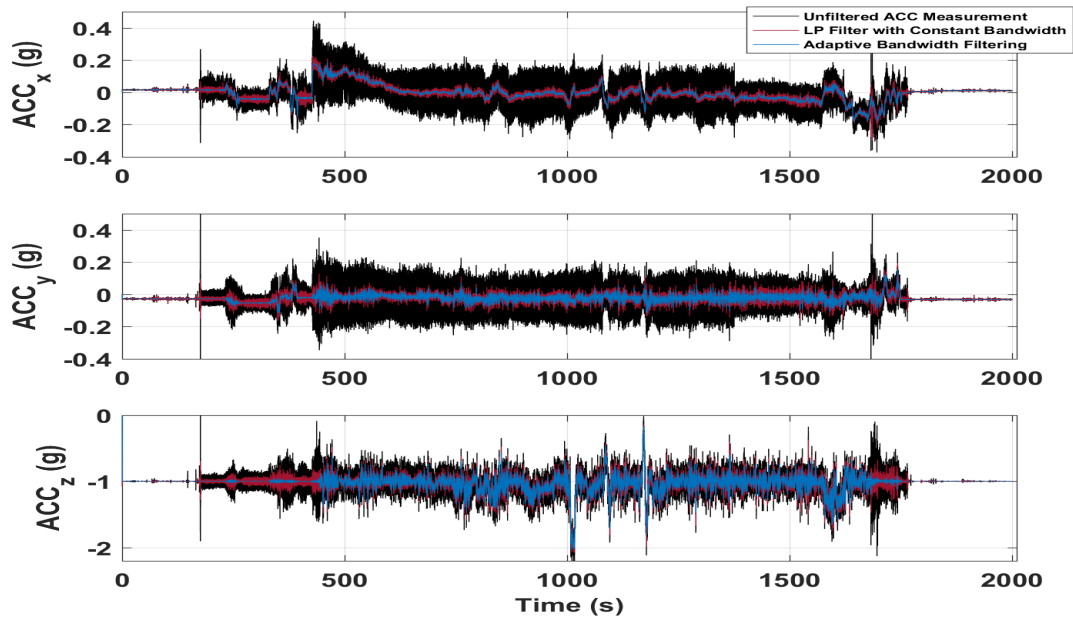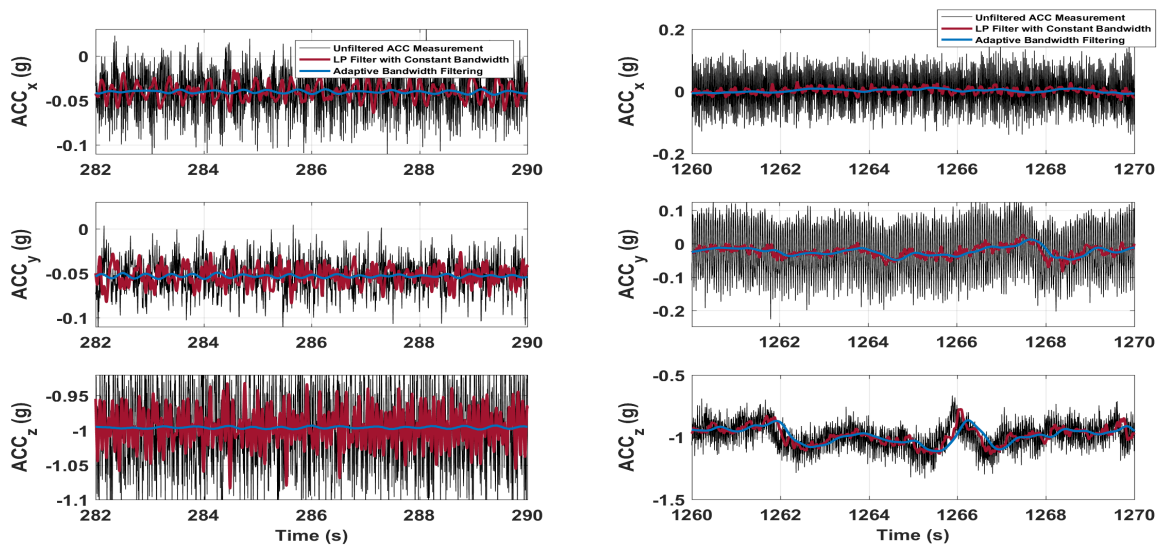
Figure 8.2: Measured ACC during the whole flight and the filtered signal.

(a) Zoomed ACC data from 282-290 seconds.

(b) Zoomed ACC data from 1830-1840 seconds.

Figure 8.3: Zoomed ACC data from the flight where the ACC are affected by low frequency vibration.

From Fig 8.3, it can be seen the ACC data are significantly affected by low frequency vibration

all the way down to 3.5 Hz (Fig 8.3a). Hence using a constant bandwidth filter will not attenuate these low frequency vibration. The data in Fig 8.3a represents the condition when the aircraft was waiting at the runway for taking off. These vibration effects on ACC are due to the structural vibrations translated from the aircraft's engine rotation. From Fig (8.3b) it can be seen that during the flight aircraft experiences vibration at high frequency. It can be seen while using adaptive bandwidth filtering these vibration effects are better attenuated to the mean-value than constant bandwidth filtering.

Fig 8.4 and 8.5 shows the attitude (pitch and roll angle) obtained from the ACC measurement only. It is important to note that attitude aiding from the ACC can not be used during the whole flight. Attitude aiding from the ACC measurement can only be applied when the ACC measurement are not affected by the dynamic motion of the aircraft and meets the steady state conditions. Using the dynamic detection algorithm presented in Chapter 5 (section 2.1.2), the steady state conditions are not met during the whole flight. For demonstration two instances are shown where the ACC measurement experiences vibration effects.
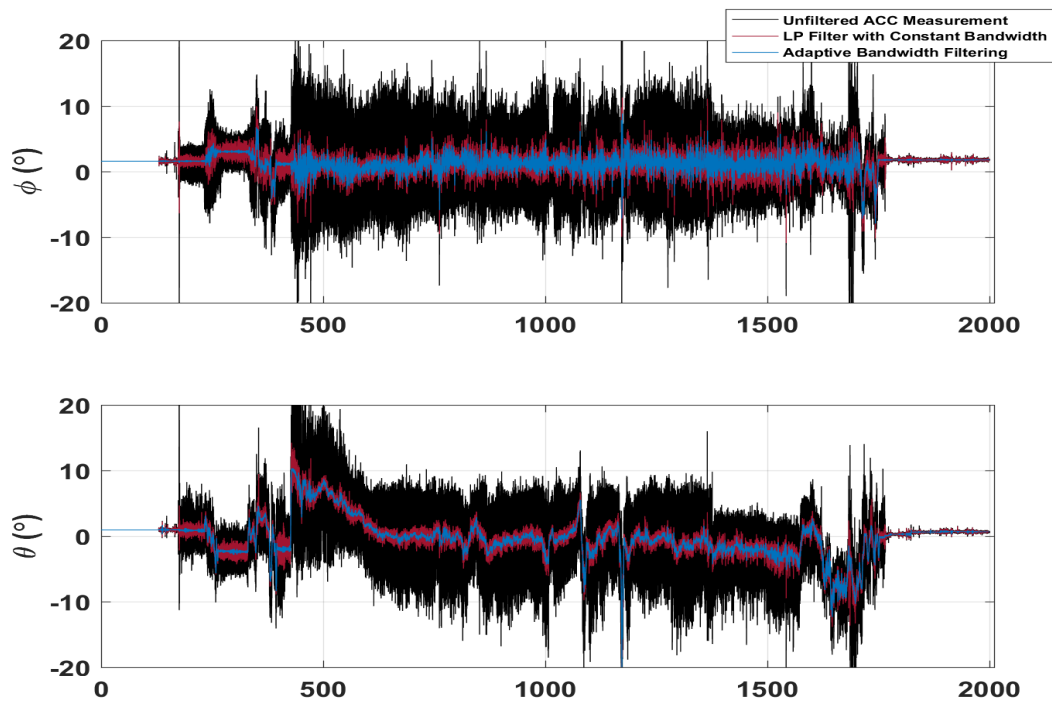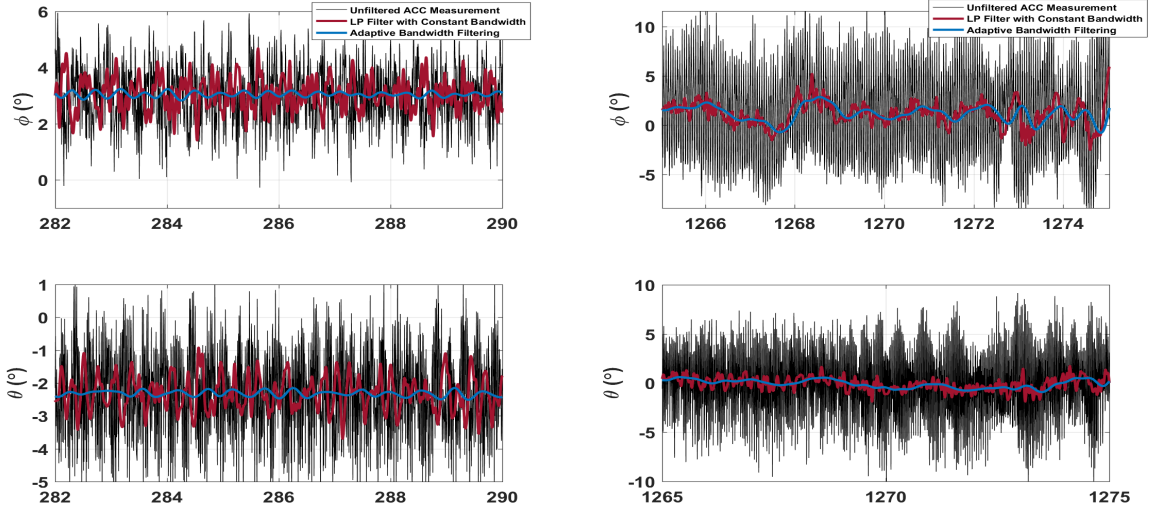

Figure 8.4: Pitch and Roll angles obtained from only ACC measurements during the whole flight.

It can be noticed from the zoomed plots in Fig 8.5b that using the adaptive bandwidth filter

(a) Zoomed attitude obtained from ACC measure-ment 282-290 seconds.

(b) Zoomed attitude obtained from ACC measurement 1830-1840 seconds.

Figure 8.5: Zoomed Pitch and Roll angles from the flight where the ACC are affected by low frequency vibration.

the vibrations effects are well attenuated to the mean-value compared to the constant bandwidth. This reduction in the oscillatory nature in the pitch and roll angles obtained from the ACC measurement should increase the accuracy of the final attitude estimation. In order to analyse the improvement of the final attitude estimation using the adaptive bandwidth filter we compare our attitude estimation with results presented in Section 5 published in Ref [45].

Fig 8.6 shows the results of the final attitude estimation using the adaptive bandwidth filtering compared with the estimation results presented in Chapter 5. Fig 8.7 shows the zoomed time instances where the ACC suffered from vibration effects and when the attitude aiding from the ACC measurement were used. For the azimuth (ψ) estimation heading information from the GNSS velocity measurements were used. The zoomed plots in Fig 8.7 shows instances ACC measurement were affected by low frequency vibration and the pitch and roll angle aiding from ACC measurement are used. It can be seen that the elimination of low frequency vibration improves the estimation results.
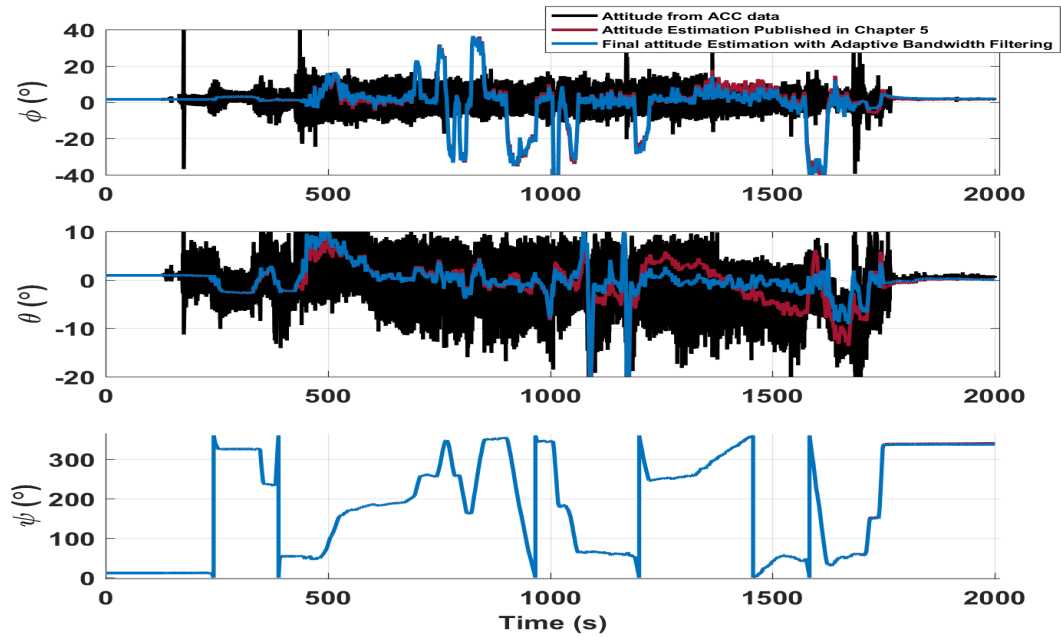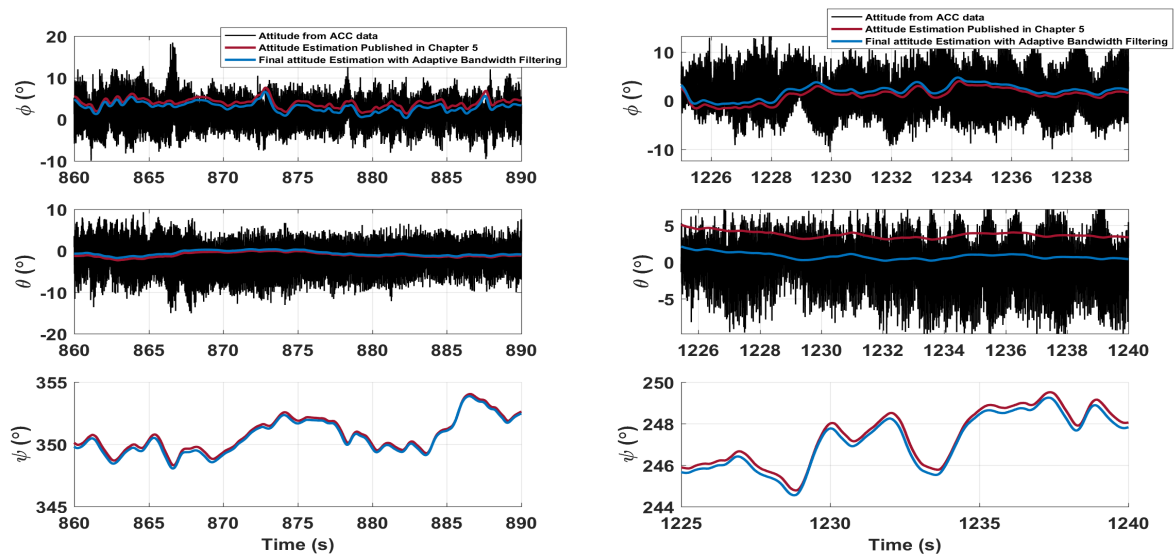
Figure 8.6: Comparison of final attitude estimation for the whole flight with and without using adaptive bandwidth filtering.

(a) Zoomed attitude estimation from 860-890 sec-onds.

(b) Zoomed attitude estimation from 1225-1240 sec-onds.

Figure 8.7: Zoomed final attitude estimation from the flight where the ACC are affected by low frequency vibration.

In Fig. 8.7 it can be noticed that the ACC data are affected by vibrations. Hence the attitude estimates from the ACC data are oscillatory. While fusing the ARS data with the ACC data filtered using constant bandwidth give higher values of final attitude estimates. In comparison, the final attitude estimation using adaptive bandwidth filter has lower value than final attitude estimated using constant bandwidth filer. It is because that ACC measurement is filtered to mean-value using the adaptive bandwidth filter. Hence using the adaptive bandwidth filtering improves the accuracy of the final attitude estimation.

Chapter 9

Conclusions

9.1   Summary of the thesis and contributions

This thesis has presented new theoretical results and applications related to strapdown inertial navigation for aircraft which can significantly improve the navigation performance. In addition, theoretical development has been made towards the control problem of fixed wing aircraft.

In the first part of the thesis a "easy to do", cost effective method for calibration of MEMS based inertial measurement unit is presented in contrast to using expensive calibration procedures. The presented method uses the information from gravity measurements under static conditions when the ACC triad is required to be calibrated. The calibration algorithm estimates the ACC and ARS error models, which includes deterministic errors such as scale factor errors, axes misalignment, and offsets. ACCs and ARSs often operates under harsh environment experiencing low frequency vibrations limiting the usability to aid the attitude estimation. A novel concept of filtering inertial data with an enhanced capability of providing smooth data under harsh environments, eliminating low frequency vibration influences is proposed. An adaptive bandwidth filtering method is presented as a pre-processing step to the ACC data. The modification of the filtering bandwidth relies on continuous estimation of the frequency of the strongest vibration content; based on that particular bandwidth filtering is applied on the ACC data. This filtering approach was confirmed based on simulated and real-flight data, and in all cases, the proposed approach reached better efficiency for vibration impact reduction, while preserving shorter processing delays compared with the commonly used approaches. Based on the effectiveness of vibration impact reduction, the proposed approach improves the ACC-based attitude compensation capability even under strong vibration, which brings a significant advantage compared with the commercially available AHRS systems. Afterwards a complete navigation solution is presented estimating the Position, Velocity and Attitude (PVA) using a strapdown inertial sensor

consisting of 3 tri-axial ACC and 3 tri-axial ARS applying GNSS position and velocity measurement as aiding source. Two different architectures of extended Kalman filter (EKF) are presented and discussed in details. The proposed approaches are validated on real flight data under various operational conditions which differ based on flight stage and on availability of aiding measurements, i.e. from a GNSS receiver providing position and velocity. The resultant performance is compared with other fusion techniques such as Nonlinear Observer with respect to the true reference position obtained by a dual-frequency X91+ GNSS receiver via Real Time Kinematics (RTK) based processing. Afterwards, a technique on how to fuse the delayed ACC measurement due to adaptive bandwidth filtering is outlined in details. The results are then compared and shows substantial improvement in final attitude estimation.

In the second part of the thesis, an automatic longitudinal flight controller is presented for conventional fixed-wing aircraft using non-linear dynamic inversion (NDI) technique or, in control theoretic terms, the partial exact feedback linearisation. Main theoretical results include designing of three different tracking flight controllers which provides full control of longitudinal states (velocity, angle of attack and pitch angle) of the aircraft. A detailed study on the stability of the internal dynamics for each controller are carried out and has been showed to be stable. Combination of these three flight controllers depending on the flight condition provided full 3-DOF longitudinal control authority of a fixed-wing aircraft. Simulation results demonstrate that with the proposed controllers, longitudinal motion of a conventional multi-role combat aircraft can be controlled with small tracking error. Finally, a load alleviation system was proposed for an aircraft. A combined mixed feedforward/feedback control approach is proposed for reducing the vibration impacts on wings due to external disturbances such as vertical wing gusts.

9.2   Future Work

In this section several suggestions for the future research extending the work presented in this doctoral thesis are proposed.

- The platform of interest in this thesis is presented by small aircraft. It would be interesting to investigate how the presented navigation solution performs on other type of vehicles such as marine vessels, car, train, small robots and UAVs. A keen point of research in this area would be to investigate how the presented navigation solutions in this doctoral thesis can be modified to have an unified frame work which can be applied for all types of vehicles.

- It would be interesting for future research to compare the estimated attitude with respect to true reference attitude obtained via more precise sensor's such as fibre optic gyro's or by using differential GPS receivers which are capable of providing attitude estimations.

- The data fusion results obtained by using the extended Kalman filter can be adapted to the eXogenous Kalman filter (XKF) structure.

- The attitude can be represented by quaternions instead of Euler's angle. This will widen the scope of the usage of the navigation solution with respect to highly manoeuvrable vehicles avoiding the singularity issues.

- The nonlinear control technique using partial feedback linearization can be extended to full lateral-directional control of the fixed wing aircraft. This will provide a complete 6-DOF flight control of the aircraft.

- A detailed analysis on the distribution of the wing loading across the entire aircraft's wing is essential for the validation of the proposed load alleviation system.

Bibliography

[1] Mushfiqul Alam and Sergej Celikovsky. On the internal stability of non-linear dynamic inversion: application to flight control. *IET Control Theory & Applications*, 2017.

[2] Mushfiqul Alam, Martin Hromcik, and Tomas Hanis. Active gust load alleviation system for flexible aircraft: Mixed feedforward/feedback approach. *Aerospace Science and Technology*, 41:122–133, 2015.

[3] Mushfiqul Alam and Jan Rohac. Adaptive data filtering of inertial sensors with variable bandwidth. *Sensors*, 15(2):3282–3298, 2015.

[4] Mushfiqul Alam, Martin Sipos, Jan Rohac, and Jakub Simanek. Calibration of a multi-sensor inertial measurement unit with modified sensor frame. In *Industrial Technology (ICIT), 2015 IEEE International Conference on*, pages 1984–1989. IEEE, 2015.

[5] Ravindra Babu and Jinling Wang. Ultra-tight gps/ins/pl integration: a system concept and performance analysis. *GPS solutions*, 13(1):75–82, 2009.

[6] Pierre-Jean Bristeau and Nicolas Petit. Navigation system for ground vehicles using temporally interconnected observers. In *American Control Conference (ACC), 2011*, pages 1260–1267. IEEE, 2011.

[7] Zhe Chen et al. Bayesian filtering: From kalman filters to particle filters, and beyond. *Statistics*, 182(1):1–69, 2003.

[8] TE Disney. C-5a active load alleviation system. *Journal of Spacecraft and Rockets*, 14(2):81–86, 1977.

[9] Gamini Dissanayake, Salah Sukkarieh, Eduardo Nebot, and Hugh Durrant-Whyte. The aiding of a low-cost strapdown inertial measurement unit using vehicle model constraints for land vehicle applications. *IEEE transactions on robotics and automation*, 17(5):731–747, 2001.

[10] Zhuxin Dong, Guanglie Zhang, Yilun Luo, Chi Chiu Tsang, Guangyi Shi, Sze Yin Kwok, Wen J Li, Philip HW Leong, and Ming Yiu Wong. A calibration method for mems inertial sensors based on optical tracking. In *Nano/Micro Engineered and Molecular Systems, 2007. NEMS'07. 2nd IEEE International Conference on*, pages 542–547. IEEE, 2007.

[11] Arnaud Doucet and Adam M Johansen. A tutorial on particle filtering and smoothing: Fifteen years later. *Handbook of nonlinear filtering*, 12(656-704):3, 2009.

[12] Alexandr Draganov, Lin Haas, and Marc Harlacher. The imre kalman filter—a new kalman filter extension for nonlinear applications. In *Position Location and Navigation Symposium (PLANS), 2012 IEEE/ION*, pages 428–440. IEEE, 2012.

[13] Jay Farrell. *Aided navigation: GPS with high rate sensors*. McGraw-Hill, Inc., 2008.

[14] D Fraser and J Potter. The optimum linear smoother as a combination of two optimum linear filters. *IEEE Transactions on Automatic Control*, 14(4):387–390, 1969.

[15] Arthur Gelb. *Applied optimal estimation*. MIT press, 1974.

[16] Philippe Goupil. Airbus state of the art and practices on fdi and ftc in flight control system. *Control Engineering Practice*, 19(6):524–539, 2011.

[17] Mohinder S Grewal, Angus P Andrews, and Chris G Bartone. *Global navigation satellite systems, inertial navigation, and integration*. John Wiley & Sons, 2013.

[18] Mohinder S Grewal, Lawrence R Weill, and Angus P Andrews. *Global positioning systems, inertial navigation, and integration*. John Wiley & Sons, 2007.

[19] Paul D Groves. *Principles of GNSS, inertial, and multisensor integrated navigation systems*. Artech house, 2013.

[20] Fredrik Gustafsson, Fredrik Gunnarsson, Niclas Bergman, Urban Forssell, Jonas Jansson, Rickard Karlsson, and P-J Nordlund. Particle filters for positioning, navigation, and tracking. *IEEE Transactions on signal processing*, 50(2):425–437, 2002.

[21] Tomas Hanis and Martin Hromcik. Information-based sensor placement optimization for bwb aircraft. *IFAC Proceedings Volumes*, 44(1):2236–2241, 2011.

[22] Jakob M Hansen, Thor I Fossen, and Tor Arne Johansen. Nonlinear observer design for gnss-aided inertial navigation systems with time-delayed gnss measurements. *Control Engineering Practice*, 60:39–50, 2017.

[23] Jakob M Hansen, Jan Roháč, Martin Šipoš, Tor A Johansen, and Thor I Fossen. Validation and experimental testing of observers for robust gnss-aided inertial navigation. In *Recent Advances in Robotic Systems*. InTech, 2016.

[24] H Hoenlinger, H Zimmermann, O Sensburg, and J Becker. Structural aspects of active control technology. In *AGARD CONFERENCE PROCEEDINGS AGARD CP*, pages 18–18. DTIC Document, 1995.

[25] Myung Hwangbo, Jun-Sik Kim, and Takeo Kanade. Imu self-calibration using factorization. *IEEE Transactions on Robotics*, 29(2):493–507, 2013.

[26] JF Johnston. Accelerated development and flight evaluation of active controls concepts for subsonic transport aircraft. volume 1: Load alleviation/extended span development and flight tests. 1979.

[27] Simon J Julier and Jeffrey K Uhlmann. New extension of the kalman filter to nonlinear systems. In *AeroSense'97*, pages 182–193. International Society for Optics and Photonics, 1997.

[28] Rudolph E Kalman and Richard S Bucy. New results in linear filtering and prediction theory. *Journal of basic engineering*, 83(3):95–108, 1961.

[29] Vladimir Kubelka and Michal Reinstein. Complementary filtering approach to orientation estimation using inertial sensors only. In *Robotics and Automation (ICRA), 2012 IEEE International Conference on*, pages 599–605. IEEE, 2012.

[30] Stephen H Lane and Robert F Stengel. Flight control design using non-linear inverse dynamics. *Automatica*, 24(4):471–483, 1988.

[31] Yong Li, Jinling Wang, Chris Rizos, Peter Mumford, and Weidong Ding. Low-cost tightly coupled gps/ins integration based on a nonlinear kalman filtering design. In *Proceedings of ION National Technical Meeting*, pages 18–20, 2006.

[32] Bei Lu, Fen Wu, and SungWan Kim. Switching lpv control of an f-16 aircraft via controller state reset. *IEEE transactions on control systems technology*, 14(2):267–277, 2006.

[33] D Magill. Optimal adaptive estimation of sampled stochastic processes. *IEEE Transactions on Automatic Control*, 10(4):434–439, 1965.

[34] F Landis Markley. Attitude error representations for kalman filtering. *Journal of guidance, control, and dynamics*, 26(2):311–317, 2003.

[35] Peter S Maybeck and George M Siouris. Stochastic models, estimation, and control, volume i. *IEEE Transactions on Systems, Man, and Cybernetics*, 10(5):282–282, 1980.

[36] D McLean. Globally stable nonlinear flight control system. In *IEE Proceedings D (Control Theory and Applications)*, volume 130, pages 93–102. IET, 1983.

[37] Raman Mehra. Approaches to adaptive filtering. *IEEE Transactions on automatic control*, 17(5):693–698, 1972.

[38] AH Mohamed and KP Schwarz. Adaptive kalman filtering for ins/gps. *Journal of geodesy*, 73(4):193–203, 1999.

[39] Guy Norris and Mark Wagner. *Airbus A380: superjumbo of the 21st century*. Zenith Imprint, 2005.

[40] Guy Norris and Mark Wagner. *Boeing 787 dreamliner*. MBI Publishing Company and Zenith Press, 2009.

[41] Michael Norton, Suiyang Khoo, Abbas Kouzani, and Alex Stojcevski. Adaptive fuzzy multi-surface sliding control of multiple-input and multiple-output autonomous flight systems. *IET Control Theory & Applications*, 9(4):587–597, 2015.

[42] Christakis Papageorgiou and Keith Glover. Robustness analysis of nonlinear flight controllers. *Journal of Guidance, Control, and Dynamics*, 28(4):639–648, 2005.

[43] Mark G Petovello, Kyle O'Keefe, Gérard Lachapelle, and M Elizabeth Cannon. Consideration of time-correlated errors in a kalman filter applicable to gnss. *Journal of Geodesy*, 83(1):51–56, 2009.

[44] Herbert E Rauch, CT Striebel, and F Tung. Maximum likelihood estimates of linear dynamic systems. *AIAA journal*, 3(8):1445–1450, 1965.

[45] Jan Rohac, Jakob M Hansen, Mushfiqul Alam, Martin Sipos, Tor A Johansen, and Thor I Fossen. Validation of nonlinear integrated navigation solutions. *Annual Reviews in Control*, 43:91–106, 2017.

[46] Jan Rohac, Martin Sipos, and Jakub Simanek. Calibration of low-cost triaxial inertial sensors. *IEEE Instrumentation & Measurement Magazine*, 18(6):32–38, 2015.

[47] F Santoso, M Liu, and GK Egan. Robust autopilot synthesis for longitudinal flight of a special unmanned aerial vehicle: a comparative study. *Institute of Engineering and Technology (IET) Control Theory and Applications*, 2(7):583–594, 2008.

[48] Paul G Savage. Strapdown inertial navigation integration algorithm design part 1: Attitude algorithms. *Journal of guidance, control, and dynamics*, 21(1):19–28, 1998.

[49] Paul G Savage. Strapdown inertial navigation integration algorithm design part 2: Velocity and position algorithms. *Journal of Guidance, Control, and Dynamics*, 21(2):208–221, 1998.

[50] Jeffery A Schroeder. Upset prevention and recovery training-a regulator update. In *AIAA Modeling and Simulation Technologies Conference*, page 1429, 2016.

[51] S Sieberling, QP Chu, and JA Mulder. Robust flight control using incremental nonlinear dynamic inversion and angular acceleration prediction. *Journal of Guidance, Control, and Dynamics*, 33(6):1732–1742, 2010.

[52] Martin Sipos, Pavel Paces, Michal Reinstein, and Jan Rohac. Flight attitude track reconstruction using two ahrs units under laboratory conditions. In *Sensors, 2009 IEEE*, pages 675–678. IEEE, 2009.

[53] Martin Sipos, Pavel Paces, Jan Rohac, and Petr Novacek. Analyses of triaxial accelerometer calibration algorithms. *IEEE Sensors Journal*, 12(5):1157–1165, 2012.

[54] Brian L Stevens, Frank L Lewis, and Eric N Johnson. *Aircraft control and simulation: dynamics, controls design, and autonomous systems*. John Wiley & Sons, 2015.

[55] LW Stimac and Thomas A Kennedy. Sensor alignment kalman filters for inertial stabilization systems. In *Position Location and Navigation Symposium, 1992. Record. 500 Years After Columbus-Navigation Challenges of Tomorrow. IEEE PLANS'92., IEEE*, pages 321–334. IEEE, 1992.

[56] Peter Swerling. First-order error propagation in a stagewise smoothing procedure for satellite observations. 1959.

[57] Peter Swerling. Probability of detection for fluctuating targets. *IRE Transactions on Information Theory*, 6(2):269–308, 1960.

[58] David Titterton and John L Weston. *Strapdown inertial navigation technology*, volume 17. IET, 2004.

[59] Qian Wang and Robert F Stengel. Robust nonlinear flight control of a high-performance aircraft. *IEEE Transactions on Control Systems Technology*, 13(1):15–26, 2005.

[60] Andreas Wildschek. *An adaptive feed-forward controller for active wing bending vibration alleviation on large transport aircraft*. Dr. Hut, 2009.

[61] Andreas Wildschek. Influence of h2 and l1 criteria on feed-forward gust loads control optimized for the minimization of wing box structural mass on an aircraft with active winglets. In *Smart Intelligent Aircraft Structures (SARISTU): Proceedings of the Final Project Conference*, page 319. Springer, 2015.

[62] Andreas Wildschek, Rudolf Maier, Falk Hoffmann, Matthieu Jeanneau, and Horst Baier. Active wing load alleviation with an adaptive feed-forward control algorithm. In *AIAA Guidance, Navigation, and Control Conference and Exhibit*, page 6054, 2006.

[63] Robert Wolf, Bemd Eissfeller, and GW Hein. A kalman filter for the integration of a low cost ins and an attitude gps. In *Proceedings of the International Symposium on Kinematic Systems in Geodesy, Geomatics and Navigation*, pages 143–150, 1997.